

(NASA-CL-144,85) DESIGN OF A TORQUE CURRENT  
GENERATOR FOR STRAPDOWN GYROSCOPES Ph.D.  
Thesis (Tennessee Univ.) 228 p HC \$8.00

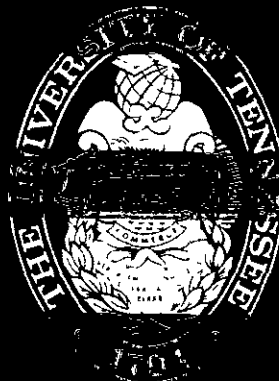
N76-13197

CSCI 22E

Unclas

63/19

05-97



# **ELECTRICAL ENGINEERING DEPARTMENT**

**UNIVERSITY OF TENNESSEE**

**KNOXVILLE  
TN 37916**

Prepared For

George C. Marshall Space Flight Center  
National Aeronautics and Space Administration  
Under Contract NAS8-27296/DCN 1-1-40-10230

DESIGN OF A TORQUE CURRENT GENERATOR

FOR STRAPDOWN GYROSCOPES

R. D. McKnight

T. V. Blalock, E. J. Kennedy

Technical Report TR-EE/EL-1

August 1, 1974



Submitted as a thesis by R. D. McKnight to the Graduate Council  
of the University of Tennessee in partial fulfillment of the  
requirements for the degree of Doctor of Philosophy.

## ACKNOWLEDGMENTS

Financial support for much of the work presented in this thesis was provided by the National Aeronautics and Space Administration's Marshall Space Flight Center under Contract NAS8-27296.

The author is particularly indebted to his major professor, Dr. E. J. Kennedy, and to Dr. T. V. Blalock for their helpful suggestions, constructive criticisms, and encouragement during the preparation of this work. The author thanks Dr. J. M. Googe and Dr. P. G. Huray for serving on his doctoral committee. A debt of gratitude is extended to Messrs. Joe Parker, Hugo Berry, and Clyde Jones of the George C. Marshall Space Flight Center for their help and cooperation. The author also thanks Mr. Michael Galyon for help in breadboarding and schematics in the initial portion of this work.

Special thanks are due Mrs. Beverly C. Perry for her patience and skill in typing the final draft of the thesis.

Finally, the author would like to express his appreciation to four very special people for their support to this work. The author's wife, Sara, and three daughters, Sarita, Anita, and Lisa, have exhibited almost boundless patience, love, and endurance throughout the preparation of this work.

## ABSTRACT

The objective of this thesis was to design, analyze, and experimentally evaluate an optimum performance torque current generator for use with strapdown gyroscopes. Among the criteria used to evaluate the design were the following: steady-state accuracy; margins of stability against self-oscillation, temperature variations, aging, etc.; static and drift errors; PVR errors; transient errors; classical frequency and time domain characteristics; and the equivalent noise at the input of the comparator operational amplifier.

The DC feedback loop of the torque current generator was approximated as a second-order system. The magnitudes of the loop gain were approximately 159.4 dB and 157.3 dB for the low- and high-torque cases, respectively. The low- and high-torquing levels were 30 mA and 60 mA, respectively.

Stability calculations yielded gain margins of 18 dB and 21 dB for the low- and high-torque cases, respectively. The phase margin for the low-torque case was 27 degrees, and for the high-torque case was 30 degrees. These margins resulted from adjusting compensation in the torque current generator to give an optimum current waveform through the torquer coil of the gyro. Variations in the magnitude and pole locations of the loop transmission due to temperature changes were negligible.

The steady-state actuating error was 0.011 ppm for the low-torque case, and 0.0136 ppm for the high-torque case. The closed-loop bandwidth of the torque current generator loop was approximately 200 kHz.

Error calculations indicate that transient feedthrough currents in the H-switch may cause a maximum error in the movement of the gyro float of approximately  $1.8 \times 10^{-4}$  arc-seconds per interrogation period. When compared to the current-time area in an ideal 30 mA current pulse under nulled gyro conditions and a limit cycle frequency of 2.4 kHz, the feedthrough error was approximately 14 ppm. Unequal rise- and fall-times of the torque current pulse contributed a worst-case gyro float movement error of  $9.6 \times 10^{-4}$  arc-seconds per interrogation period. The worst-case static error was 0.7 ppm, and the worst-case drift error was 0.07 ppm/°C when compared to a low-scale current of 30 mA. Worst-case PVR errors were 3.6 ppm/°C and 2.2 ppm/°C for the low- and high-torque cases, respectively. The worst-case long-term drift error in the PVR was approximately 96 ppm/month.

A noise analysis of the torque current generator was made for a torque current level of 30 mA. The result was a total rms input noise (at the input of the comparator operational amplifier) in the 0.1 Hz to 200 kHz interval of  $20.9 \mu\text{V}_{\text{rms}}$ . The input noise was found to be not strongly dependent on the torque current level.

Using the Kearfott 2544 gyro, the rise- and fall-times (10-90%) for a 30 mA current pulse through the torquer were 70 nsec and 90 nsec, respectively. When switching torquing levels (30 mA to 60 mA, and vice-versa), the rise- and fall-times were approximately 12  $\mu\text{sec}$ , which represents approximately 8 data periods.

## TABLE OF CONTENTS

CHAPTER	. PAGE
I. INTRODUCTION . . . . .	1
Background . . . . .	1
Scope of the Thesis . . . . .	4
II. DESIGN CONSIDERATIONS FOR THE TORQUE	
CURRENT GENERATOR . . . . .	7
The Torque Current Generator in Perspective . . . . .	8
Design Goals for the Torque Current Generator . . . . .	12
Design Theory - Preliminary Error Analysis . . . . .	15
Error Due to Lower H-switch Elements . . . . .	15
Error Due to Upper H-switch Elements . . . . .	23
Error Due to "ON" Voltage . . . . .	25
Design Implications from the Preliminary Error	
Analysis . . . . .	26
III. TORQUE CURRENT GENERATOR IMPLEMENTATION . . . . .	31
The Precision Voltage Reference . . . . .	31
The Comparator Operational Amplifier . . . . .	38
The Error Amplifier - Level Shift Network . . . . .	40
The Power Transistor Stage . . . . .	41
The H-Switch . . . . .	41
The H-Switch Driver . . . . .	43
The Sampling Resistors and Sampling Resistor	
Switching Network . . . . .	44

CHAPTER	PAGE
The TTL to CMOS Interfacing Network . . . . .	45
Torquer Compensation . . . . .	45
IV. LOOP TRANSMISSION AND STABILITY AGAINST SELF-OSCILLATION . . . . .	48
Loop Transmission of the Torque Current Generator . . . . .	50
Criteria for Evaluating the Relative Stability of the Torque Current Generator . . . . .	60
Relative Stability of the Torque Current Generator . . . . .	62
V. CLOSED LOOP FREQUENCY RESPONSE AND STEADY-STATE ACCURACY . . . . .	64
Closed-Loop Frequency Response of the Torque Current Generator . . . . .	64
Frequency Dependence of the Feedback Network . . . . .	66
A Simplified Feedback Configuration for the TCG . . . . .	68
An Algebraic Expression for the Closed-Loop Voltage Gain of the TCG . . . . .	73
Closed-Loop Frequency Response of the TCG From T Via the Nichols Chart . . . . .	79
Steady-State Accuracy of the Torque Current Generator . . . . .	82
VI. STABILITY OF THE TCG AGAINST VARIATIONS DUE TO TEMPERATURE, AGING AND SEMICONDUCTOR DEVICE REPLACEMENT . . . . .	90
The Effect of Temperature Variations Upon $ T_{mid} $ of the TCG . . . . .	90

CHAPTER	PAGE
Loop Transmission Variation with Temperature for the Low-Torque Mode . . . . .	100
Loop Transmission Variation with Temperature for the High-Torque Mode . . . . .	103
Effect of Temperature Variations Upon the Location of Poles of the Loop Transmission . . . . .	104
Thermal Runaway Possibilities in the TCG Loop . . . . .	107
VII. TIME DOMAIN CHARACTERISTICS OF THE TORQUE CURRENT	
GENERATOR LOOP . . . . .	108
The Low-Torque Case . . . . .	110
The High-Torque Case . . . . .	111
VIII. ERROR ANALYSIS OF THE H-SWITCH AND PRECISION	
VOLTAGE REFERENCE CIRCUIT . . . . .	114
The H-Switch . . . . .	114
Transient Feedthrough Currents . . . . .	116
Rise- and Fall-Time Inaccuracy . . . . .	122
Offset and Drift Errors in the H-Switch . . . . .	125
The PVR Circuit . . . . .	126
IX. NOISE CONSIDERATIONS FOR THE TORQUE CURRENT	
GENERATOR . . . . .	132
General Comments . . . . .	132
Noise Analysis of the TCG . . . . .	133
X. VERSATILITY OF THE TORQUE CURRENT	
GENERATOR . . . . .	147



CHAPTER	PAGE
Current Range Capability of the TCG . . . . .	147
Maximum Torquing Current of the TCG . . . . .	148
Minimum Torquing Current of the TCG . . . . .	152
Some Possible Modifications of the TCG . . . . .	155
Driving the TCG with TTL Logic . . . . .	155
Driving with TTL Logic with 35 V Supply Present . . . . .	156
Driving with TTL Logic with 35 V Supply Eliminated . . . . .	156
Driving the TCG with CMOS Logic . . . . .	157
Driving with CMOS Logic with 35 V Supply Present . . . . .	157
Driving with CMOS Logic with 35 V Supply Eliminated . . . . .	163
The TCG with One Sampling Resistor . . . . .	163
Effect of a Lower PVR . . . . .	167
XI. EXPERIMENTAL RESULTS . . . . .	170
XII. CONCLUSIONS . . . . .	178
Summary . . . . .	178
Suggestions for Further Study . . . . .	179
BIBLIOGRAPHY . . . . .	185
APPENDIXES . . . . .	191
Appendix A . . . . .	192
Appendix B . . . . .	194
Appendix C . . . . .	197
Appendix D . . . . .	203
Appendix E . . . . .	207
VITA . . . . .	214

## LIST OF TABLES

TABLE		PAGE
4.1.	Gain and Phase Margins of the Torque Current.	
	Generator . . . . .	63
5.1.	Closed-Loop Frequency Response Parameters for the	
	Torque Current Generator . . . . .	78
6.1.	Parameter Values used in Temperature Calculations . . . . .	101
8.1.	Drift Data used for Drift Error Analysis of the PVR . . . . .	129
9.1.	Contributions of the Noise Terms in Equation (9.1)	
	and Figure 9.1 for the Indicated Frequency Intervals,	
	and for a Torque Current of 30 mA . . . . .	144
9.2.	$e_{ni}$ for the Indicated Frequency Intervals . . . . .	145
12.1.	A Tabular Summary of Theoretical and Experimental	
	Performance Characteristics of the TCG . . . . .	180
D.1.	Data for Graphical Solution of Closed-Loop Frequency	
	Response from T via Nichols Chart . . . . .	205

## LIST OF FIGURES

FIGURE		PAGE
2.1.	The Basic Elements of a Width-Modulated Binary Rebalance Loop . . . . .	9
2.2.	U.T. Rebalance Electronics - Block Diagram . . . . .	10
2.3.	Block Diagram of a Torque Current Generator for Strapdown Gyroscopes . . . . .	16
2.4.	Lower H-Switch Elements and Their Associated Drive Currents . . . . .	18
2.5.	An Equivalent Circuit of the Current Regulator and H-Switch Sections of the Torque Current Generator . . . . .	19
2.6.	An Additional Equivalent Circuit of the Current Regulator and H-Switch Sections of the Torque Current Generator . . . . .	24
2.7.	A Composite Field-Effect-Bipolar Transistor . . . . .	28
3.1.	Torque Current Generator . . . . .	32
3.2.	TTL to CMOS Interface . . . . .	46
4.1.	Test Configurations for Obtaining the Open-Loop Frequency Response of the AD504M Operational Amplifier . . . . .	52
4.2.	Open-Loop Frequency Response of the AD504M Operational Amplifier with $C_c = 3380 \text{ pF}$ . . . . .	54
4.3.	Closed-Loop Configurations of the AD504M Op. Amp. used to Study Effects of the Feedforward Network . . . . .	56

## FIGURE

## PAGE

4.4.	PCAP Results for Voltage Gain and Phase Versus Frequency for Torque Current Generator from Output of Op. Amp. to Input of Op. Amp. . . . .	58
4.5.	Bode Plot of the Loop Transmission of the Torque Current Generator . . . . .	59
5.1.	Impedance $Z_B$ Seen Looking into the Top of the H-Switch for the Low-Torque Case . . . . .	67
5.2.	A Controlled Current Source used to Discuss Feedback Mechanisms in the TCG . . . . .	70
5.3.	A Simplified Feedback Configuration Representing the Torque Current Generator . . . . .	72
5.4.	Bode Plots of $ A_{fv} $ for the Low- and High-Torque Cases of the Torque Current Generator . . . . .	80
5.5.	Block Diagram of the Simplified Torque Current Generator . . . . .	84
8.1.	Model of H-Switch for Offset Current Error Analysis . . . . .	115
8.2.	A Simplified Model of the PVR and Associated Circuitry for Use in Drift Error Analysis . . . . .	127
9.1.	Feedback Circuit Representations of the TCG for Use in Noise Analysis . . . . .	134
9.2.	Representations of a Composite FET-Bipolar Transistor for Use in Noise Analysis . . . . .	137
10.1.	Plots of Voltage Drop and Power Dissipation Constraints Indicating Torquing Current and Torquer Resistance Ranges, for a Power Supply Voltage of 35 V . . . . .	150

FIGURE	PAGE
10.2. A TCG Circuit for Low-Level Torquing Currents and Low DC Torquer Resistances . . . . .	154
10.3. A Modification of the H-Switch Driver to Allow Elimination of the 35 V Power Supply Using TTL Logic . . .	158
10.4. TTL to CMOS Interface for Driving the Sampling Resistor Switching Network with No 35 V Supply and Using TTL Logic . . . . .	159
10.5. (-5)V Bias for TTL to CMOS Interface . . . . .	160
10.6. Modification of TCG to Accommodate Elimination of +35 V Supply . . . . .	161
10.7. Modification of TCG to Accommodate Elimination of +35 V Supply with Alternate Output Stages . . . . .	162
10.8. An H-Switch Driver Circuit for Use with CMOS Logic . . . . .	164
10.9. H-Switch Driver Circuit for the Case when CMOS Logic and No 35 V Supply is Used . . . . .	165
10.10. Interface Circuit to Drive Sampling Resistor Switching Network when CMOS Logic and No 35V Supply is Used . . . .	166
11.1. Current and Voltage Waveforms Through and Across the Torquer when Torquing the Kearfott 2544 Gyro . . . . .	171
11.2. Transient Response of Torquer Current when Switched from Low to High Scale (30 mA to 60 mA). Spin Motor On . . . . .	172
11.3. An Output of the H-Switch Driver (Gate of Q4B) . . . . .	174

FIGURE	PAGE
11.4. Transient Inputs to the AD504M Op. Amp. when Switching Torquing Scale Factors (30 mA to 60 mA) . . . . .	175
11.5. Voltage Waveforms Across Sampling Resistors and ICl Op. Amp. Output During Scale Factor Switching (30 mA to 60 mA) . . . . .	176
B.1. Equivalent Circuit of the Torquer Coil and Compensation . . . . .	194
C.1. Closed-Loop Inverting-Mode Configuration of an Operational Amplifier . . . . .	197
C.2. A Feedback Configuration Having the Same Parameter Relationships as Figure C.1 . . . . .	198
C.3. A Block Diagram Representation Equivalent to that in Figure C.2 . . . . .	199
C.4. A Block Diagram Representation Equivalent to that in Figure C.3 . . . . .	199
D.1. The Loop Transmission of the TCG Plotted on a Nichols Chart . . . . .	204

## CHAPTER I

### INTRODUCTION

#### A. Background

The degree of accuracy and environmental capability of inertial measurement units has increased rapidly in the last decade. Until recently, the platform variety of inertial units has enjoyed the role of being the most often used inertial unit in inertial navigation, guidance and control systems. Advances in computer technology, particularly in resolution and speed, have made possible the emergence of the strapdown system as a new generation of navigation equipment.<sup>1</sup> The gyroscope is the most important component of an inertial measurement unit.

In strapdown navigation platforms, several gyros and accelerometers are mounted directly on the vehicle body. The set of gyros and/or accelerometers can sense three-axis vehicle angular rates. The rotor spin axis of the gyro is maintained in close coincidence with the spin-reference axis by a rebalance electronics system connected between the gyro signal generator and torque generator. Information of the angular motion about the input axis of the gyro is contained in the history of the torque current required to restrain or reposition the gyro about its output axis. The torque required to restore the position of the sensor output axis is generated by an input current which is divided into pulses of known amplitude, polarity, and duration. Each pulse represents an incremental rotation of the gyro about its input axis. To the extent that these increments are sufficiently small and the associated digital

computer has sufficient speed, an accurate calculation of system attitude change can be made.

The requirement of a precisely known weight for each torque pulse places a heavy burden upon the role played by the torque current generator in the pulse rebalance electronics. The function of the torque current generator is the following: (1) to regulate the magnitude of the torque pulse current by referencing it to a precision voltage reference and a high stability sampling resistor; (2) to torque scale or change the weighting of the torque pulses by changing the magnitude of the loop current; and (3) to translate a state in the logic section into a torque pulse polarity suitable for nulling the gyro's output error signal. This last function requires the torque current generator to contain an H-switch. The H-switch is a bridge arrangement, and must be bilateral in nature to allow current to be driven in both directions through the torquer of the gyro. The function of the H-switch then, is to route a precisely controlled current to the torquer.

Any pulse rebalance electronics system must of necessity depend heavily upon the stability, performance, and limitations of the torque current generator. The H-switch bridge is a key feature of the torque current generator. Any basic limitations in the performance of the H-switch will heavily degrade the performance of the torque current generator. The entire rebalance loop suffers as a result. Consequently, the performance of the torque current generator with special emphasis on the H-switch, is worthy of close study.



The design of the torque current generator is dependent upon the torquing method chosen for the pulse rebalance electronics loop. There are two commonly used schemes for current levels incorporated in pulse torquing methods (for example, see References 1 and 2). These are the binary and ternary methods. The binary torquing method supplies torquing current during each interrogation (or sample) period of such a polarity as to reduce the gyro output error signal. The ternary torquing method supplies current only during each interrogation period in which the error signal is greater in magnitude than a predetermined threshold level. If the error signal magnitude is less than the threshold level in a given sample period, the ternary method establishes a zero torque level condition. Two versions of each pulse torquing method are in existence. These are discrete-pulse torquing and width-modulated torquing methods. The torque current pulse is width-modulated in discrete steps in the width-modulated pulse torquing method.

The torque current generator to be discussed in this work was designed for use in a width-modulated binary pulse rebalance electronics loop for strapdown gyroscopes. More specifically, this work was part of a joint effort at the University of Tennessee's Department of Electrical Engineering under the auspices of N.A.S.A.'s Marshall Space Flight Center. The team, composed of Dr. T. V. Blalock, Dr. E. J. Kennedy, and the author, designed, implemented, and experimentally evaluated a new width-modulated pulse rebalance electronics loop. The development was based on previous studies by members of the team, as well as on studies in the latter contract period. The results of the team effort

were presented to N.A.S.A.'s Marshall Space Flight Center in a scientific report<sup>5</sup> dated July 13, 1973. The author's contribution, the torque current generator, will be presented in much greater detail in this work.

The scope of the work will be broadened to include topics not mentioned in the scientific report and research completed since that time.

## B. Scope of the Thesis

The purpose of this work is to design, construct, and test a torque current generator and to demonstrate its use in a closed-loop current generator. The generator is designed to provide a precise, well-regulated and scalable current pulse incorporated into the design such that the circuit may find application in other areas where a precise, well-regulated and scalable current pulse is needed.

For evaluation of the performance characteristics of the torque current generator, suitable criteria must be chosen as figures of merit. Steady-state accuracy, margins of stability against self-oscillation, temperature, aging, etc., and magnitudes of transient errors are of prime interest. Frequency and time domain characteristics, noise properties, and power consumption are among other items to be considered.

In Chapter II, design considerations for the torque current generator are discussed. The role of the torque current generator (TCG) in a width-modulated pulse rebalance electronics loop is presented. Design goals are enumerated, and design theory with some preliminary error analysis is detailed. Some implications resulting from the preliminary error analysis are investigated.

The implementation of the TCG is presented in Chapter III. Each functional block of the TCG is treated in detail. In some cases, engineering tradeoffs are indicated with reasons for the selection made.

Chapter IV introduces the analysis section of the thesis with a derivation of the loop transmission for the TCG loop. Also, criteria for evaluating the relative stability of the loop are selected. The relative stability of the TCG loop is then expressed in terms of these figures of merit.

Closed-loop frequency response and steady-state accuracy are calculated in Chapter V. The feedback network of the TCG as a function of frequency is considered. The feedback configuration of the TCG is simplified to facilitate the derivation of the closed-loop frequency response parameters. The steady-state actuating error of the loop is obtained as a figure-of-merit for steady-state dynamic accuracy.

Chapter VI continues the stability analysis of the TCG loop from Chapter IV. In this case, the stability problem is associated with temperature variations, component aging, and semiconductor device replacement.

A continuation of performance analysis of the TCG is found in Chapter VII. Time domain characteristics of the closed-loop voltage gain are discussed. Limitations on the usefulness of such characteristics for characterizing the TCG are briefly treated.

In Chapter VIII, offset and drift errors of the H-switch and precision voltage reference circuit are investigated. Also discussed in this chapter are errors due to transient feedthrough currents and unequal rise and fall times.

The low-frequency noise properties of the TCG are studied in Chapter IX. Noise generated in the loop is referred to the input of the comparator operational amplifier where the low-signal resolution of the circuit can be immediately recognized. Chapter IX completes the analysis section of the thesis.

Chapter X contains discussions of several possible modifications of the TCG. These modifications revolve mainly around the type of logic commanding the TCG and whether or not the +35V supply is present. The current range capability of the TCG is also investigated in Chapter X.

The principal experimental results are detailed in Chapter XI. The current waveform in the gyro torquer coil is the signal of prime interest. Several photographs of voltage and current waveforms at key points in the TCG loop are given.

A tabular summary of the principal results of the work is given in Chapter XII. Suggestions for further study are briefly discussed.

## CHAPTER II

### DESIGN CONSIDERATIONS FOR THE TORQUE

#### CURRENT GENERATOR

The torque current generator (often referred to as TCG in this thesis), has the distinction of being a most critical section of a pulse rebalance electronics loop for a strapdown gyro. It must be capable of supplying a current pulse of known amplitude, polarity, and duration to the gyro torquer to restrain or reposition the gyro about its output axis. Accuracy, stability, and reliability are of utmost importance in the design.

In order to fulfill its role in a pulse rebalance electronics loop for a strapdown gyro, the TCG must perform three separate but related tasks: (1) regulate the magnitude of the torque pulse current by referencing it to a precision voltage reference and a high stability sampling resistor; (2) change the weighting of the torque pulses by changing the magnitude of the TCG loop current; and (3) translate a state in the logic section into a torque pulse polarity. The TCG, as may be surmised from the last statement, is not a self-sufficient unit. Rather, it is designed to function as an integral part of a pulse rebalance electronics loop. At least two ports are needed in the TCG to receive scale factor and polarity commands from the logic section of the pulse rebalance electronics. For a better understanding of the role of the torque current generator in the overall performance of the pulse rebalance electronics loop, a short discussion on the entire loop is warranted.

#### A. The Torque Current Generator in Perspective

The torque current generator treated in this work is a part of a width-modulated binary pulse rebalance electronics loop for strapdown gyroscopes. The entire loop was a team effort, the TCG being the author's contribution to that effort. The basic elements of a width-modulated binary rebalance loop are illustrated in Figure 2.1. Figure 2.2 is a block diagram of the rebalance electronics developed at the University of Tennessee's Department of Electrical Engineering. Figures 2.1 and 2.2 were taken from the scientific report listed as reference 5. Reference to these figures will be helpful in the brief discussion of the operation of the rebalance loop which follows.

The proper place to begin a discussion on the operation of a rebalance electronics loop for a strapdown gyroscope is at the gyroscope. The gyroscope is attached directly to the vehicle body, and senses a degree of attitude change experienced by the vehicle. (For sensing three degrees of attitude change, three strapdown gyroscopes with their associated rebalance electronics loops are necessary). The attitude change of the vehicle becomes an input angular rate to the gyro. The gyro's signal generator is excited by a sinusoidal signal. The gyro pickoff, (see Figure 2.1), is designed such that the error signal is the sinusoidal excitation signal amplitude-modulated by the angular displacement of the gyro float.

The AC amplifier block immediately follows the gyro pickoff. This block consists of an AC preamplifier, bandpass filter, and an AC amplifier. The high-input impedance preamplifier receives the error signal

ORIGINAL PAGE IS  
OF POOR QUALITY

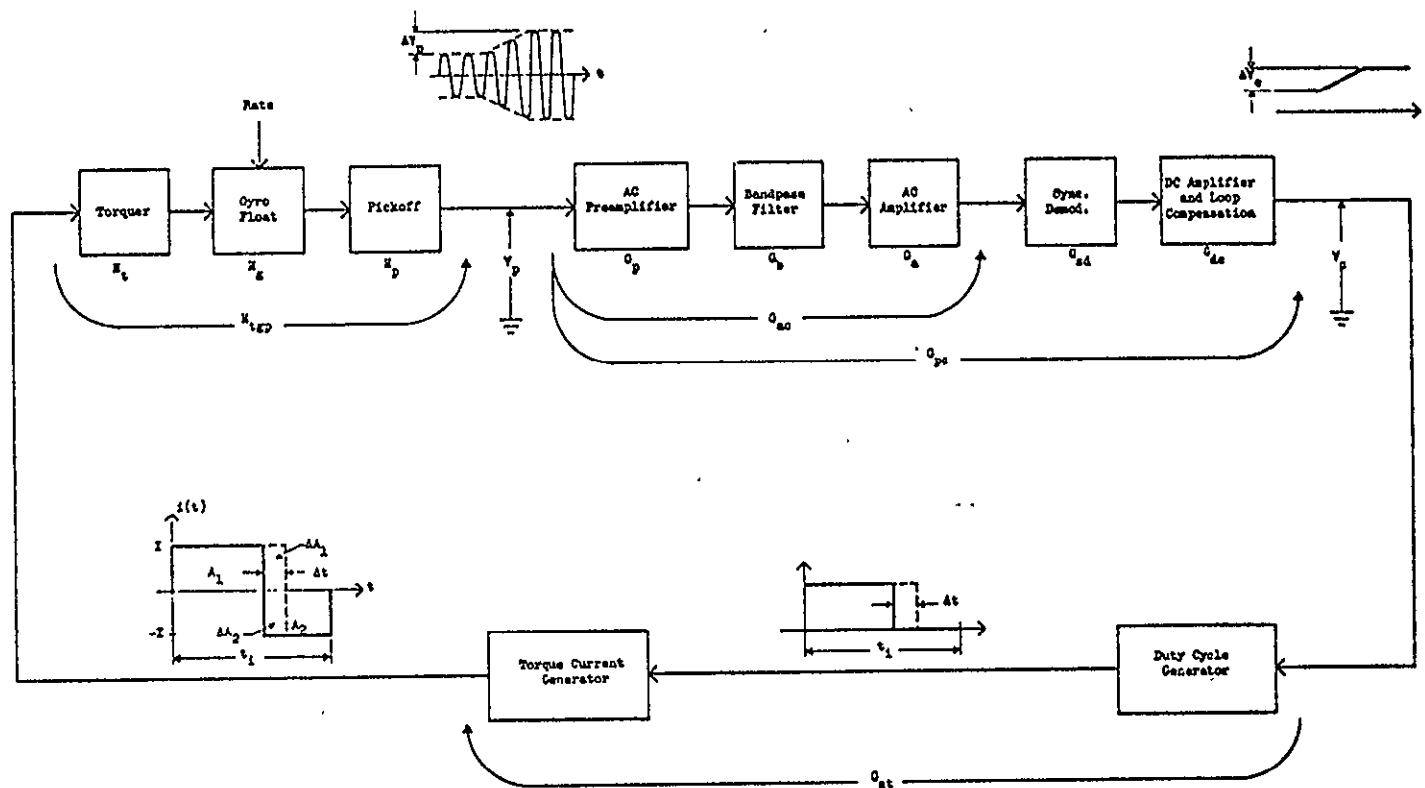


FIGURE 2.1

THE BASIC ELEMENTS OF A WIDTH-MODULATED BINARY REBALANCE LOOP

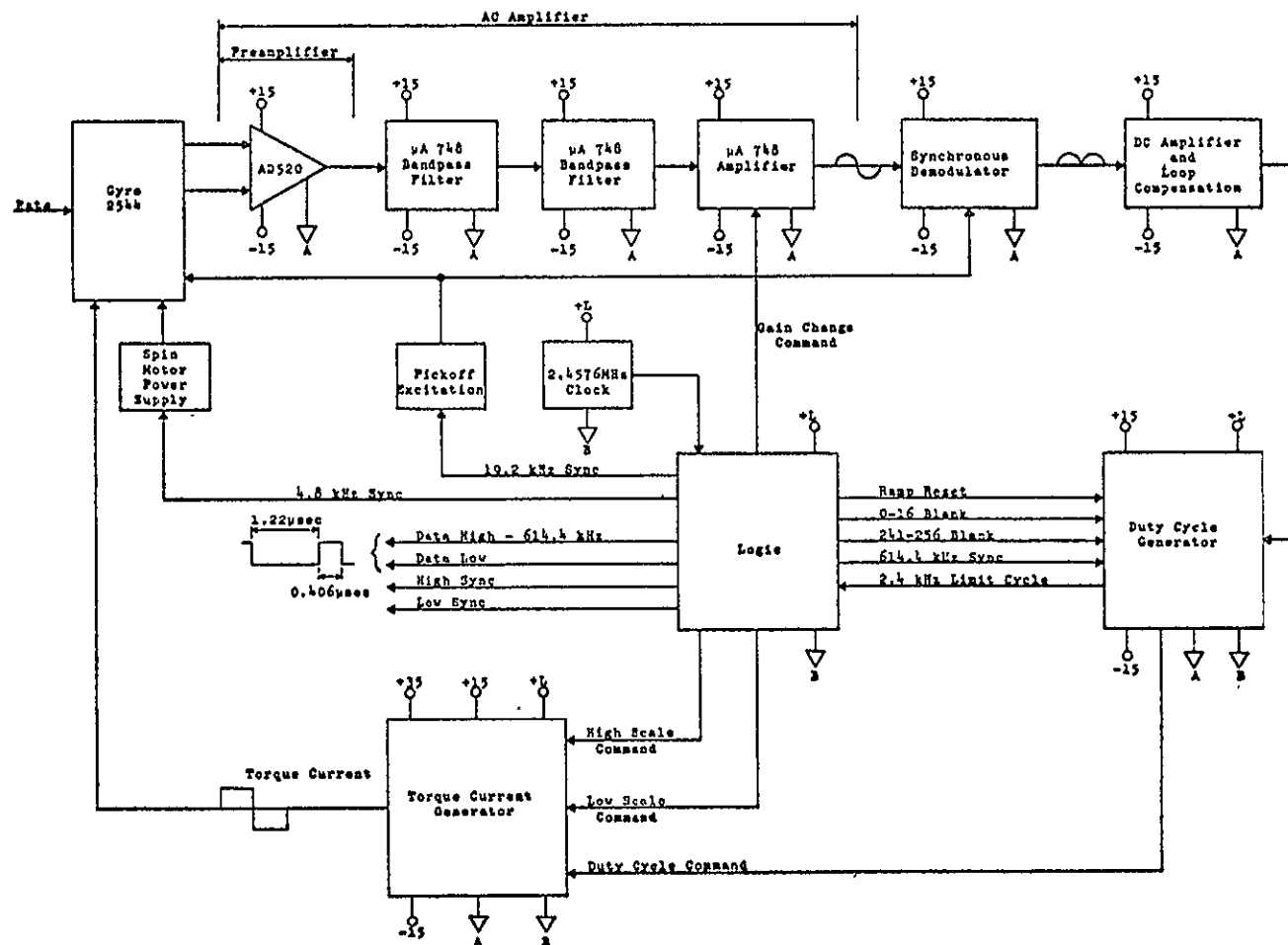


FIGURE 2.2

U.T. REBALANCE ELECTRONICS - BLOCK DIAGRAM



from the gyro pickoff, and removes common-mode signals contaminating the error signal. The output of the preamplifier feeds a bandpass filter which further improves the signal-to-noise ratio of the amplified error signal. The AC amplifier output stage following the bandpass filter has the capability of accommodating a range of gain requirements, and it also has a gain switching facility for scale factor changes<sup>5</sup>.

The sinusoidal AC output of the AC amplifier is fed into a synchronous demodulator. Here the processed error signal is converted to a DC output, the polarity being determined by the signal generator of the gyro.

The synchronous demodulator is followed by a DC amplifier section. The function of this section is to provide any additional electronic gain needed and to shape the overall rebalance loop transmission for adequate system stability.

The duty cycle generator receives the processed error signal from the DC amplifier section and mixes it with a ramp signal. The duty cycle generator determines when the composite signal crosses a threshold, and uses this information to proportion the torque current between positive and negative values. The duty cycle generator sends a limit cycle signal to the logic section which carries the torquing rate information. Blank-ing signals are sent from the logic section to the duty cycle generator to set lower bounds on the duration of positive and negative torque currents. The duty cycle generator also receives a sync signal from the logic section. These signal paths are illustrated in Figure 2.2.

The functions performed by the logic section of the rebalance loop are amply illustrated in Figure 2.2. At the time of presentation of the scientific report<sup>5</sup> from which Figure 2.2 was taken, the logic being used in the rebalance loop was the Hamilton Standard TTL logic discussed in reference 1. The rebalance loop was designed primarily for use with CMOS logic. However, the design is sufficiently versatile to work well with 5V TTL logic.

The TCG completes the listing of the basic elements of a width-modulated binary rebalance loop. It receives scale factor commands from the logic section, torque current pulse polarity and duration commands from the duty cycle generator, and sends a corresponding torque current pulse to the torquer coil of the gyro.

From the above discussion, the rebalance electronics loop can be seen as a system performing a three-fold function. First, it senses movement of the gyro float from its quiescent position. Secondly, it generates pulses of torque current to restore the float to its quiescent position. Thirdly, a data train is sent from the logic section in the rebalance loop to a digital computer where vehicle attitude changes are computed. For the vehicle to be where the computer thinks it is, each section in the rebalance loop must perform its function properly. This is particularly true of the torque current generator.

#### B. Design Goals for the Torque Current Generator

The TCG is in one sense a regulated current power supply. Classically, a constant current power supply is a regulated power supply that

acts to maintain its output current constant in spite of changes in load, line, temperature, etc.<sup>6</sup> Ideally, the current source would have an infinite internal impedance. Also, it would be able to produce an infinite voltage if open circuited.<sup>7</sup> Obviously the output characteristics of a regulated current supply are the dual of the output characteristics of a regulated voltage supply. A practical current regulator is bounded by a maximum open circuit voltage and only approximates the current source characteristics.

A TCG for a strapdown gyro is more than a common current regulator. True, it must regulate its output current precisely. In addition, it must be capable of scaling its output current and changing the direction of the current through the load in response to commands from other sections of the rebalance electronics. In this last respect, the TCG exhibits a characteristic similar to a pulse-width-modulated DC servo amplifier, such as one described in reference 8.

The functions to be performed by a TCG for strapdown gyroscopes have been briefly discussed above. From this discussion, several design considerations for a TCG become apparent.

Stability of the TCG against self-oscillation, temperature, aging, etc., is at the top of the list of design goals. If the TCG were in an unstable state with regard to oscillations, it would be useless as a functional block in a pulse rebalance electronics system. Sufficiently large gain and phase margins are a must. Minimum bias, offset, and drift errors are desirable.

After stability, the criterion of accuracy is next in importance as a design consideration. The output of the TCG must be current pulses with well-defined amplitude, polarity, duration, and shape. Mode switching with a minimum loss of data pulses to the computer is desirable. The generator should be free of random moding (this is hardly a problem in a width-modulated binary system). A high degree of steady-state accuracy requires a high loop gain at low frequencies.

Another design consideration is reliability. Component types must be carefully selected, and exhaustive testing under worst case conditions is needed. Reliability, stability, and accuracy form a three-fold primary design consideration for the TCG. Other design goals need to be considered, but they must not encroach upon the reign of the triumvirate of stability, accuracy, and reliability as design criteria.

Other salient design considerations for the TCG are simplicity, versatility, power consumption, and packaging density. All other things being equal, the more simple the circuit in component count, the more reliable it should be. The generator should be versatile enough to have a dual scale factor capability over a wide range of current levels. It should be capable of being used with many different gyros, and with either TTL or CMOS logic sections. Power consumption should be kept at a minimum consistent with other design constraints. Packaging density should be such as to make microcircuit implementation of the circuit a facile task.

Additional design goals, such as the reduction of the number of power supplies necessary to supply the TCG, are significant. However,

they are deemed by the author to have less weight in the overall design of the TCG than those criteria already discussed. Such goals are to be realized whenever possible without degrading the more important features of the design.

The principal design criteria for a TCG for strapdown gyroscopes have been enumerated above. Next, design theory in the form of some preliminary error analysis will be presented.

### C. Design Theory - Preliminary Error Analysis

A simplified block diagram of a TCG to perform the functions described earlier in this work is illustrated in Figure 2.3. For accuracy, it is absolutely essential that the sampling resistor sense exactly the same current that passes through the gyro torquer coil. In a practical application this is impossible, but the circuit must approach the ideal situation to achieve the acceptable degree of accuracy. Any source of error must be carefully investigated and minimized whenever possible.

A preliminary analysis of errors resulting from bias and scale factor currents and "on" voltages of the switching elements in the H-switch can be made without specifying semiconductor components. The analysis which follows is taken mainly from reference 1.

#### Error Due to Lower H-switch Elements

Reference to Figure 2.3 indicates that when semiconductor switch S3 is "on" switch S4 should be "off". The reverse situation is true when S4 is on. For a given torquing mode, a desirable feature of the design is to have the currents passed by the two switches be equal in magnitude,

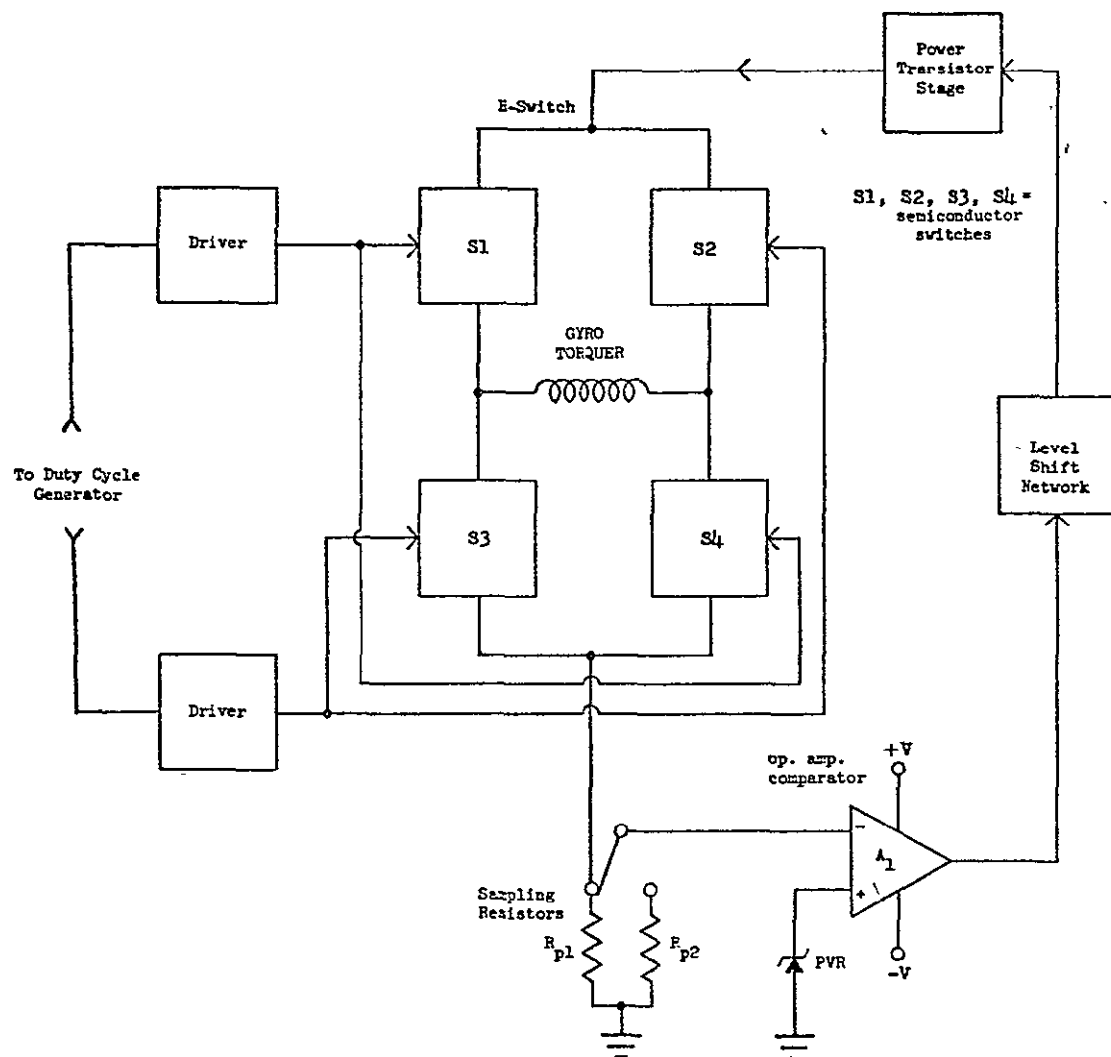


FIGURE 2.3

BLOCK DIAGRAM OF A TORQUE CURRENT  
GENERATOR FOR STRAPDOWN GYROSCOPES

but occurring at different times. Since semiconductor switches are generally bipolar or FET devices, they are either current or voltage controlled devices. Consequently, the current passed by the semiconductor switch is dependent upon either a voltage or current drive supplied to the switching element. The first error to be investigated is related to the drive signal supplied to the lower H-switch switching elements.

The lower H-switch drive signals are assumed to be drive currents and are illustrated in Figure 2.4. In Figure 2.4,  $T_s$  is the sample period, and  $I_a$  and  $I_b$  are the amplitudes of  $i_1$  and  $i_2$  respectively. The gyro rebalance loop is assumed to be a width-modulated binary loop, and the indicated input rate of the gyro is assumed to be zero. Under these conditions, the duty cycle of each switch under consideration should be 50%.

The existence of variations in drive currents to the lower H-switch switching elements produce scale factor and bias current errors. In order to obtain expressions for these errors, it is helpful to represent  $i_1$  and  $i_2$  as DC currents and employ the time function<sup>9</sup>  $F_s$ , where

$$F_s = \left( \frac{4}{\pi} \right) \sum_{n=1}^{\infty} \left( \frac{1}{2n-1} \right) \sin(2n-1) \omega_s t \quad (2.1)$$

The graph of  $F_s$  is a square wave with an amplitude of  $\pm 1$  and a frequency of  $\omega_s$ .  $\omega_s$  is  $2\pi/T_s$ , where  $T_s$  is the sampling period. The function has a zero mean value. An equivalent circuit of the current regulator and H-switch sections of the TCG is shown in Figure 2.5. This circuit assumes the upper H-switch switching elements to be ideal.  $A_1(s)$  is the transfer

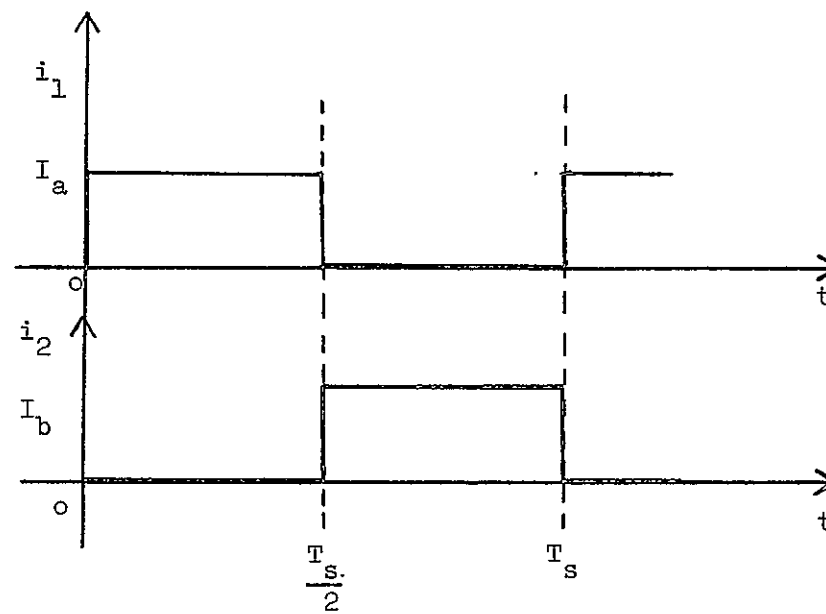
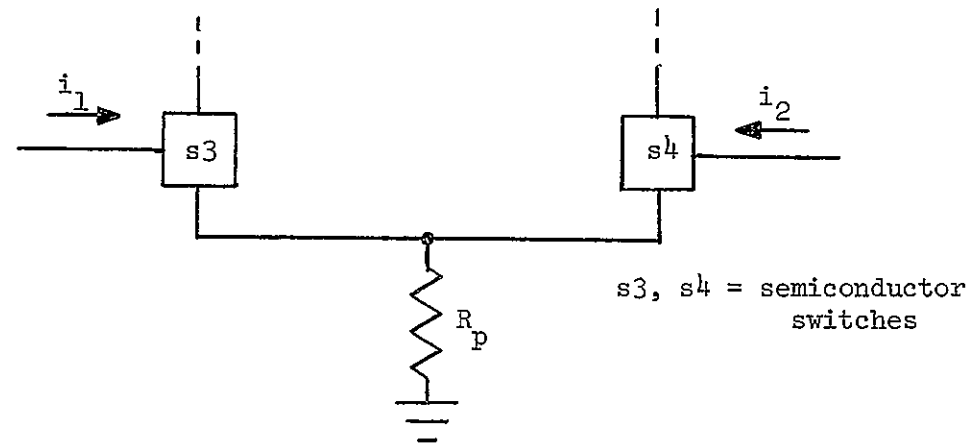
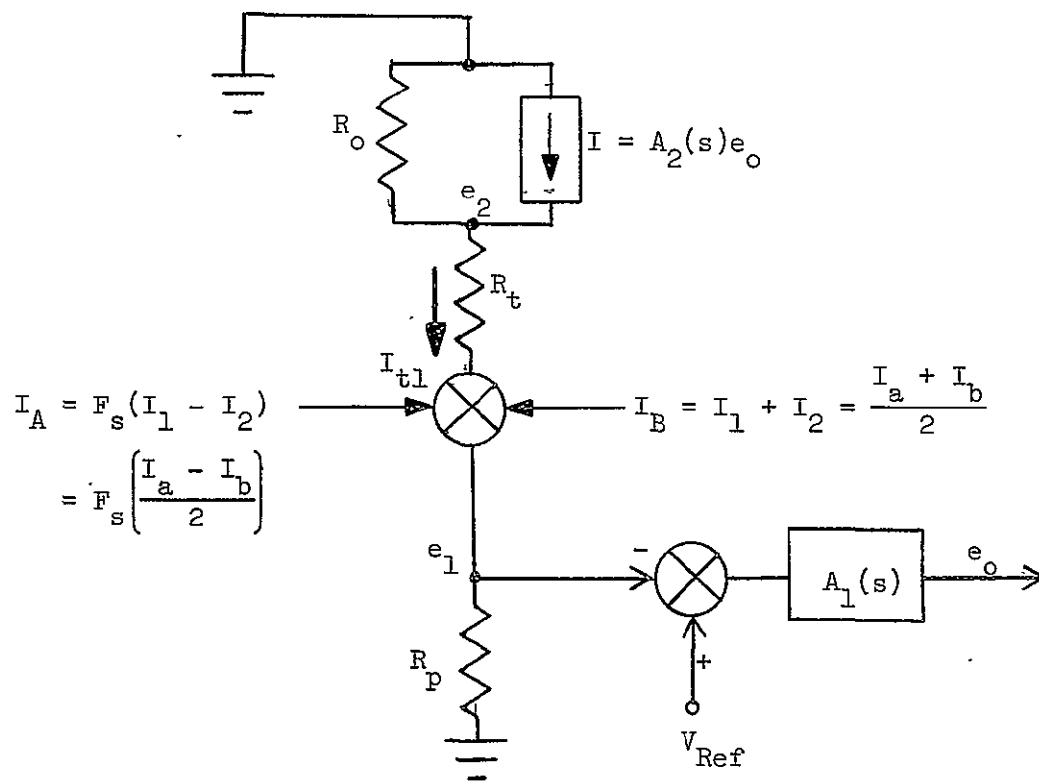


FIGURE 2.4

LOWER H-SWITCH ELEMENTS AND  
THEIR ASSOCIATED DRIVE CURRENTS





Note: 
$$I_1 = \frac{1}{T_s} \int_0^{T_s} i_1 dt = \frac{I_a}{2} ;$$

$$I_2 = \frac{1}{T_s} \int_0^{T_s} i_2 dt = \frac{I_b}{2} .$$

FIGURE 2.5

AN EQUIVALENT CIRCUIT OF THE CURRENT REGULATOR  
AND H-SWITCH SECTIONS OF THE TORQUE CURRENT GENERATOR

function from the input of the op. amp. comparator to the output.  $A_2(s)$  is the transfer function from the output of the op. amp. to the output of the current regulator.

The current through the torquer (assumed to be compensated and represented by  $R_t$ ) is shown in Figure 2.5, as  $I_{t1}$ . As a result of the switching action of the H-switch, the actual load current,  $I_t$ , is related to  $I_{t1}$  according to the equation

$$I_t = F_s I_{t1} . \quad (2.2)$$

The H-switch current can be found by standard circuit analysis, and is detailed in Appendix A.

$$I_{t1} = \frac{R_o A_1(j\omega) A_2(j\omega) V_{Ref}(\omega) - [I_A(\omega) + I_B(\omega)] [R_p + R_o R_p A_1(j\omega) A_2(j\omega)]}{R_o + R_p + R_t + R_o R_p A_1(j\omega) A_2(j\omega)} . \quad (2.3)$$

When  $\omega = 0$ , or for DC currents, the current through the torquer corresponds to scale factor errors. The current  $I_{t1}$  under these conditions is given by

$$I_{t1}(\omega=0) = \frac{R_o A_1(o) A_2(o) V_{Ref} - \left[ \frac{I_a + I_b}{2} \right] [R_p + R_o R_p A_1(o) A_2(o)]}{R_o + R_p + R_t + R_o R_p A_1(o) A_2(o)} . \quad (2.4)$$

In Equation (2.4),  $V_{Ref}(\omega) = V_{Ref}$ ,  $I_A(\omega) = 0$ , and  $I_B(\omega) = \frac{I_a + I_b}{2}$ .  $R_o$  is normally large due to feedback effects.  $A(o) = A_1(o) A_2(o)$  is required to be quite large for steady state accuracy. The other parameters in Equation (2.4) are small compared to  $R_o$  and  $A(o)$ . Consequently, Equation (2.4) can be reduced to

$$I_{t1}(\omega=0) = \frac{V_{Ref}}{R_p} - \left( \frac{I_a + I_b}{2} \right). \quad (2.5)$$

Ideally,  $I_{t1}(\omega=0)$  should be equal to  $V_{Ref}/R_p$ . The error indicated in Equation (2.5) is a scale factor error and corresponds to changes in the reference voltage.

An error in the bias current of the torquer is also present as a result of drive currents to the lower H-switch switching elements. The procedure used to find this error is as follows: for  $\omega \neq 0$ , set  $V_{Ref}(\omega)=0$ , and  $I_B(\omega)=0$ ; with these sources of DC current removed, rewrite Equation (2.3), and analyze the equation to see what DC components exist as a result of the  $I_A(\omega)$  drive current. With  $V_{Ref}(\omega)=0$  and  $I_B(\omega)=0$ , Equation (2.3) becomes

$$I_{t1} = \frac{-I_A(\omega) \{R_p [1 + R_o A(j\omega)]\}}{R_o + R_p + R_t + R_o R_p A(j\omega)}. \quad (2.6)$$

In Equation (2.6),  $A(j\omega) = A_1(j\omega) A_2(j\omega)$  as indicated in Figure 2.5,

$$I_A(\omega) = F_s \left( \frac{I_a - I_b}{2} \right). \quad (2.7)$$

Substitution of Equation (2.1) into Equation (2.7) and the result into Equation (2.6) yields Equation (2.8).

$$I_{t1}(\omega) \Big|_{\omega=n\omega_s} = \frac{2(I_b - I_a)}{\pi} \sum_{n=1}^{\infty} \left( \frac{1}{2n-1} \right) A_n \sin[(2n-1)\omega_s t + \phi_n], \quad (2.8)$$

where

$$A_n = \left| \frac{R_p [1 + R_o A(j\omega)]}{R_o + R_p + R_t + R_o R_p A(j\omega)} \right|_{\omega = n\omega_s} ; \phi_n = \angle \frac{R_p [1 + R_o A(j\omega)]}{R_o + R_p + R_t + R_o R_p A(j\omega)}_{\omega = n\omega_s}$$

The actual torquer current,  $I_t$ , is the parameter of interest in the calculation of the bias current.  $I_t$  may be found by substituting Equation (2.8) into Equation (2.2). The result is

$$I_t = \frac{8(I_b - I_a)}{\pi^2} \sum_{m=1}^{\infty} \left( \frac{1}{2m-1} \right) \left\{ \sum_{n=1}^{\infty} \left( \frac{A_n}{2n-1} \right) \sin[(2n-1)\omega_s t + \phi_n] \right\} \sin(2m-1)\omega_s t. \quad (2.9)$$

By definition, the bias current is the DC torquer current when the gyroscope indicates zero rate input. The DC current components of Equation (2.9) are given in Equation (2.10).

$$I_t(\text{DC}) = \frac{4(I_b - I_a)}{\pi^2} \sum_{n=1}^{\infty} \frac{A_n}{(2n-1)^2} \cos \phi_n. \quad (2.10)$$

The factor  $A_n \cos \phi_n$  in Equation (2.10) is the real part of the complex factor used in Equation (2.8). Consequently, the bias current can be expressed as

$$I_t(\text{DC}) = \frac{4(I_b - I_a)}{\pi^2} \sum_{n=1}^{\infty} \frac{B_{2n-1}}{(2n-1)^2}, \quad (2.11)$$

where

$$B_n = R_e \left\{ \frac{R_p [1 + R_o A(j\omega)]}{R_o + R_p + R_t + R_o R_p A(j\omega)} \right\} \bigg|_{\omega=n\omega_s} .$$

$R_o$  and  $A(j\omega)$  are large compared to  $R_t$  and  $R_p$  at the frequencies of interest. As a result,  $B_n$  in Equation (2.11), reduces to unity. The approximate bias current due to the drive currents of the lower H-switch switching elements is then

$$I_t(\text{DC}) \approx \frac{4(I_b - I_a)}{\pi^2} \sum_{n=1}^{\infty} \frac{1}{(2n-1)^2} = \frac{(I_b - I_a)}{2} . \quad (2.12)$$

The scale factor error and bias current error, both due to drive signals to the lower H-switch switching elements, have been expressed in Equation (2.5), and Equation (2.12), respectively. These errors are not corrected by the current regulator section of the torque current generator.

#### Error Due to Upper H-switch Elements

The scale factor and bias error currents due to drive currents of the upper H-switch switching elements are calculated in the same manner as those due to the lower switching elements. The necessary equivalent circuit is shown in Figure 2.6. The results, again taken from Reference 1, are given in Equations (2.13) through (2.15).

$$I_{tl}(\omega) = \frac{R_o [I_A(\omega) + I_B(\omega) + A(j\omega)V_{\text{Ref}}(\omega)]}{R_o + R_p + R_t + R_o R_p A(j\omega)} . \quad (2.13)$$

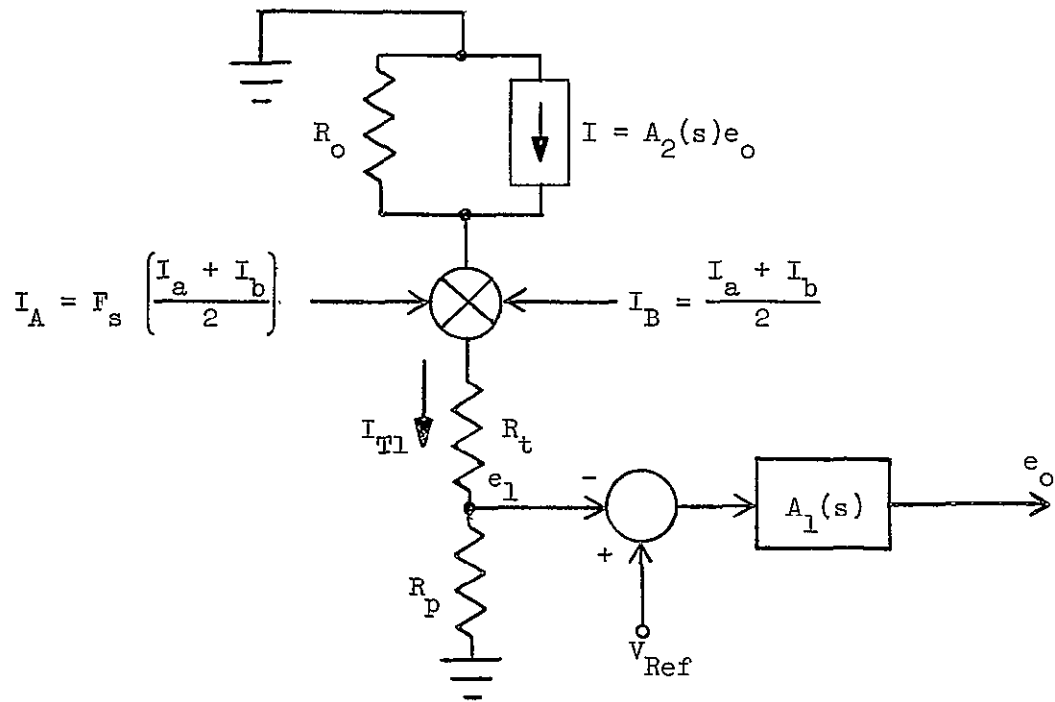


FIGURE 2.6

AN ADDITIONAL EQUIVALENT CIRCUIT OF THE CURRENT REGULATOR  
AND H-SWITCH SECTIONS OF THE TORQUE CURRENT GENERATOR

$$I_{t1}(\omega=0) = \left( \frac{I_a + I_b}{2} \right) \left[ \frac{1}{R_p A(j\omega)} \right] + V_{Ref}/R_p . \quad (2.14)$$

$$I_t(DC) = \frac{4(I_b - I_a)}{\pi^2} \sum_{n=1}^{\infty} R_o \frac{B(2n-1)}{(2n-1)^2} , \quad (2.15)$$

where

$$B_n = R_e \left\{ \frac{1}{R_o + R_p + R_t + R_o R_p A(j\omega)} \right\} \bigg|_{\omega=n\omega_s} .$$

The current regulator corrects for these errors. Consequently, the actual error currents are functions of the TCG frequency response.

#### Error Due to "ON" Voltage

As mentioned earlier, the H-switch is a bridge arrangement and consists of two semiconductor switches in each leg. The "ON" voltage of any one of the switches may differ from that of the other three. Such an unbalance in the ON voltages of the switching elements in the H-switch will result in a bias current error in the torquer.

In Reference 1, the unbalance in the ON voltages of the four semiconductor switches in the H-switch was represented by a square wave voltage source in series with  $R_t$ . The peak value of the source was  $V_o$ . The result of the calculations for bias current was

$$I_t(DC) = \left( \frac{8}{\pi^2} \right) V_o \sum_{n=1}^{\infty} \frac{B(2n-1)}{(2n-1)^2} , \quad (2.16)$$

where

$$B_n = R_e \left\{ \frac{1}{R_o + R_p + R_t + R_o R_p A(j\omega)} \right\} \bigg|_{\omega = n\omega_s}$$

The torque current generator corrects for the voltage unbalance in the H-switch. Again, the actual bias current error due to the voltage unbalance is a function of the frequency response of the TCG.

A preliminary error analysis involving unbalances in drive signals and ON voltages of the switching elements of the H-switch has been discussed in this section. Next, a brief discussion on the implications of this error analysis concerning the design of the TCG will be presented.

#### D. Design Implications from the Preliminary Error Analysis

The most distressing results of the preliminary error analysis are the errors in scale factor and bias currents due to an unbalance in the drive currents of the lower H-switch elements. The TCG does not correct for these errors. This situation makes it imperative that great care be taken to choose switching elements for the H-switch that minimize these errors.

The use of simple bipolar transistor switches is all but prohibited by the magnitude of the resulting errors due to the drive currents to the lower H-switch elements. By way of example, consider the lower switching elements of the H-switch to be bipolar transistors with a current gain ( $\Delta I_C / \Delta I_B$ , or Beta) of 100 at  $I_C = 30$  mA and  $V_{CE} = 1$  V. The magnitude of the drive current to each of the lower switching elements would be



$I_B = I_C/\beta = 300 \mu A$ . This information, coupled with Equation (2.5), gives a scale factor error of  $10^4$  ppm. Further suppose that there is a 5% variation in the drive currents necessary to turn the lower H-switch switching elements "ON". The result, from Equation (2.12), is a 250 ppm bias error due to the unbalance in the drive current to the lower H-switch switches. The values in this example do not include transient effects or temperature effects. However, the example does illustrate that under these circumstances there is a considerable difference between the current sensed by the sampling resistor and the current through the torquer.

An obvious partial solution to the problem associated with drive currents to the H-switch switches is a semiconductor switch that draws very little current from the H-switch driver circuit. Except for its lack of sufficient speed at the present time, the optical isolator might find an application here. The best solution for the problem appears to be a switch labeled by one author<sup>10</sup> as a composite field-effect-bipolar transistor. Such a composite transistor consisting of a p-channel MOSFET and an NPN bipolar transistor is shown in Figure 2.7. The drive signal to the composite device is a voltage since the FET is a voltage controlled device. MOSFETs are available with a maximum gate current of 10 pA. The drive current to the bipolar is the drain current of the FET, and passes through the torquer as well as the current sampling resistor. This should minimize the scale factor error.

Matching of components to be used in the four switches of the H-switch is very important from the standpoint of bias current error. With

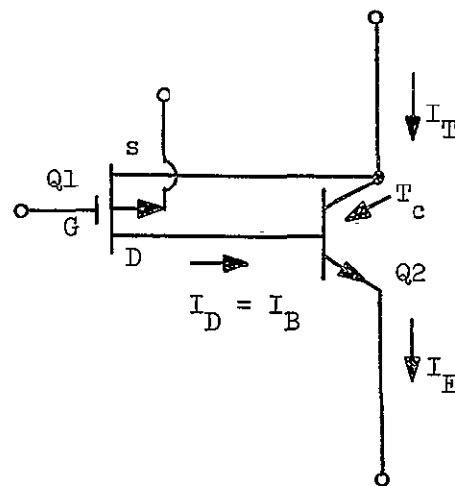


FIGURE 2.7

A COMPOSITE FIELD-EFFECT-BIPOLAR TRANSISTOR

reference to Figure 2.7, the following relationship holds.

$$I_E = I_B + I_C = I_D + I_C \approx I_t \quad . \quad (2.17)$$

The MOSFET in the circuit of Figure 2.7, will operate in either the OFF or ON state, the ON state being the ohmic region. The bipolar will operate in either the OFF or the ACTIVE region. Note that it is impossible for the bipolar to saturate in this configuration since base current flow through the ON resistance of the FET keeps the base-collector junction reverse-biased. For drain-to-source voltages well below pinch-off, the drain current of the MOSFET may be expressed as<sup>11</sup>

$$I_D = K_1 V_{DS} \left[ (V_{gs} - V_T) - \frac{V_{DS}}{2} \right] \quad . \quad (2.18)$$

In Equation (2.18),  $K_1$  is a constant depending upon the geometry of the device. Obviously, any variation in the parameters of Equation (2.18) from one device to another will cause a variation in  $I_D$ , and consequently in  $I_t$ . However, the variations in  $I_t$  are also those of  $I_E$ . Consequently, these variations in  $I_t$  are also present in the current sensed by the sampling resistor. The TCG can partially correct for this error.

A brief examination of Equations (2.15) and (2.16), indicates that the same infinite series appears in both equations. The terms of the series are dependent upon the TCG impedances and frequency response. The magnitude of each term in the series  $B_n$  is the real part of a function. Hence,  $B_n$  can be minimized if the function is made to have a value which is mostly imaginary. This will be the case if the frequency response of

the TCG has a single pole.<sup>1</sup> This may not be possible and be consistent with other design constraints. However, it is a desirable design criterion for minimizing bias current errors due to unbalances in ON voltages and upper H-switch drive currents.

Design considerations for the TCG have been discussed in this chapter. While the discussion has not been all inclusive, many prominent, desirable features of the TCG have become apparent. These features are design goals to be realized in the physical circuit to be implemented. The implementation of the TCG will be presented in the next chapter.

## CHAPTER III

### TORQUE CURRENT GENERATOR IMPLEMENTATION

The TCG illustrated in Figure 3.1 is the result of an effort to design a near optimum, yet versatile, TCG for use in strapdown sensor systems. An attempt has been made to incorporate the best aspects of previously published torque current generators as well as the inclusion of improved solid state devices. As many as possible of the design goals discussed in Chapter II have been realized in the implementation of the circuit.

The TCG consists of a DC feedback loop containing the following: a precision Zener diode driven by a constant current source and serving as a precision voltage reference; a comparator operational amplifier; an error amplifier serving as a level shifter; a power transistor which functions as the output stage of the current regulator; an H-switch; an H-switch driver; two precision sampling resistors with a sampling resistor switching network; a TTL to CMOS interfacing circuit; and torquer compensation. Each of these functional blocks will now be discussed.

#### A. The Precision Voltage Reference

The application here requires a precision voltage reference with ultra-high stability of voltage over changes in time and temperature. The most important component in the precision voltage reference is the reference diode. The reference diode is made possible by exploiting the differing thermal characteristics of forward- and reverse-biased silicon



p-n junctions. A forward-biased junction has a negative temperature coefficient of approximately  $2 \text{ mV}/^\circ\text{C}$ . Reverse-biased junctions have positive temperature coefficients ranging from approximately  $2 \text{ mV}/^\circ\text{C}$  at  $5.5 \text{ V}$  to  $6 \text{ mV}/^\circ\text{C}$  at  $10 \text{ V}$ .<sup>12</sup> By a judicious combination of forward- and reverse-biased junctions, a device can be fabricated with a very low overall temperature coefficient. After assembly, some of the devices within a lot may be overcompensated while others may be undercompensated. For this reason, the device reference voltage may change in either the negative or positive direction. Manufacturers of reference diodes generally specify a maximum  $\Delta V_z$  over a given temperature range. Sometimes the temperature stability of Zener voltage is expressed as a temperature coefficient. The temperature coefficient is usually defined as the percent voltage change across the device per degree Celsius. This method accurately reflects the voltage deviation at the test temperature extremes, but not necessarily at other points within the specified temperature range. This phenomenon is due to variations in the rate of voltage change with temperature for the forward- and reverse-biased dice of the reference diode.<sup>12</sup>

An MZ 605, with its voltage-time stability of  $5 \text{ ppm}/1000 \text{ hr.}$  and voltage-temperature stability of approximately  $5.4 \text{ ppm}/^\circ\text{C}$ , could have been used for the precision reference diode. However, due to economics and resolution of available measuring instruments, a 1N829A was chosen as a reasonable substitute. (A reference voltage of  $6.2 \text{ V}$  was chosen because the lowest discrete temperature-compensated Zener diode is rated at  $6.2 \text{ V}$ .<sup>13</sup>) This Zener reference diode has an average temperature

coefficient over the operating temperature range of 5 ppm/°C. As mentioned above, the reference diode temperature coefficient is not a linear coefficient, and accurately reflects the voltage deviation at test temperature extremes only. However, the maximum  $\Delta V_z$  over the operating temperature range is specified as 5mV. This translates into a voltage-temperature stability of  $\pm 5.20$  ppm/°C. Voltage-time stability, although not specified, is typically better than 100 ppm/1000 hr. of operation.<sup>14</sup> In addition, the diode has a low dynamic impedance and a silicon oxide passivated junction for long-term stability.

In the discussion of voltage-temperature stability above, an underlying assumption was made that current remained constant. A significant change in the temperature coefficient of a reference diode usually occurs with a deviation above or below the test current specified. It is not necessary, however, that a reference diode be operated at the specified test current. New voltage-temperature characteristics for a change in current may be obtained by superimposing the  $I_z$  versus  $\Delta V_z$  data curve upon the  $\Delta V_z$  versus ambient temperature curve.<sup>12</sup> On the average, more voltage variation is due to current fluctuation than is due to temperature variation.<sup>14</sup> Hence, once the diode current is chosen, this current must be supplied by a constant current source if a truly stable reference source is desired.

The circuit composed of Q16, D4 and R3 in Figure 3.1, is a constant current source to drive D1, the reference diode. Q16 is a type 2N5245 N-channel junction field-effect transistor. The FET has three distinct characteristic regions, although only two of them are operational.



Below the pinch-off voltage,  $V_p$ , the FET operates in the ohmic or resistance region. Above the pinch-off voltage and up to the drain-source breakdown voltage,  $BV_{DSS}$ , the device operates in the constant-current region, or saturated region. The third region is above the breakdown voltage. This region, where the FET is not operated, is called the avalanche region. For the application of driving the reference diode, the constant-current region is the region of interest.

An FET with the gate and source shorted operates at  $I_{DSS}$ , the zero-bias drain current. With the addition of a source resistor and diode as indicated in Figure 2.1, the circuit becomes capable of supplying any current below  $I_{DSS}$ . Resistor R3 in Figure 3.1 was adjusted to give an  $I_D$  of 7.5 mA, the test current specified for the reference diode. The circuit output conductance<sup>15,16</sup> is

$$g_o = \frac{g_{os}}{1 + R_s(g_{os} + g_{fs})} \approx \frac{g_{os}}{1 + R_s g_{fs}}, \quad (3.1)$$

where  $g_{fs}$  and  $g_{os}$  are the real parts of the short-circuit forward transfer and output admittances respectively.  $R_s$  is the combination of the padding resistor R3 and the dynamic impedance of the diode D4. At low frequencies  $g_{os}$  is equal to  $y_{os}$ . R3 is approximately  $25\Omega$ , and the dynamic impedance of the diode, D4, is approximately 3.4 ohms.  $R_s$  is typically 28.4 ohms. From manufacturers' data,  $g_{os} \approx 0.012$  mmho and  $g_{fs} \approx 5$  mmho under the operating conditions of this circuit. These values, when substituted into Equation (3.1) yield an output conductance of approximately 10.5 micromhos for the FET constant-current source. The equivalent output resistance is approximately 95.2 k $\Omega$ .

For the FET constant-current source to have a zero temperature coefficient, (OTC), the FET must be operated at a specific current,  $I_{DZ}$ , the drain current for OTC.  $I_{DZ}$  is given by <sup>17</sup>

$$I_{DZ} \approx I_{DSS} \left( \frac{0.63}{V_p} \right)^2. \quad (3.2)$$

$V_p$  in Equation (3.2) is the pinch-off voltage of the FET. The gate-source bias voltage required is

$$V_{gsz} \approx V_p - 0.63. \quad (3.3)$$

Operation of the FET at  $I_D < I_{DZ}$ , but near  $I_{DZ}$ , will give a positive temperature coefficient. Negative temperature coefficients result if  $I_D > I_{DZ}$ .<sup>15,16</sup> The FET constant-current source driving the reference diode is biased at  $I_D > I_{DZ}$ .  $I_D$  tends to decrease with increasing temperature. However, as  $I_D$  decreases, the ohmic drop  $I_D R_3$  decreases. Also, the forward voltage drop,  $V_f$ , across the diode,  $D4$ , decreases at approximately 2mV/°C. The gate-to-source voltage of the FET can be written as

$$V_{gs} = -(I_D R_3 + V_f). \quad (3.4)$$

Analyzing Equation (3.4) shows that  $V_{gs}$  increases as  $I_D$  and  $V_f$  decrease. An increase in  $V_{gs}$  for an N-channel JFET results in an increase in the drain current. Hence, the FET constant-current source under discussion should have good bias stability with respect to temperature change.

An additional advantage of using the FET constant-current source to supply the reference diode is one of tremendous decoupling of either

ripple or noise on the 15V supply line. The maximum dynamic impedance of the IN829A reference diode is 10 ohms. The estimated dynamic impedance of the current source was approximately 95.2 k $\Omega$ . Due to the high ratio of the dynamic impedance of the current source to that of the reference diode, an attenuation of approximately 80 dB can be realized at frequencies up to several hundred kHz.

The main disadvantage of FETs is capacitance between gate and source, and gate and drain. These capacitances are detrimental to high-frequency signal isolation. They also impose a limitation on response times. The source of concern in the present application is that noise generated by the reference diode might feedthrough the capacitances just mentioned. This, plus high frequency disturbances coupled through the reference diode, might degrade the operation of the precision voltage reference circuit.

Current flowing through a reference diode produces noise. The internal resistance associated with the device accounts for a small part of this noise. The Zener breakdown phenomenon is responsible for the larger part of the Zener noise, called microplasma noise.<sup>12</sup> The microplasma noise is usually considered "white noise". A small shunting capacitor can be used to eliminate the higher-frequency components of Zener noise. This is the function performed by the capacitor, C3, in Figure 3.1. An additional function of C3 is to reduce coupling of high frequency power supply signals back into the loop. The lower frequency noise must be tolerated. A capacitor large enough to eliminate the lower frequency components of the noise would probably degrade the regulation

properties of the reference diode. In addition, a capacitor larger than  $0.1\ \mu\text{F}$  would be more difficult to realize if the system were to be micro-circuited.

The precision voltage reference, discussed in the preceding few pages, provides a reference input to the noninverting input of a comparator operational amplifier. This device and its associated circuitry will be discussed next.

#### B. The Comparator Operational Amplifier

Normally, the objective in selecting the amplifier IC1 in Figure 3.1, would be to choose the least expensive device which would meet the physical, electrical, and environmental requirements imposed by the application. This would suggest a "general purpose" amplifier. However, accuracy and stability constraints for the case at hand require the lowest offset and drift parameters possible. Also, a very high common-mode rejection ratio is needed. A large open-loop gain is demanded to provide a sufficiently high loop transmission, which in turn will give the required degree of accuracy. Accuracy, along with offset and drift parameter requirements overshadow gain-bandwidth considerations in selecting the amplifier. However, an amplifier which will assure an adequate value of loop gain at the maximum frequency of interest is necessary for the desired accuracy. It is necessary that the input of the amplifier be protected. This is due to the fact that the current sampled by the sampling resistors is switching from  $R_{P1}$  to  $R_{P2}$  (see Figure 3.1), or vice-versa, in approximately 350 nanoseconds. For 30mA and 60mA levels,

$R_{P1}$  and  $R_{P2}$  are 207 ohms and 103 ohms respectively. Obviously, rather large signals will occur at the input of the operational amplifier during the transient period of switching the sampling resistors. To limit over- and under-shoot in the pulse response and to maintain close regulation, it is essential that the amplifier have as large a slew-rate capability as possible.

The above mentioned criteria, along with items of lesser interest, were studied closely. After detailed studies and testing, it was found that the Analog Devices AD504M offered the best overall performance.

The problem of an insufficient slew-rate for the operational amplifier, IC1, plagued the performance of the circuit illustrated in Figure 3.1, for quite some time. A high loop gain at low frequencies, for steady-state accuracy, requires a large value of capacitance for  $C9$  as compensation against oscillations. This results in more capacitance which must be charged by the op. amp. on each signal swing. The source of charging current is finite. This limitation leads to a specification of the output slew-rate, usually given in  $V/\mu s$ . The slewing rate is defined<sup>18</sup> as the maximum rate of change of output voltage when supplying the rated output.

A finite slew-rate imposes a limitation on the maximum amplitude of a sinewave the operational amplifier can deliver at its output. If  $S$  is the slew rate of the op. amp. and  $V_o$  (max.) is the maximum voltage output at a frequency  $f$ , then<sup>19</sup>

$$V_o \text{ (max.)} = \frac{S}{2\pi f} \quad . \quad (3.5)$$

The problem of an insufficient slew rate for IC1 was partially alleviated by the use of a feedforward technique ( $R_x$  and  $C_x$  in Figure 3.1). Feedforward techniques are discussed in the literature, among which are those listed as References 20, 21, 22, and 23. As often as not, the discussions on feed-forward techniques found in the literature refer to a particular device. The feedforward circuit that offers optimum performance for a given operational amplifier must usually be found experimentally. Such was the case with the circuit in Figure 3.1.

By means of  $R_x$  and  $C_x$  in Figure 3.1, higher frequency signals are fed around the slower lateral PNP transistors following the input section of the operational amplifier. This makes it possible to more heavily compensate for stability with C9 and the RC lag network ( $R_c$  and  $C_c$ ), and yet obtain a reasonable slew rate with IC1. The transient response was acceptable for a 2 to 1 scale factor change, but additional work is needed to provide better slewing rate, overload recovery, and settling time for a 5 to 1 scale factor change.

If the AD504M operational amplifier is to exhibit its superior drift performance, the manufacturer recommends that the device be nulled.  $R_a$  and  $R_b$  in Figure 3.1, are typical values found from investigating three AD504M units.

### C. The Error Amplifier - Level Shift Network

Q1 (A and B) in Figure 3.1, is a differential pair following the input IC1 comparator and functions in a dual role as an error amplifier and level shifter. Q2A serves as a constant current source to supply Q1.

D2 and D3 (1N5230B with  $V_Z = 4.7V$ ) serve to clamp the signal excursions at the base of Q1A and prevent saturation of either Q1A or Q2A; the diodes are normally not conducting. Resistors R7 and R8 in the emitters of Q1A and Q1B increase thermal stability and decrease the gain of this stage. The RC lag network ( $R_c$  and  $C_c$ ) across the collectors of Q1A and Q1B helps shape the frequency response of the TCG.

The error amplifier is operated in the non-inverting mode to reduce any Miller effect at the base of Q1A and hence improve the frequency response. While duals (2N5794) were used for Q1 and Q2, a quad NPN such as the MHQ2222, or individual 2N2222 transistors would serve as well.

#### D. The Power Transistor Stage

A Darlington configuration is used for the output stage of the current regulator section of the TCG. One half of a 2N5794 drives the medium power transistor, Q3. An SDT6103 may be used for Q3, but tends to operate at an elevated temperature. An MPS-U06 is a better choice, and operates much cooler when properly heat-sinked. The Darlington configuration used here does not load the collector circuit of Q1B, and has a current drive capability that far exceeds the required 60mA.

#### E. The H-Switch

The H-switch is a modification of the H-switch in the Hamilton Standard system outlined in the Lawrence Report.<sup>1</sup> The H-switch is a bridge arrangement consisting of four composite MOSFET-bipolar transistor switches. (This type of switch was discussed briefly in Chapter II and illustrated in Figure 2.7.) All the MOSFETs in the H-switch of the U.T.

system are P-channel, whereas in the Hamilton Standard version two P-channel and two N-channel MOSFETs were used. Since dual N-channel MOSFETs are at present unavailable commercially, matching was more easily accomplished with P-channel devices. A dual P-channel MOSFET with separate source and drain leads is necessary in the lower switches of the H-switch, i.e., for Q7A and Q7B in Figure 3.1. The type 3N190 P-channel MOSFET was used for both Q4 and Q5 in the H-switch. It has a maximum  $r_{DS(on)}$  of  $300\ \Omega$ , 10% matching of  $y_{fs}$ , and is readily available from several manufacturers. Also, it has a minimum  $BV_{DSS}$  of 40V, which is difficult to obtain in many of the other available dual MOSFETs.

Each composite switch in the H-switch contains a bipolar transistor as well as a MOSFET. Type SDT6103 bipolar transistors were chosen to fill this role. This device has a  $BV_{CEO}$  of 50V, a maximum collector current rating of 5 amperes, and total power dissipation (with a TO-5 case) of 7 watts. It has a maximum turn-on and turn-off time of 50 nanoseconds, and  $f_T$  of approximately 450 MHz in the region of interest, and a beta curve which is almost flat in the region of interest.

The H-switch, composed of the four composite MOSFET-bipolar switches discussed above, has excellent electrical isolation from the H-switch driver circuit. This was discussed in the U.T. Annual Report<sup>3</sup> of 1972. The composite MOSFET-bipolar switches have excellent thermal stability, as pointed out in the Masters Thesis given as Reference 4. More will be said about the thermal stability of the H-switch in a later chapter.



#### F. The H-Switch Driver

This circuit has the function of translating a state in the logic section into a torque current polarity. When instructed by the logic, it sets up the H-switch to route the torquer current in the necessary direction through the torquer to null the error signal.

The H-switch driver is designed to relegate any limitations in switching speed to the H-switch itself. Since the H-switch driver is essentially driving a capacitive load, considerable effort was necessary to acquire switching times for the 0-35V excursions. Best results were obtained using bipolar transistors with active pull-ups and active pull-downs in the output stage of the driver circuit. In Figure 3.1, Q15A and Q15B are the output stages; Q13A and Q14A function as active pull-downs, rapidly sweeping base charge out of the output stage which is turning off; Q13B and Q14B serve as active pull-ups to rapidly charge the output capacitance of the output stage turning off. The RC networks connecting the SN7400 IC to Q13 and Q14 are commutating networks. The SN7400 serves as the input section of the H-switch driver circuit.

The H-switch driver circuit also serves as an interfacing circuit for TTL to MOSFET levels. If CMOS logic is used in the logic section of the pulse rebalance electronics, then a modified version of the H-switch driver should be substituted. A modified version has been designed and experimentally checked. This alternate H-switch driver circuit will be discussed in a later chapter on the versatility of the torque current generator.

### G. The Sampling Resistors and Sampling Resistor Switching Network

Two sampling resistors are required in this design since the precision voltage reference (PVR) is held constant. With the PVR chosen at 6.2 V, values of  $R_{P1}$  and  $R_{P2}$  can then be chosen to give desired current levels and scale factor ratio. For current levels of 30mA and 150mA, or a scale factor ratio of 5 to 1,  $R_{P1}$  and  $R_{P2}$  are required to be approximately 206.7  $\Omega$  and 41.3  $\Omega$ , respectively. The TCG has been operated with 30 and 150mA levels, and also with 30 and 60mA levels. The 60mA high requires  $R_{P2}$  to be approximately 103.3  $\Omega$ . The wattage of the sampling resistors should be 3 W minimum. Naturally, the sampling resistors need to be as stable as economics and availability allow, and if wirewound, should be as noninductive as possible.

The sampling resistor switching network consists of a quad MOS analog switch (MM552D, a four MOS transistor package), two type SDT6103 bipolar transistors, and resistors R17 and R18. Transistors Q10 and Q11 are paired with Q12D and Q12A respectively to form two composite MOSFET-bipolar switches. Q12B and Q12C serve as buffer switches between the sampling resistors and the comparator amplifier.

The quad MOSFET analog switch is biased at approximately 10V to ensure that the inherent diodes, formed from source and drain to the substrate, are never forward biased. This is also required because the voltage at the base of the H-switch (emitters of Q8 and Q9) may be as high as 8 volts. The 10V bulk bias is obtained from the 15V supply by means of R5 and D5. This eliminates the need of a separate 10V supply. Biasing the quad MOS analog switch at 10V requires a gating voltage of approximately zero to 10V. If the switch is driven by CMOS logic, this

is no problem. However, if the switch is driven by TTL logic, then interfacing is necessary. A circuit which will perform this interfacing function satisfactorily is given in Figure 3.2 and is discussed next.

#### H. The TTL to CMOS Interfacing Network

The TTL to CMOS interface circuit mentioned immediately above (and shown in Figure 3.2) is identical to the H-switch driver circuit, except for having a 10V supply instead of a 35V supply. The 10V supply is obtained from the 15V supply by means of Q23 and associated resistors. This circuit is given in Figure 3.2, along with the TTL to CMOS interface circuit. The interfacing circuit is unnecessary if CMOS logic is used.

#### I. Torquer Compensation

The torquer compensation network depends upon which gyroscope is being used. The goal of the compensation is to make the torquer coil look purely resistive. For the Kearfott Model 2544 gyro, experimental measurements indicate a torquer inductance of 3.08 mH, a torquer resistance of 71.7  $\Omega$ , and a stray capacitance of 20.4 pF. The compensation necessary to make the torquer coil appear resistive is developed in Appendix B. From Appendix B, the values of  $R_{tc}$  and  $C_{tc}$  in Figure 3.1, needed to compensate the Kearfott Model 2544 gyro are 71.7  $\Omega$  and 0.60  $\mu$ F, respectively. The stray capacitance was not compensated.

The compensation values given immediately above are for a particular frequency of a sinusoidal excitation. This particular frequency is 2.4 kHz, which is the limit cycle frequency of the duty cycle generator. The compensation of the torquer coil is reasonably sufficient for

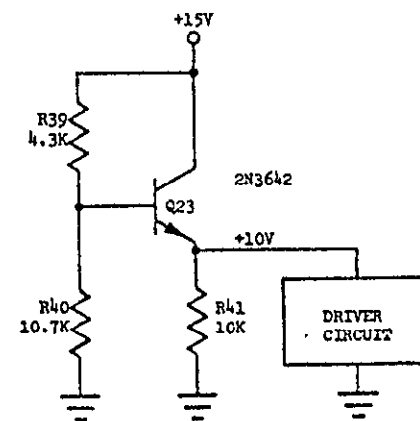
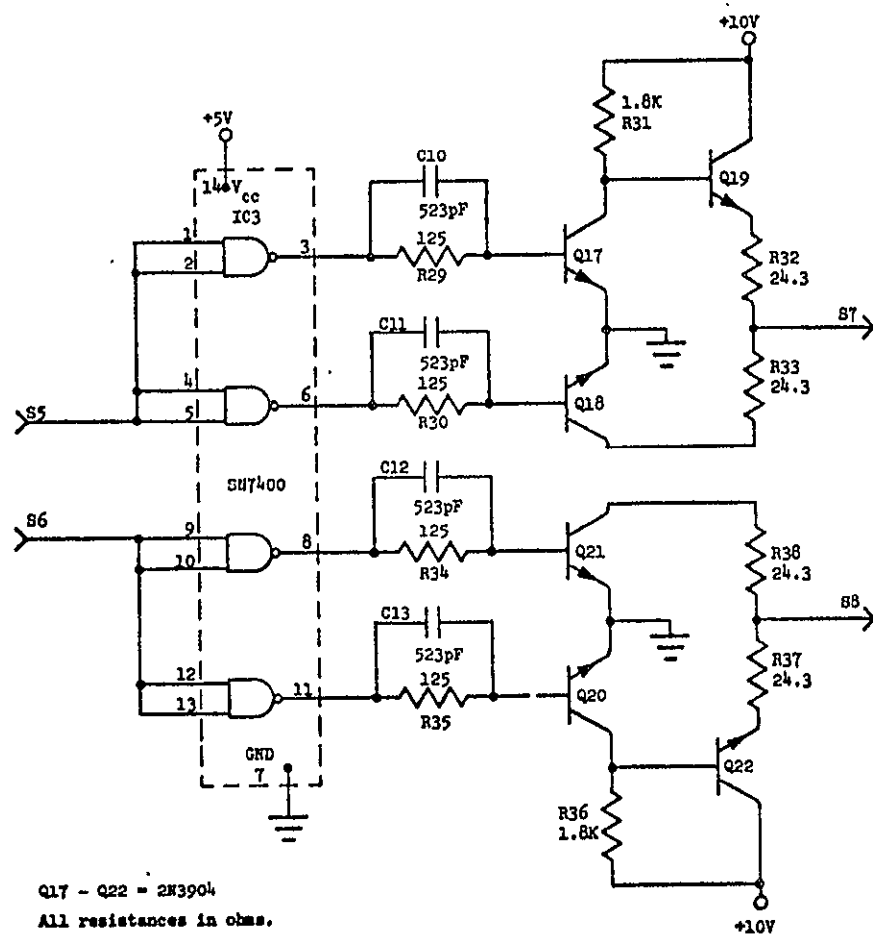


FIGURE 3.2  
TTL TO CMOS INTERFACE

switching polarities of the torquer current at the limit cycle rate. Switching from one torquer current level to another occurs at a different frequency, however, and the torquer coil is not optimally compensated for this phenomenon. Also, the excitation current of the torquer coil is more nearly a square wave than a sinusoidal one. The direction of the current through the torquer coil is switched at the 2.4kHz rate continuously, whereas switching current levels occurs far less frequently. Since optimum compensation for both of these switching schemes is either impossible or difficult to achieve, less error is involved by compensating for the polarity switching rate of 2.4kHz.

The basic design, implementation, and function of each of the major divisions of the TCG has been discussed. Attention will now be turned to evaluating the performance characteristics of the TCG. Stability against self-oscillation is of prime importance in such an evaluation, and will be investigated in Chapter IV.

## CHAPTER IV

### LOOP TRANSMISSION AND STABILITY AGAINST SELF-OSCILLATION

The TCG is a useless piece of circuitry if it is not stable against self-oscillation. Needless to say, an unstable system may eventually destroy itself and its surroundings.

Schwarz and Friedland<sup>24</sup> define a system as being stable if and only if any bounded input results in a bounded output. According to Goldman<sup>25</sup>, a system is stable if a small impressed disturbance, which itself dies out, results in a response which dies out. These definitions of system stability give a reasonably clear concept of the stability of a system against self-oscillation. Some criterion or criteria for stability must be chosen to determine absolute stability and/or relative stability.

Many texts on control theory and feedback systems are available which treat the concept of system stability extensively. Absolute stability of a system can be determined by applying the Routh-Hurwitz criterion to the characteristic equation of the closed-loop system. Reference 26 has a good discussion on this technique. The Routh-Hurwitz criterion does not yield any information on the degree of stability of a feedback system. If unstable roots are present, no indication is given as to the location of these roots in the right-half  $s$  plane. On the other hand, if the characteristic equation has stable roots, the Routh-Hurwitz criterion does not specify where the root locations are with respect to the  $s = j\omega$  axis.

Two basic methods are available for predicting and adjusting a system's performance without resorting to the actual solving of the system's differential equation. One of these is the Nyquist stability criterion, and the other is the root-locus method. The Nyquist stability criterion is a graphical method, and may be used with the gain-phase plot, the polar plot, and the Bode plot for minimum phase open-loop functions. This method involves the analysis and interpretation of the steady-state sinusoidal response of the system's transfer function to reach an understanding of the system's response.

The root locus is a plot of the roots of the characteristic equation of the closed loop system as a function of the gain.<sup>27</sup> The root-locus method is a graphical approach, and is based upon the fact that closed loop poles are related to the zeros and poles of the open-loop transfer function and the gain. It provides a correlation between the feedback system's open-loop poles and zeros and the system's stability characteristics, its frequency and transient response, and its steady-state behavior.<sup>28</sup>

Because of the particulars of the situation and the author's personal preference, the Nyquist stability criterion applied to the Bode plot will be used to attack the problem of the stability of the TCG. This will require a determination of the loop transmission of the TCG for both the low- and high-current modes. This task is complicated by two factors which are both concerned with the open-loop frequency response of the AD504M operational amplifier. The first factor is that no phase information is normally provided for the device on the manufacturer's data

sheets. The second factor is the presence of the feedforward circuit used to increase the slew rate of the operational amplifier. This network was experimentally determined. Since the feedforward network connects the input of the operational amplifier with a point internal to the device, an equivalent circuit of the chip is desirable. Though requested by the author, the manufacturer did not make available detailed and comprehensive information on phase plots and an equivalent circuit. Therefore, it was necessary to experimentally obtain information on the open-loop frequency response of the operational amplifier to supplement the scant data provided by the manufacturer. Otherwise, a relative stability analysis is beyond reach.

Since the loop transmission of the TCG is necessary and central to the development of the concept of relative stability of the circuit, it will be determined first. Later in the chapter, suitable criteria for measuring the relative stability of the circuit will be introduced. Finally, an analysis of the relative stability of the TCG will be made.

#### A. Loop Transmission of the Torque Current Generator

The loop transmission,  $T$ , may be calculated as follows:<sup>29</sup> A voltage disturbance is assumed at the inverting input to the comparator operational amplifier (see Figure 3.1); the signal is traced around the loop; the ratio of the signal returned to the signal injected is the desired loop transmission. This technique readily gives the midband value of  $T$ . The frequency dependence of  $T$  must then be calculated.

Before proceeding with the calculation of  $T$ , the open-loop frequency response of the AD504M operational amplifier must be determined.



The manufacturer's data sheet gives the open-loop magnitude response as a function of frequency for a maximum  $C_c$  ( $C_c$  is the compensation capacitor, equivalent to C9 in Figure 3.1), of 390pF. As indicated in Figure 3.1, the experimentally determined value of C9 is 3380pF. This value was reached by doubling the loop transmission and determining the value of C9 necessary to stabilize the loop. The loop gain was then changed back to its normal value for operation of the circuit. Thus, no manufacturer produced curves are available for the open-loop magnitude response for compensation of  $C_c = 3380\text{pF}$ . Also, only scant phase versus frequency information was provided by the manufacturer upon special request. It too only encompassed compensation up to  $C_c = 390\text{pF}$ .

The difficulty just described forced the author to turn to an experimental method of obtaining the open-loop frequency response of the operational amplifier. The typical open-loop gain of 8,000,000 all but precludes any open-loop method of measurement. Nevertheless, the circuit illustrated in Figure 4.1 (a) was tested. Nulling was difficult at any point, and became impossible as the signal frequency exceeded 5 kHz. Data was obtained at frequencies of 200 Hz, 500 Hz, and 2 kHz for later comparison with data obtained by other test set-ups.

To circumvent the high gain and offset problems, the AD504M op. amp. was tested in three closed-loop configurations. Two of these are illustrated in Figure 4.1, (b) and (c). The method of attack was as follows: obtain closed-loop gain and phase versus frequency data from the closed-loop configurations; plot this data on the curvilinear coordinates of a Nichols chart with frequency as a parameter; obtain and plot

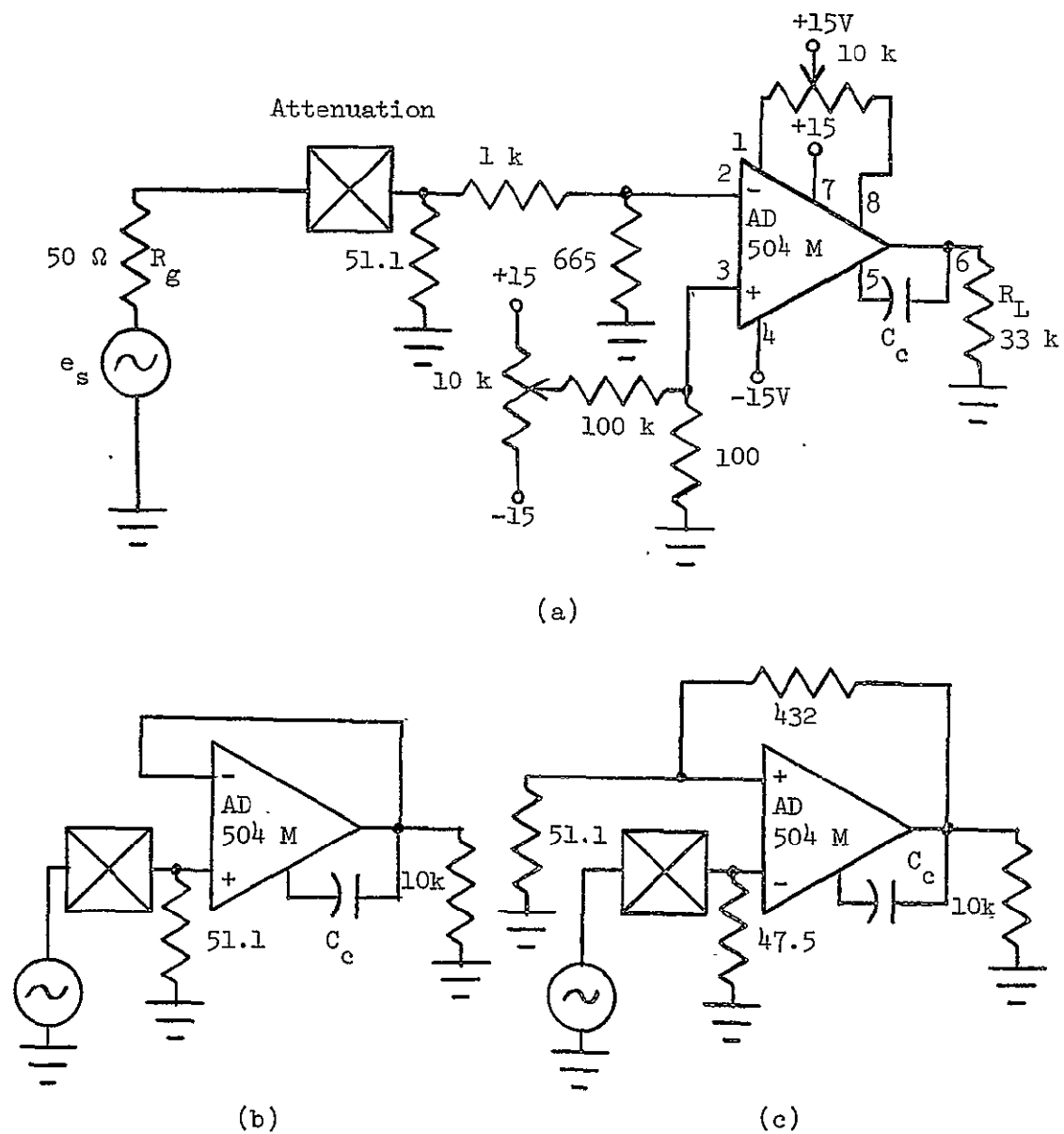


FIGURE 4.1

TEST CONFIGURATIONS FOR OBTAINING THE OPEN-LOOP  
FREQUENCY RESPONSE OF THE AD504M OPERATIONAL AMPLIFIER

values of  $T$  from the linear coordinates of the Nichols chart for specific values of frequency; and graphically subtract the feedback factor from the Bode plot of  $T$  (if the feedback factor is other than unity) to obtain the open-loop frequency response of the operational amplifier. Particular care must be taken to plot only  $T/(1+T)$  on the curvilinear coordinates of the Nichols chart. The Nichols chart assumes a unity feedback system.

Close agreement was found in the test results of the three configurations of Figure 4.1. Also, the magnitude curve is approximately what one would expect by extrapolating the manufacturer's data sheet curve for  $C_c = 390\text{pF}$  to one for  $C_c = 3380\text{pF}$ . The experimentally determined open-loop frequency response of the AD504M op. amp. for a compensation of  $C_c = 3380\text{pF}$  is given in Figure 4.2. The voltage gain of the op. amp. is designated  $A_1$ . Thus far the feedforward circuit has been ignored in the tests to determine the open-loop frequency response of the device.

The lack of an equivalent circuit of the AD504M op. amp. with typical parameter values precludes any direct calculation of the effect of the feedforward circuit on the op. amp. response. In reality, such a calculation would be a sizable task even if an equivalent circuit of the AD504M were available. The feedforward circuit was experimentally determined and was used to partially alleviate the slew-rate problem . . . a nonlinear phenomenon. When the TCG switches sampling resistor values, a differential signal on the order of 3.8 volts develops at the input of the operational amplifier. The feedforward network routes this signal to an

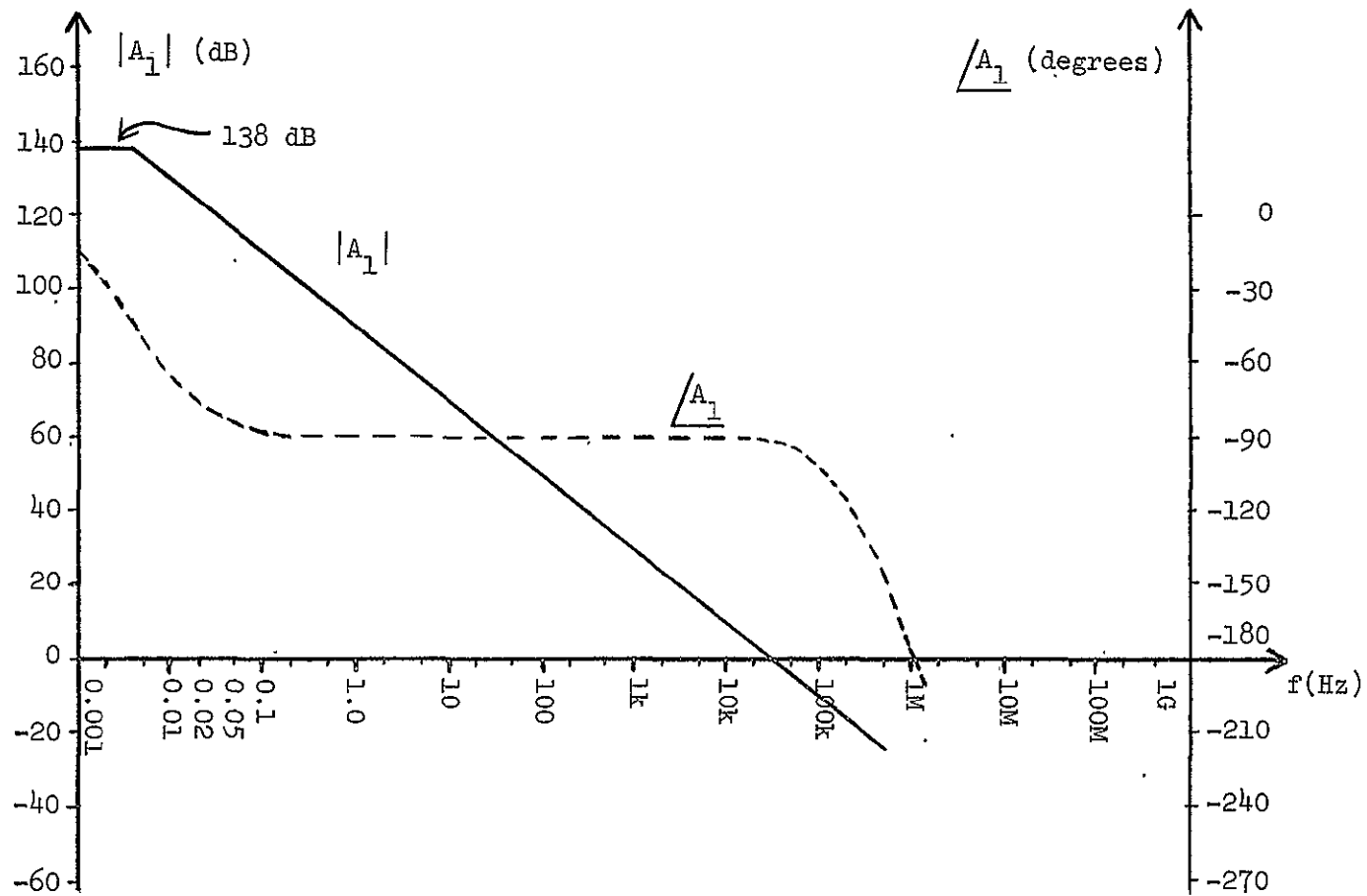


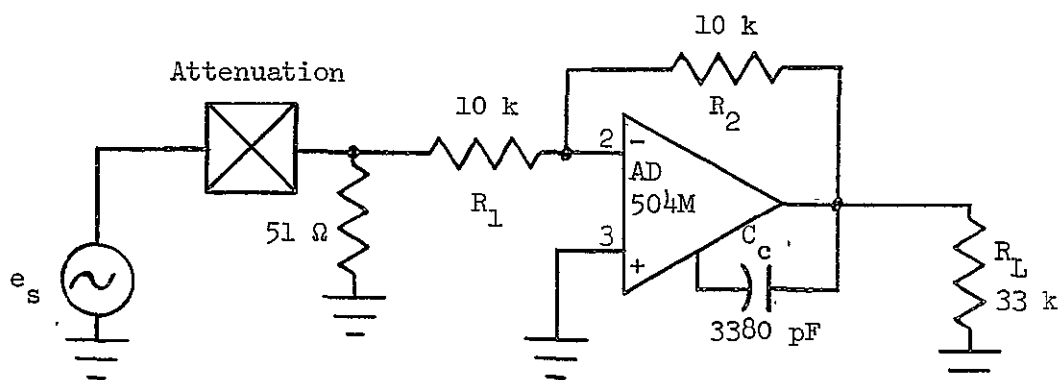
FIGURE 4.2  
 OPEN-LOOP FREQUENCY RESPONSE OF THE AD504M  
 OPERATIONAL AMPLIFIER WITH  $C_c = 3380$  pF

internal point of the op. amp. past the input circuit. A signal of this magnitude causes transistor stages internal to the op. amp. to either cutoff or saturate during the early part of the switching transient. The net effect of the feedforward network is a nonlinear one. Thus, the effect should not show up on a Bode plot of the open-loop frequency response of the op. amp. plus feedforward network. Further experimental work was performed to substantiate this argument.

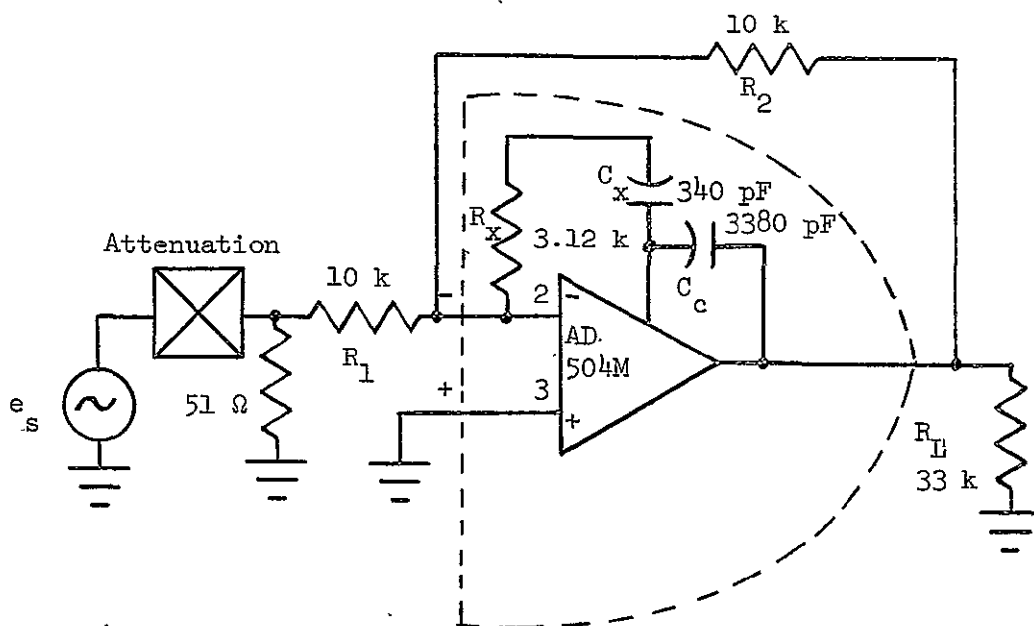
The AD504M op. amp. was tested in the configurations illustrated in Figure 4.3 over a frequency range from 100 Hz to 600 kHz. The resistors  $R_1$  and  $R_2$  were chosen such that  $R_1 = R_2 = 10K$  in order to give a voltage feedback factor of unity. The theory for identifying the voltage feedback factor for the inverting closed-loop configuration of the op. amp. is developed in Appendix C. Also, the procedure for obtaining open-loop information from closed-loop data for this configuration via the Nichols chart is outlined in Appendix C.

Open-loop voltage gain and phase versus frequency plots of the AD504M op. amp. were obtained (as outlined in Appendix C) for the configurations illustrated in Figure 4.3. The plot obtained with the feedforward network present was identical to the one obtained with the feedforward network absent. Further, each of these plots closely approximated the open-loop frequency response previously obtained and given in Figure 4.2.

In view of the close agreement of the results described thus far in this chapter, the plot in Figure 4.2 will be accepted as a reasonable representation of the open-loop frequency response of the AD504M op. amp.



(a) Closed-loop configuration, inverting mode, without feed-forward network.



(b) Closed-loop configuration, inverting mode, with feedforward network.

FIGURE 4.3

CLOSED-LOOP CONFIGURATIONS OF THE AD504M OP. AMP. USED  
TO STUDY EFFECTS OF THE FEEDFORWARD NETWORK

Actual measurements were made over a frequency range of 100 Hz to 600kHz. The typical open-loop voltage gain of 8,000,000 quoted in the manufacturer's data sheet was chosen as the low-frequency point to which the magnitude curve was to extend. Now that a suitable representation of the dynamic performance of the AD504M op. amp. is in hand, the calculation of the loop transmission can proceed.

The next step in the calculation of the loop transmission of the TCG is to obtain the frequency response of the circuit from the output of the op. amp. to the input of the op. amp. This can be conveniently done by means of a canned computer program called PCAP.<sup>30</sup> The results for both the low- and high-torque cases are given in Figure 4.4. The voltage gain from the output of the op. amp. to the input of the op. amp. is designated  $A_2$ . The "LT" subscript in Figure 4.4 refers to the low-torque case where the torquer current is 30mA. The "HT" subscript refers to the high torque case in which the torquer current is 60mA.

The final step in obtaining the loop transmission of the TCG is to graphically combine the plots in Figure 4.2 and Figure 4.4. The resulting Bode plot of  $T$  is given in Figure 4.5. Note that in the region of interest, i.e., from D.C. to 1MHz, the gain plots for the high- and low-torque cases track. They are merely separated by 2.1 dB. The phase plots for the low- and high-torque cases are so nearly equal as to be approximated by the same curve.

The Bode plot of the loop transmission of the TCG (given in Figure 4.5) is of central importance in the analysis of the stability of the circuit against self-oscillation. Also, reference will be made to Figure

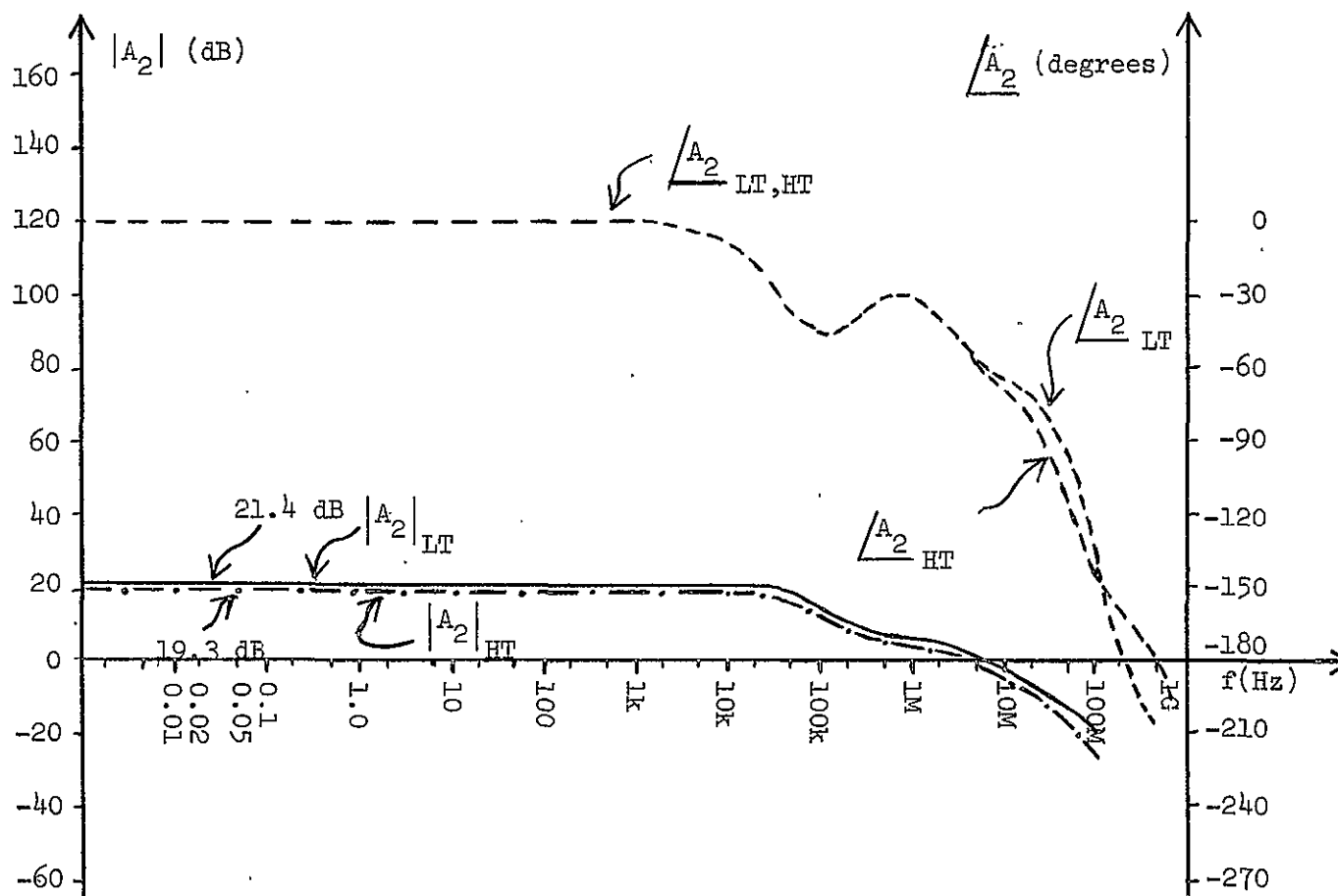


FIGURE 4.4

PCAP-RESULTS FOR VOLTAGE GAIN AND PHASE VERSUS FREQUENCY  
FOR TORQUE CURRENT GENERATOR FROM OUTPUT OF OP. AMP. TO  
INPUT OF OP. AMP.



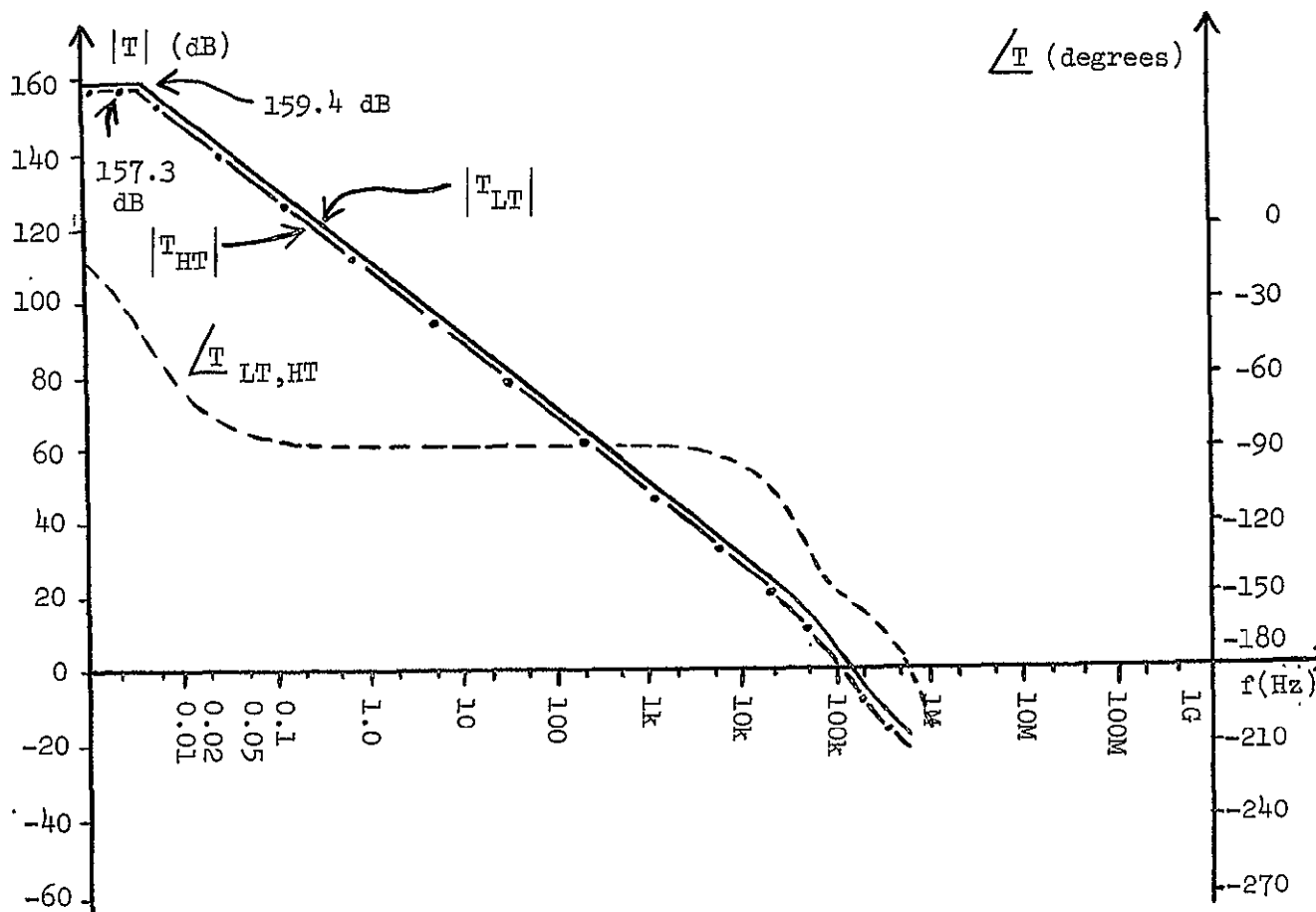


FIGURE 4.5

BODE PLOT OF THE LOOP TRANSMISSION OF  
THE TORQUE-CURRENT GENERATOR

4.5 when the actuating errors are investigated in a later chapter.

Numerous other topics to be discussed later in the thesis will warrant further use of this valuable plot.

Relative stability of the TCG against self-oscillation will be meaningful only if suitable and widely-accepted criteria are chosen as figures of merit. Such criteria will be discussed briefly. Then the relative stability of the TCG will be expressed in terms of these figures of merit.

#### B. Criteria for Evaluating the Relative Stability of the Torque Current Generator

Gain and phase margins are criteria which are widely used and acknowledged as means of defining the relative stability of a feedback system. These parameters may be obtained from a Bode plot of the loop transmission of the feedback system.

The gain margin (GM) is defined as the value of  $|T|$  in decibels at the frequency at which the phase angle of  $T$  is 180 degrees.<sup>31</sup> (For a negative feedback amplifier circuit, the sign of  $T$  is negative at midband frequencies. This implies that the phase angle of  $T$  at midband frequencies is 180 degrees. The 180 degrees of phase angle mentioned in the definition of gain margin refers to additional phase shift at frequencies above midband).

The phase margin (PM) is 180 degrees minus the magnitude of the angle of  $T$  at the frequency for which  $|T|$  is unity (zero decibels).<sup>31</sup> In terms of a Nyquist diagram, the phase margin is the amount of phase shift needed at unity gain to make the Nyquist plot pass through  $-1 + j0$  point.

The phase margin can be used to obtain an estimate of the system damping ratio  $\xi$ .<sup>32</sup>  $\xi$  is a parameter used in the characterization of a second-order system.  $\xi$  is defined in most systems texts, such as References 24, 26, 27, 28, and 32. The parameter is a measure of how rapidly the natural oscillations of a second-order system are "damped out" as the losses in the system increase. The possibility of arriving at the damping ratio via the phase margin is based on a second-order system for which an exact relationship between phase margin and damping ratio exists. Thus, even though a system under investigation is not of second order, it may be approximated as a second-order system in many cases. Then the relationship between its phase margin and damping ratio may be assumed the same as that of a second-order system.

Correlations between the frequency response and the time response can be made explicit only in the case of second-order systems. Only the general trends hold true for higher order systems. However, some rules of thumb for PM and GM are widely observed in control system design for any order system. The rules of thumb

$$PM > 30^\circ$$

$$GM > 6 \text{ dB}$$

generally result in an acceptable transient response and an adequate "cushion" of stability margin for differences between model and actual system.<sup>28</sup>

The phase margin is meaningful in some systems where the gain margin is not. Consequently, the phase margin is usually more descriptive

of relative stability than the gain margin. Both are needed for the best understanding of relative stability.

There are many systems higher than second order for which phase margin and gain margin have significance and are meaningful specifications. However, one should be cognizant of the fact that it is possible for some complex systems that the GM and PM will not give a reasonable indication of system performance.

### C. Relative Stability of the Torque Current Generator

The gain and phase margins of the TCG may be obtained from the Bode plot of  $T$  found in Figure 4.5. The loop transmission plotted in that figure is for torquing current levels of 30mA and 60mA. For current levels below 30mA and above 60mA, new loop transmission plots must be generated to investigate the relative stability of the TCG at those particular levels. Other current levels will be investigated in a later chapter on the versatility of the TCG.

The gain and phase margins of the TCG, taken from Figure 4.5, are tabulated in Table 4.1.

The gain margins listed in Table 4.1 are well above a 6 dB minimum for good response. The phase margins do not exceed the 30 degrees mentioned earlier as a desirable minimum. However, herein lies the engineering trade-off. The choice is one of more relative stability and slower response (rise and fall times of the torquer current), or a faster response and less relative stability. The speed of response has a great deal to do with how quickly the torquing scales can be switched. This in

TABLE 4.1  
GAIN AND PHASE MARGINS OF THE  
TORQUE CURRENT GENERATOR

	GAIN MARGIN	PHASE MARGIN
Low-Torque Case (30mA torquing current)	18dB	27°
High-Torque Case (60mA torquing current)	21dB	30°

turn determines how many data pulses are lost in the transition from one torquing scale to another. With these and other factors considered, the compensation networks were chosen to give the margins tabulated in Table 4.1.

The results of this chapter will be used in later chapters which will continue to more fully characterize the TCG. Steady-state accuracy will be discussed in the next chapter, along with the closed-loop frequency response of the TCG. An expression for  $T$  as a function of frequency will be obtained during that discussion.

## CHAPTER V

### CLOSED LOOP FREQUENCY RESPONSE

#### AND STEADY-STATE ACCURACY

##### A. Closed-Loop Frequency Response of the Torque Current Generator

The convolution integral may be used to establish a relationship between the system transfer function and the time domain response of a system to an arbitrarily specified input.<sup>32</sup> A relationship also exists between the transfer function of a system and the frequency response of the system. Consequently, if the frequency response of a system is known, the time domain response of the system to an arbitrarily specified input should be known also. However, a direct translation from the frequency domain to the time domain is mathematically cumbersome for higher order systems. As a result, the correlation between the closed-loop frequency response and the transient response of a system is often based on the second-order system. Many systems higher than second-order may be assumed to be dominated by a pair of complex poles in the vicinity of the imaginary axis. The system's behavior is then similar to a pure second-order system, and reasonable response parameters may be obtained from the approximation.

The closed-loop frequency response of a unity feedback system is a plot of

$$C/R(j\omega) = \frac{G(j\omega)}{1 + G(j\omega)} \quad (5.1)$$

as  $\omega$  varies from 0 to  $\infty$ . In equation (5.1),  $C/R(j\omega)$  is the control ratio or closed-loop transfer function, and  $G(j\omega)$  is the direct or forward transfer function. Since unity feedback is assumed in Equation (5.1),  $G(j\omega)$  is also the loop transfer function, and is often referred to as the open-loop transfer function, or loop transmission.<sup>33</sup>

For a nonunity feedback system, the closed-loop response is given by

$$C/R(j\omega) = \frac{G(j\omega)}{1 + G(j\omega)H(j\omega)} = \frac{1}{H(j\omega)} \left[ \frac{G(j\omega)H(j\omega)}{1 + G(j\omega)H(j\omega)} \right]. \quad (5.2)$$

$H(j\omega)$  is the feedback transfer function. Calculation of the closed-loop frequency response from a Nyquist diagram is not straightforward. However, the Nichols chart provides a convenient graphical method for obtaining the closed-loop frequency response from the loop transmission. The procedure is outlined in controls type texts, and in many electronics texts or amplifier handbooks, such as Reference 34.

The loop transmission,  $T$ , for the TCG was obtained in Chapter IV. The direct transfer function used in obtaining  $T$  was an open-loop voltage gain,  $A_v$ . Equation (5.2), may be written as

$$\begin{aligned} A_{fv} \equiv \frac{E_o}{E_i}(j\omega) &= \frac{1}{B(j\omega)} \left[ \frac{A_v(j\omega)B(j\omega)}{1 + A_v(j\omega)B(j\omega)} \right], \\ &= \frac{1}{B(j\omega)} \left[ \frac{T(j\omega)}{1 + T(j\omega)} \right]. \end{aligned} \quad (5.3)$$

In Equation (5.3),  $B$  is the feedback factor, and

$$T(j\omega) = A_v(j\omega)B(j\omega) \quad (5.4)$$

is the loop transmission.  $A_{fv}$  is the closed-loop voltage transfer function. One may note from Equation (5.4) that the frequency dependence of  $T$  is two-fold: it depends on  $A_v(j\omega)$ , and on  $B(j\omega)$ . If  $B$  should be frequency independent, then  $T$ , and hence  $A_{fv}$ , have their frequency response dependent upon that of  $A_v(j\omega)$  alone. Before proceeding with the closed-loop frequency response of the TCG, two topics will be discussed. One is the frequency dependence of the feedback network, and the other is a simplified feedback configuration for the TCG.

#### Frequency Dependence of the Feedback Network

As a means of investigating the frequency dependence of what will be considered the feedback network, that portion of the TCG from the output of Q3 (see Figure 3.1) to the input of IC1 was modeled on PCAP. The electrical isolation of the H-switch and sampling resistor switching network provided by the MOSFET's makes the modeling easier. The torquer coil was compensated as indicated in Figure 3.1, and the top of the H-switch was driven by a current source. The impedance looking into the top of the H-switch,  $Z_B$ , was calculated by the PCAP program over a frequency range of 1Hz to 1GHz. The results are plotted in Figure 5.1 for the low-torque case ( $I_{\text{torque}} = 30\text{mA}$ ).

The high-torque case had for all practical purposes the same phase shift characteristics as the low-torque case, and consequently was not



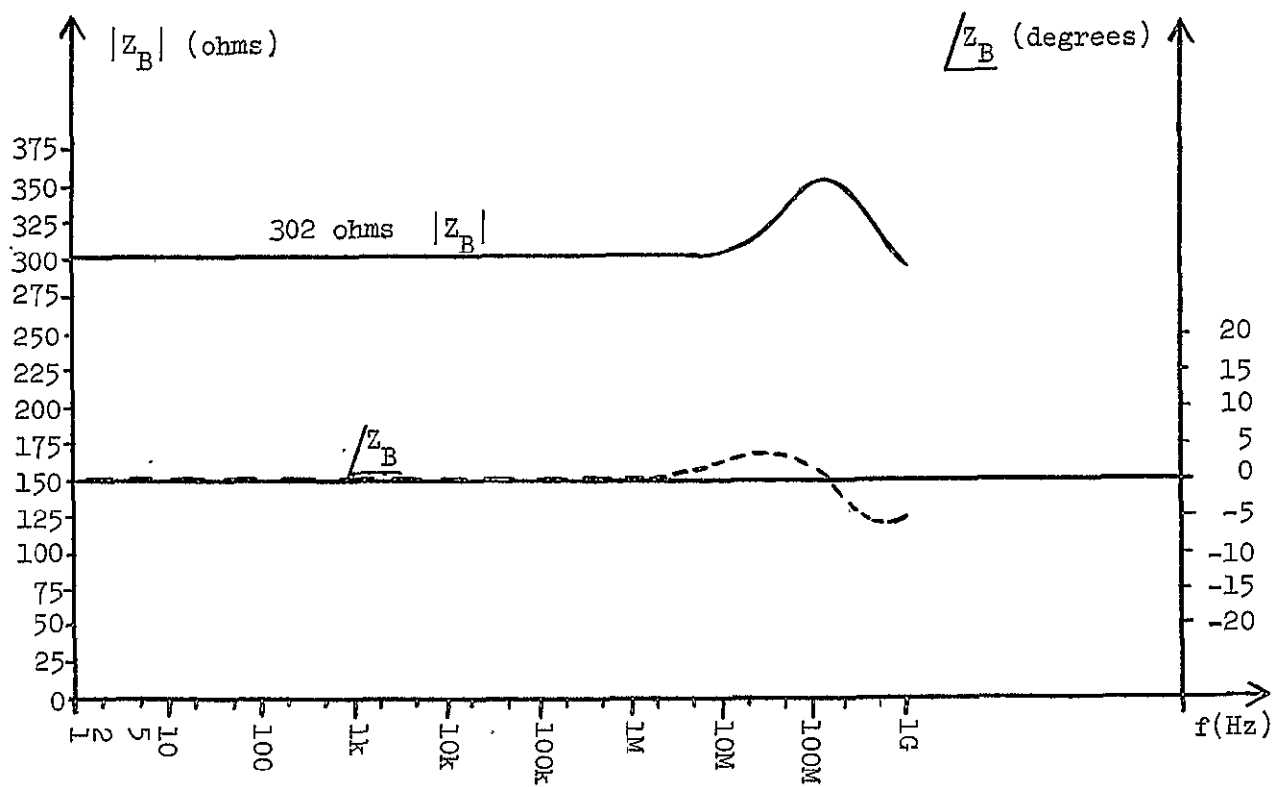


FIGURE 5.1

IMPEDANCE  $Z_B$  SEEN LOOKING INTO THE TOP OF THE  
H-SWITCH FOR THE LOW-TORQUE CASE

plotted. The magnitude of  $Z_B$  for the high torque case was approximately 198  $\Omega$  in contrast to 302  $\Omega$  for the low-torque case. This is due primarily to the difference in the values of the sampling resistors used for the two torquing levels.

Examination of Figure 5.1 indicates that  $Z_B$  maintains a rather constant value out to approximately 10 MHz. Something like a resonant peak occurs at approximately 140 MHz, although the side skirts are not sharp. There is less than 2 degrees phase shift in  $Z_B$  below 10 MHz, and less than 7 degrees on to 1 GHz.

A brief look at Figure 4.5 shows that the region of interest for the operation of the TCG extends from D.C. to less than 1 MHz. Because of this and the discussion above, the impedance seen looking out from the emitter of Q3 in the TCG can be considered purely resistive over the operating range of the TCG. Certainly the feedback network is located between the output and input of the current regulator section of the TCG. Hence, it is included in the impedance just discussed, and will be considered frequency independent over the useful frequency range of the TCG.

#### A Simplified Feedback Configuration for the TCG

As mentioned earlier in this chapter, the direct transfer function used in obtaining T in Chapter IV was an open-loop voltage transfer function. Perhaps the more meaningful simplified feedback configuration to develop would be a voltage-sampled voltage-summed feedback network. Dynamically, the TCG functions as a voltage to current converter, or a voltage-controlled current source. The load is floated, and is actually

contained in the feedback loop. In one sense, the TCG can be represented by Figure 5.2, which is taken from Reference 35.

In Figure 5.2, both the source and the load are connected in the feedback loop. The current drain on the source is only the input bias current of the amplifier. The amplifier here represents the combination of the op. amp. and the error amplifier-level shift network. Feedback attempts to remove the signal swing from the amplifier input. As a result, an input impedance of

$$Z_i' = A Z_i \quad (5.5)$$

is presented to the source by the amplifier.  $A$  is the open-loop gain of the amplifier, and  $Z_i$  is the input impedance of the amplifier ( $Z_i$  is the input impedance of the op. amp. in the TCG).

Feedback reduces the amplifier differential input voltage to almost zero, causing the voltage on the sense resistor  $R_p$  to equal the input signal  $e_i$ . By this means feedback controls the load current. If the amplifier input current is negligible, the associated current  $e_i/R_p$  essentially all flows in the load. Consequently, the output current is easily and accurately controlled by a single sense resistor  $R_p$  to be

$$I_o = \frac{e_i}{R_p} \quad (5.6)$$

Most of the signal error associated with the amplifier is removed by high-gain feedback. Small input voltage changes are produced by load voltage changes. The input voltage changes produce current changes, and thus define the current source output impedance as<sup>35</sup>

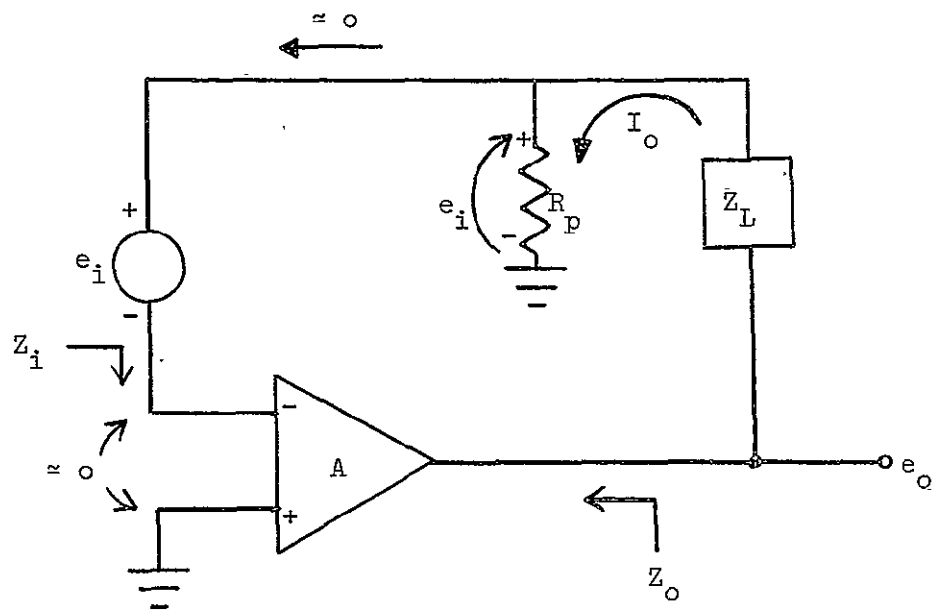


FIGURE 5.2

A CONTROLLED CURRENT SOURCE USED TO DISCUSS  
FEEDBACK MECHANISMS IN THE TCG

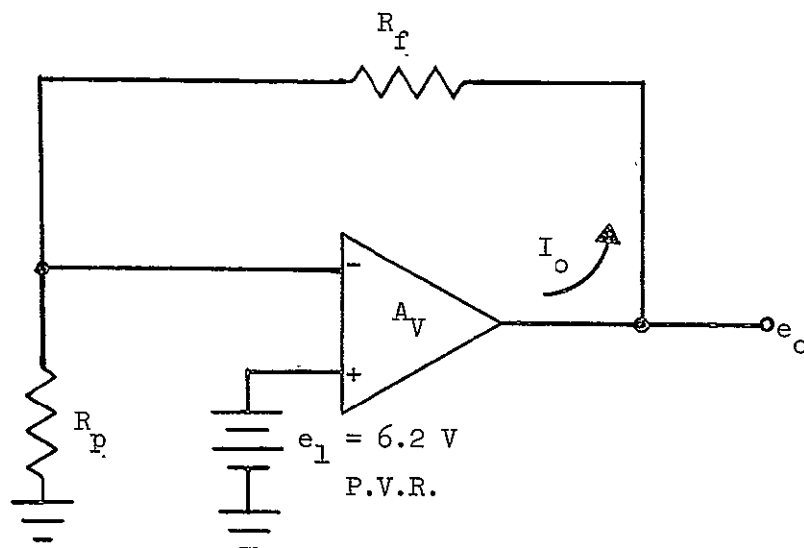
$$Z_o = A R_p . \quad (5.7)$$

Assuming  $A$  very large, the low-frequency closed-loop gain of the controlled current source shown in Figure 5.2 is

$$\frac{e_o}{e_i} = 1 + \frac{Z_L}{R_p} . \quad (5.8)$$

An alternate, but equivalent configuration to that in Figure 5.2 is to drive the noninverting input with a grounded signal. In the case at hand, the input to the noninverting input is a D.C. precision voltage reference. The feedback network, considered purely resistive, consists of the following: (1) the sampling resistor(s); (2) the circuit from the output of Q3 to the sampling resistor. This portion of the circuit was shown earlier to behave as a resistance over the frequency range of interest. The value of this resistance may be obtained by subtracting the value of the sampling resistor from the impedance  $Z_B$ .  $Z_B$  is the impedance seen from the emitter of Q3 (see Figure 3.1) looking into the top of the H-switch, and was discussed earlier in this chapter. The alternate configuration just discussed is illustrated in Figure 5.3.

In the circuit illustrated in Figure 5.3, the amplifier block  $A_v$  represents the combined open-loop voltage gain of the op. amp. and the error amplifier. The frequency dependence of the circuit is relegated to that block.  $R_f$  is used instead of  $Z_f$  because the feedback network is resistive over the operating range of the TCG. Now that a suitable simplified representation of the TCG has been obtained in the form



Note:  $R_p = 206.7 \, \Omega$  for the low-torque case.  
 $R_p = 103.3 \, \Omega$  for the high-torque case.  
 $R_f \approx 95.3 \, \Omega$  for both low- and high-torque cases.

FIGURE 5.3

A SIMPLIFIED FEEDBACK CONFIGURATION REPRESENTING  
 THE TORQUE CURRENT GENERATOR

illustrated in Figure 5.3, the investigation of the closed-loop frequency response will be continued.

#### An Algebraic Expression for the Closed-Loop Voltage Gain of the TCG

With reference to Figure 5.3 the closed-loop voltage gain of the TCG,  $A_{fv}$ , may be written as

$$\begin{aligned} A_{fv} &\equiv \frac{E_o}{E_i}(j\omega) = \frac{A(j\omega)}{1 + A(j\omega)B} , \\ &= \frac{1}{B} \left[ \frac{T(j\omega)}{1 + T(j\omega)} \right] . \end{aligned} \quad (5.9)$$

In Equation (5.9)

$$B = \frac{R_p}{R_p + R_f} , \quad (5.10)$$

and

$$T(j\omega) = A_v(j\omega)B . \quad (5.11)$$

A Bode plot of  $T$  was given in Figure 4.5. A brief examination of the plot indicates that the plot for  $T$  may be closely approximated by a function with the proper midband value and having two poles. The two poles are virtually the same for both the low- and high-torque cases. The two poles occur at approximately 0.004 Hz and 60 kHz.  $T$  may be written in the form

$$T = T_{mid} \left( \frac{1}{1 + j f/f_1} \right) \left( \frac{1}{1 + j f/f_2} \right) , \quad (5.12)$$

where  $T_{\text{mid}}$  is the midband value of  $T$  and  $f_1$  and  $f_2$  are the poles of  $T$ . Further examination of Figure 4.5 indicates that the values of  $T_{\text{mid}}$  for the low- and high-torque cases are

$$\left| T_{\text{mid}}^{\text{L.T.}} \right|_{\text{dB}} \approx 159.4 \text{ dB} , \quad (5.13)$$

and

$$\left| T_{\text{mid}}^{\text{H.T.}} \right|_{\text{dB}} \approx 157.3 \text{ dB} . \quad (5.14)$$

These dB values translate into magnitude values of

$$\left| T_{\text{mid}}^{\text{L.T.}} \right| \approx 9.33 \times 10^7 , \quad (5.15)$$

and

$$\left| T_{\text{mid}}^{\text{H.T.}} \right| \approx 7.33 \times 10^7 . \quad (5.16)$$

Equation (5.15) may be substituted into Equation (5.12) along with the pole frequencies to give a low-torque case expression for  $T$  as

$$T_{\text{L.T.}} \approx (-9.33 \times 10^7) \left[ \frac{1}{1 + j \frac{f}{0.004\text{Hz}}} \right] \left[ \frac{1}{1 + j \frac{f}{60\text{kHz}}} \right] . \quad (5.17)$$

In a similar manner, the high-torque case expression for  $T$  is

$$T_{\text{H.T.}} \approx (-7.33 \times 10^7) \left[ \frac{1}{1 + j \frac{f}{0.004\text{Hz}}} \right] \left[ \frac{1}{1 + j \frac{f}{60\text{kHz}}} \right] . \quad (5.18)$$



Equations (5.17) and (5.18) may be compared with Equations (E.26) and (E.27) in Appendix E to establish greater reliability. The negative sign in the expressions for  $T$  above account for negative feedback, sometimes referred to as inverse feedback.<sup>36</sup> The values of  $T_{mid}$  appear quite large. As stated earlier, these values are derived assuming the typical D.C. voltage gain stated by the manufacturer of the AD504M op. amp., i.e.,  $8 \times 10^6$ . The lower frequency pole was obtained by extrapolating the experimentally obtained frequency response data of the op. amp. back to the typical D.C. gain of  $8 \times 10^6$ . If this gain should be 1,000,000 instead of 8,000,000, then the lower pole would appear to be at 0.03Hz when the same technique is applied. The typical gain of 8,000,000 will be assumed in the calculations to follow.

Equation (5.12) may be substituted into Equation (5.9) to give

$$A_{fv} = \frac{A_{fv(mid)}}{[(jf)^2/f_n^2] + [(jf) 2 \xi/f_n] + 1} \quad (5.19)$$

In Equation (5.19),

$$A_{fv(mid)} = \frac{|T_{mid}|}{1 + |T_{mid}|} \left( \frac{1}{B} \right) \quad (5.20)$$

$\xi$  is the damping ratio, and  $f_n$  is the undamped natural frequency.  $f_n$  is related to the two high-frequency poles and the midband loop gain by<sup>29</sup>

$$f_n = \sqrt{f_1 f_2 (1 + |T_{mid}|)} \quad (5.21)$$

$\xi$  is related to the two high frequency poles and  $f_n$  by

$$\xi = \frac{f_1 + f_2}{2f_n} . \quad (5.22)$$

Many texts on feedback and control systems contain Bode plots of magnitude and phase versus  $f/f_n$  with  $\xi$  as a parameter for the quadratic factor in Equation (5.19). Consequently, the high-frequency response of a feedback system with two important corner frequencies can be determined as follows: (a) calculate or graphically obtain  $T_{mid}$ ,  $f_1$ , and  $f_2$ ; (b) using these values, calculate  $f_n$  and  $\xi$  from Equations (5.21) and (5.22); (c) use a standard Bode plot of the  $[1 + j(2\xi f/f_n) + j(f/f_n)^2]^{-1}$  factor to plot that factor in Equation (5.19); and (d) shift the plot obtained in (c) by an amount  $A_{fv(mid)}$ .

Substitution of Equation (5.15) into Equation (5.20) gives  $A_{fv(mid)}$  for the low-torque case as

$$\left| A_{fv(mid)}^{L.T.} \right| \approx 1.459 . \quad (5.23)$$

In a like manner,  $A_{fv(mid)}$  for the high-torque case is

$$\left| A_{fv(mid)}^{H.T.} \right| \approx 1.920 . \quad (5.24)$$

$f_n$  and  $\xi$  were calculated for the low- and high-torque cases of the TCG. The values of these parameters were:

$$\begin{aligned}
 f_n(\text{L.T.}) &\approx 150 \text{ kHz} \\
 f_n(\text{H.T.}) &\approx 133 \text{ kHz}
 \end{aligned}
 \tag{5.25}$$

and

$$\begin{aligned}
 \xi(\text{L.T.}) &\approx 0.200 \\
 \xi(\text{H.T.}) &\approx 0.226
 \end{aligned}
 \tag{5.26}$$

Since a plot of  $A_{fv}$  versus frequency will be generated from T via a Nichols chart shortly, no attempt will be made to produce one by the method described above. However, to verify that the two-pole approximation for T is reasonable, values obtained for  $M_p$ ,  $f_p$ , and  $f_{hi(f)}$  by the two methods can be compared. If M is the normalized closed-loop gain, i.e.,

$$M = \frac{A_{fv}}{A_{fv(\text{mid})}} \quad , \tag{5.27}$$

then  $M_{pf}$  is the peak value of M.  $f_p$  is the resonant frequency, or the frequency at which M reaches its peak.  $f_{hi(f)}$  is the closed-loop, high corner frequency, and occurs when the closed-loop gain is 3dB below its midband value. This is also the closed-loop bandwidth, BW.

The parameters in Equations (5.25) and (5.26) were used with a Bode plot of the quadratic factor in the expression for  $A_{fv}$  to estimate  $M_{pf}$ ,  $f_p$ , and  $f_{hi(f)}$ . These values are given in Table 5.1 which follows the development of a Bode plot of  $A_{fv}$  from a Bode plot of T via a Nichols chart.

TABLE 5.1

CLOSED-LOOP FREQUENCY RESPONSE PARAMETERS FOR THE  
TORQUE CURRENT GENERATOR

	$ A_{fv}(\text{mid}) (\text{dB})$	Parameters estimated from two-pole function approximation for T and quadratic factor plot			Parameters obtained from Bode plot of T using a Nichols chart (Graphical)		
		$M_{pf}(\text{dB})$	$f_p(\text{Hz})$	BW(Hz)	$M_{pf}(\text{dB})$	$f_p(\text{Hz})$	BW(Hz)
Low-torque case ( $I_t = 30 \text{ mA}$ )	3.28 dB	7.6 dB	125 kHz	210 kHz	7.0 dB	130 kHz	205 kHz
High-torque case ( $I_t = 60 \text{ mA}$ )	5.66 dB	6.8 dB	114 kHz	200 kHz	6.1 dB	108 kHz	200 kHz

### Closed-Loop Frequency Response of the TCG From $T$ Via the Nichols Chart

The Nichols chart can be used as a conversion chart whereby the values of  $|T|$  and  $\angle T$  are converted into the corresponding values of  $|T/(1 + T)|$  and  $\angle T/(1 + T)$ . An outline of the procedure for obtaining the graphical solution of the closed-loop frequency response of a feedback system using a Nichols chart is given in many texts on control theory. References 27 and 28 are examples.

Appendix D contains a Nichols chart with plots of  $|T|$  versus  $\angle T$ , with frequency as a parameter, for the low- and high-torque cases. All the pertinent data involved in the operation is tabulated in Table D.1. Table D.1 is also located in Appendix D. From the data in Table D.1, a Bode plot of  $|T/(1 + T)|$  and  $\angle T/(1 + T)$  was constructed. This plot was shifted by  $1/B$  to give a plot of  $A_{fv}$ . Figure 5.4 contains Bode plots of  $|A_{fv}|$  for the low- and high-torque cases.

$|A_{fv(\text{mid})}|$ ,  $M_{pf}$ , and  $f_p$  are indicated in Figure 5.4 for both the low- and high-torque cases. These values, plus those estimated by using the two-pole function approximation for  $T$  discussed earlier in this chapter, are given in Table 5.1.

A brief comparison of the closed-loop frequency parameters in Table 5.1 indicates that the two-pole function approximation for  $T$  discussed earlier is reasonable. The smaller peaking obtained with the graphical approach suggests the values of  $\xi$  in Equation (5.26) are somewhat smaller than would be expected. However, the expressions for  $T$  in Equations (5.17) and (5.18), should be accurate enough to give reliable error coefficients in a later analysis.

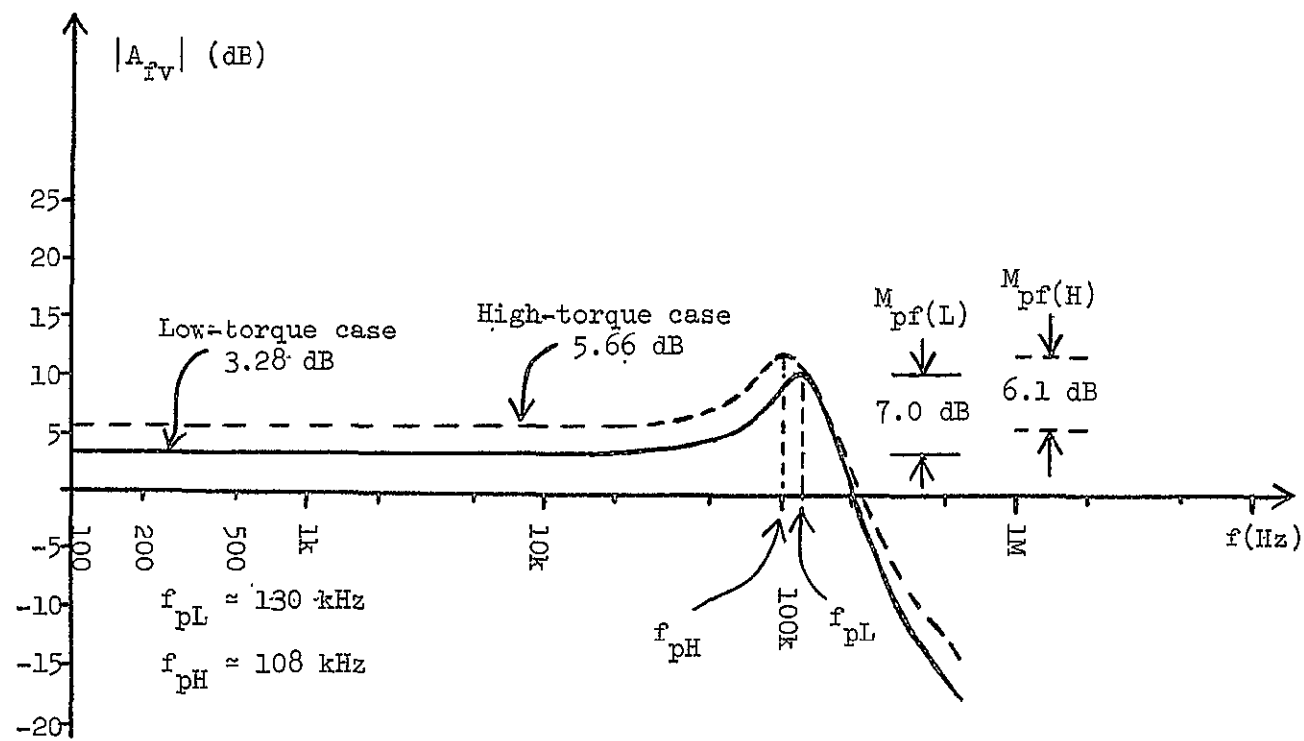


FIGURE 5.4

BODE PLOTS OF  $|A_{fv}|$  FOR THE LOW- AND HIGH-TORQUE CASES OF THE TORQUE CURRENT GENERATOR

One parameter given in Table 5.1 is the bandwidth, BW. As mentioned earlier, the BW is most commonly defined to be the frequency where the closed-loop frequency response magnitude is a factor of  $0.707 = 1/\sqrt{2}$  or -3dB of its midband value. The bandwidth is related to speed of response and to the overall control system ability to reproduce an input signal. Also, the ability of the system to reject unwanted noise or spurious disturbances anywhere in the system is to some degree a function of bandwidth.

The natural frequency  $f_n$  of the system dominant poles for most systems is closely related to the bandwidth. Consequently the bandwidth is a measure of the frequency of damped oscillation  $f_d$  of the closed-loop system. A short speed of response corresponds to a large bandwidth, and vice versa. Such statements do not account for nonlinear effects in the system. Saturating gain stages due to overdrive, and slew rate limitations produce effects in system behavior which are beyond an easy analysis.

Often there is the possibility that the input signal to a control system may be contaminated with noise. Perhaps unwanted fluctuations occur inside the system loop. A desirable feature of the system would be that it ignore these disturbances and use only the useful signals. In many cases such disturbances are of a higher frequency content than the highest significant frequency in the signal spectrum. In such cases, the bandwidth is representative of the "cutoff frequency", above which disturbances are attenuated.

From Table 5.1 one can note that the bandwidth of the TCG is approximately 200 kHz. While this may appear small compared to some systems previously designed, the BW is adequate to handle the signal spectrum for which the TCG was designed. Considering the parasitic oscillations of a higher frequency often found in power supply and logic lines, a larger BW seems undesirable at this time.

Reference will be made later in the thesis to much of the material in this section on closed-loop frequency response. Chapters on topics such as time domain characteristics of the TCG and noise considerations will certainly refer to some of the equations and parameters. More immediately, some of the equations will be used in the next section to analyze the steady state accuracy of the TCG.

#### B. Steady-State Accuracy of the Torque Current Generator

One of the most important characteristics of a system is its accuracy. A more accurate system will better process information and reject undesirable external disturbances. Error coefficients and error constants are classically used to provide a measure of the accuracy of a given control system.<sup>28</sup> The system's ability to minimize error is better described by error coefficients than by error constants.

The TCG loop, as illustrated in the simplified circuit of Figure 5.3, presents itself as a type of problem referred to as a regulator problem. The term regulator is used to refer to systems in which there is a constant steady-state value for a constant input signal.<sup>27</sup> When not switching torquing levels, the TCG does fit that description. In view of



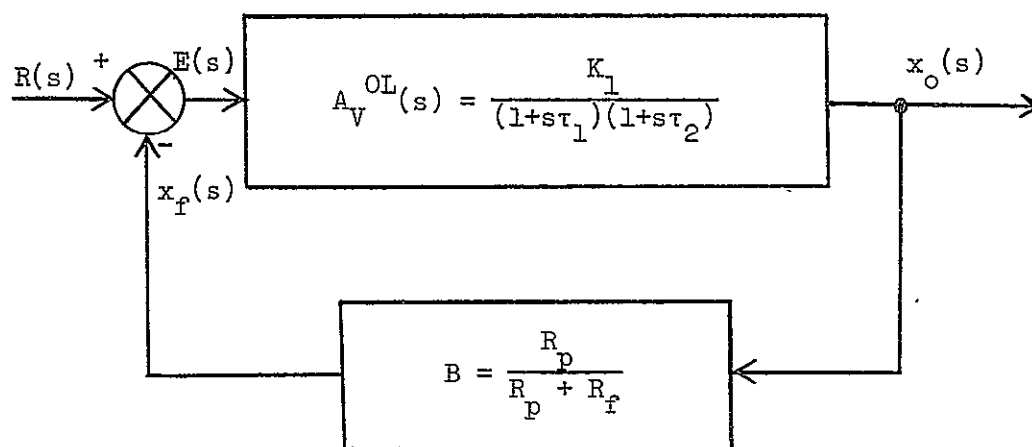
this situation, a logical way to estimate steady-state accuracy for the TCG appears to be the control systems approach.

The TCG loop may be represented by the block diagram illustrated in Figure 5.5. Since  $B$  is frequency independent over the region of interest,  $A_v^{OL}$  may be obtained from Equations (5.11) and (5.12) by dividing the expression for  $T$  by  $B$ .  $K_1$  is the magnitude of the midband open-loop voltage gain of the TCG loop. Also, the following relationships are employed:

$$\begin{aligned} s &= j\omega, \\ \omega &= 2\pi f, \\ \omega &= 1/\tau. \end{aligned} \tag{5.28}$$

$\tau$ , in the context used here, is a high-frequency time constant of the TCG loop.  $X_o(s)$  is the output voltage at the output of the current regulator.  $R(s)$  is the reference input voltage,  $X_f(s)$  is the voltage feedback signal, and  $E(s)$  is the actuating error. Parameter values of interest are given in a note in Figure 5.5 for the block diagram of the simplified TCG loop.

The definitions of error coefficients and error constants contained in most texts are for unity feedback systems. The concept may be extended to nonunity feedback systems, such as the TCG loop. Reference 28 gives a development of error coefficients for a unity feedback system. Only the results of a parallel development for a nonunity feedback system will be given here.



Note:  $K_1 \approx 1.36 \times 10^8$  for the low-torque case.  
 $K_1 \approx 1.41 \times 10^8$  for the high-torque case.  
 $R_p \approx 206.7 \, \Omega$  for the low-torque case.  
 $R_p \approx 103.3 \, \Omega$  for the high-torque case.  
 $R_f \approx 95.3 \, \Omega$  for the low- and high-torque cases.  
 $\left. \begin{array}{l} \tau_1 \approx 39.8 \text{ sec.} \\ \tau_2 \approx 3.18 \, \mu\text{sec} \end{array} \right\} \text{ for low- and high-torque cases.}$

FIGURE 5.5

BLOCK DIAGRAM OF THE SIMPLIFIED  
TORQUE CURRENT GENERATOR

The error transfer function for the feedback system illustrated in Figure 5.5 is

$$\begin{aligned} E(s)/R(s) &= \frac{1}{1 + A_{OL}(s)B} , \\ &= \frac{\tau_1 \tau_2 s^2 + (\tau_1 + \tau_2)s + 1}{\tau_1 \tau_2 s^2 + (\tau_1 + \tau_2)s + (K_1 B + 1)} . \end{aligned} \quad (5.29)$$

By definition let

$$W(s) = E(s)/R(s) , \quad (5.30)$$

so that

$$E(s) = W(s)R(s) . \quad (5.31)$$

The system-error impulse response  $w(t)$  may be defined as

$$w(t) = L^{-1} [W(s)] . \quad (5.32)$$

One can show that

$$\epsilon_{ss}(t) = \sum_{i=0}^{\infty} \frac{C_i r^{(i)}(t)}{i!} . \quad (5.33)$$

In Equation (5.33)

$$\begin{aligned} C_i &= (-1)^i \int_0^{\infty} \tau^i w(\tau) d\tau, \quad i = 0, 1, 2, \dots , \\ r^{(i)}(t) &= \frac{d^i r(t)}{dt^i} , \\ r^{(0)}(t) &= r(t) = \text{reference input} . \end{aligned} \quad (5.34)$$

Equation (5.33) is commonly referred to as the steady-state error series, or the actuating error under steady-state conditions. The constants  $C_i$  are known as the error coefficients of the system. The error coefficients dictate the steady-state error of the system for a large class of reference input functions. Reference 28 shows that

$$C_i = \lim_{s \rightarrow 0} \frac{d^i W(s)}{ds^i} . \quad (5.35)$$

Substitution of Equation (5.29) into Equation (5.30) gives

$$W(s) = \frac{\tau_1 \tau_2 s^2 + (\tau_1 + \tau_2)s + 1}{\tau_1 \tau_2 s^2 + (\tau_1 + \tau_2)s + (K_1 B + 1)} . \quad (5.36)$$

Equations (5.35) and (5.36) can now be used to determine the error coefficients of the TCG loop. Using these coefficients as figures of merit, the steady-state performance of the loop may be evaluated.

From Equations (5.35) and (5.36),

$$C_o = W(s) \Big|_{s=0} = \frac{1}{1 + K_1 B} = \frac{1}{1 + |T_{mid}|} . \quad (5.37)$$

If the input function is a unit step, then all the terms in Equation (5.35) but  $C_o$  will disappear. In that case, the system error in the steady-state is

$$\epsilon_{ss}(t) = C_o r(t) . \quad (5.38)$$

The reference input for the TCG loop may be considered as a constant times a unit step. Equation (5.38) applies, and  $C_n$  for  $n$  greater than zero need not be derived. Substitution of Equation (5.37) into Equation (5.38) gives

$$\epsilon_{ss}(t) = \left[ \frac{1}{1 + |T_{mid}|} \right] [r(t)] . \quad (5.39)$$

Values of  $|T_{mid}|$  for the low- and high-torque cases are given in Equations (5.15) and (5.16).  $r(t)$  is equal to the P.V.R., or 6.2 volts. Substitution of these values into Equation (5.39) yields the steady-state actuating error of the TCG loop for the low- and high-torque cases. These values are

$$\begin{aligned} \epsilon_{ss}(t) \text{ [L.T.]} &\approx 6.64 \times 10^{-8} \text{ volts ,} \\ \epsilon_{ss}(t) \text{ [H.T.]} &\approx 8.46 \times 10^{-8} \text{ volts .} \end{aligned} \quad (5.40)$$

The system error coefficients are a generalization of the error constants and can be used for a large variety of input functions. The error constants provide a steady-state error measure for systems excited by step, ramp, and parabolic inputs. There exists a correlation between the first three error coefficients and the error constants. Since the mechanics of the error coefficients have already been obtained, a derivation of the error constants would be redundant on the one hand and less enlightening on the other. No effort will be made to ascertain these parameters.

A few general comments can be made regarding Equation (5.39). For a given input,  $r(t)$ ,  $\epsilon_{ss}(t)$  is inversely proportional to the magnitude of  $T_{mid}$ . The magnitude of  $T_{mid}$  must be made larger if a greater final accuracy is desired. This indicates that, for high accuracy, the open-loop gain  $A_v^{OL}$  should be large. In that case, even the smallest detectable error signal may be amplified and produce a correction to the input. On the other hand, if  $|T_{mid}|$  is made too large, oscillations with sustained or increasing amplitude may develop and cause instability. In the sense that increasing stability decreases accuracy, and vice versa, the features of accuracy and stability are opposites.

A note of caution concerning the correct use of the error coefficients discussed above is in order. There is a constraint which must be placed upon the physical system in order for the error series to be valid. This constraint is that the system-error impulse response must decay much faster than any exponential factors associated with the input function.

Only  $C_0$  of the error coefficients was determined in this study since the input  $r(t)$  was assumed to be a constant times the unit step. However, if the constraint mentioned above is obeyed, any input waveform which can be written as a function  $r(t)$  can be used. Additional error coefficients can be generated using Equation (5.35). The number of error coefficients that need to be generated is determined by the characterization of the input function, and by the rapidity with which the error series converges.  $W(s)$  is usually relatively simple to determine for a given system. The error coefficients can then be generated quite rapidly by differentiating  $W(s)$  and substituting a zero everywhere an  $s$  is seen.

The above discussion on steady-state accuracy has dealt with the subject only from the control systems approach. The error of concern here was the steady-state actuating error, and error coefficients were chosen as figures of merit to indicate steady-state accuracy. Such errors as drift error in the P.V.R., error in the sensed current due to offset currents, and errors due to rise- and fall-time differences will be discussed in a later chapter. The steady-state actuating errors obtained above will be tabulated, along with other errors of the TCG, in a summary section of the conclusions chapter. Attention is now turned to another facet of the stability of the TCG against temperature variations, aging, and semiconductor device replacement.

## CHAPTER VI

### STABILITY OF THE TCG AGAINST VARIATIONS DUE TO TEMPERATURE, AGING AND SEMICONDUCTOR DEVICE REPLACEMENT

The discussion on the stability of the TCG loop of the U.T. pulse rebalance electronics system continues from Chapter V. The emphasis in this chapter is on stability of the TCG loop against variations due to temperature, component aging, and semiconductor device replacement.

The method of attack on the thermal stability of the TCG loop will be to determine the magnitude of the loop gain at midband as a function of parameters which are in turn functions of temperature. Then the change in  $|T_{mid}|$  with temperature can be evaluated by the chain rule. The variation of the pole locations with temperature will be examined. Transistors which are in critical positions in the loop will be investigated for thermal runaway. The pulse rebalance electronics will be housed in a temperature regulated environment of approximately 50°C. The temperature band used in this analysis will be 45°C to 55°C. The results found for parameter variations due to temperature changes will also apply to parameter variations due to component aging and replacement. Thus a separate analysis for current gain variations with transistor replacement, etc., will not be necessary.

#### A. The Effect of Temperature Variations Upon $|T_{mid}|$ of the TCG

The problem of loop gain variation with temperature in the TCG loop is much simplified if the H-switch and sampling resistor switching



network are considered invariant with temperature. There is strong argument for neglecting the temperature effects in these circuits. This argument was presented in Reference 4 by the author, and will not be repeated here in order to conserve space. Rather, the assumption will be made that the effects upon  $|T_{mid}|$  caused by temperature-related variations in the parameters of the H-switch and sampling resistor switching network are negligible.

The sampling resistors used in a pulse rebalance electronics system should be high-quality precision resistors with close tolerances. Since ample burn-in is usually associated with such resistors, they will be assumed temperature stable.

In view of the above discussion, the feedback factor, B, (as identified in Equation (5.10)), can be assumed invariant in the temperature band of  $50^{\circ}\text{C} \pm 5^{\circ}\text{C}$ . Therefore, the thermal stability of the op. amp., the error amplifier, and the Darlington pair output of the current regulator is the problem at hand.

From Figure 3.1, and the material in Appendix E, the loop transmission of the TCG may be written

$$T_L = [A_{v1} A_1 A_{d1} A_2] B . \quad (6.1)$$

In Equation (6.1),  $A_{v1}$  is the open-loop voltage gain of the op. amp.;  $A_1$  is the voltage division term from the output of the op. amp. to the input of Q1A;  $A_{d1}$  is the voltage gain from the base of Q1A to the collector of Q1B;  $A_2$  is the voltage gain from the collector of Q1B to the emitter

of Q3; and, B is the feedback factor.  $T_L$  is used for loop transmission in this chapter to distinguish it from the symbol for temperature, T.

The change in the loop transmission with respect to a change in temperature is given by

$$\begin{aligned} \frac{dT_L}{dT} = & \left[ \frac{\partial T_L}{\partial A_{v1}} \frac{dA_{v1}}{dT} + \frac{\partial T_L}{\partial A_1} \frac{dA_1}{dT} + \frac{\partial T_L}{\partial A_{d1}} \frac{dA_{d1}}{dT} \right. \\ & \left. + \frac{\partial T_L}{\partial A_2} \frac{dA_2}{dT} + \frac{\partial T_L}{\partial B} \frac{dB}{dT} \right] . \end{aligned} \quad (6.2)$$

Each of the terms in Equation (6.2) will need to be evaluated or estimated to obtain the total change in  $T_L$  with a change in T.

From the manufacturer's data,  $\frac{dA_{v1}}{dT}$  can be estimated for the AD504M op. amp. over the temperature band of interest to be

$$\frac{dA_{v1}}{dT} \approx \frac{\Delta A_{v1}}{\Delta T} \approx \frac{3000}{^\circ\text{C}} . \quad (6.3)$$

This applies to both torquing levels of the TCG.

From Figure 3.1, the expression for  $A_{d1}$  may be written

$$A_{d1} \approx \frac{(\beta_{1B})(R6)}{(\beta_{1B} + 1)[r_{e1A} + R7 + R8 + r_{e1B} + \frac{R9}{(\beta_{1B} + 1)}]} . \quad (6.4)$$

One may note that  $A_{d1} = f_1(r_{e1A}, r_{e1B}, \beta_{1B})$ ,  $r_{e1A} = f_2(I_{E1A}, T)$ ,  $r_{e1B} = f_3(I_{E1B}, T)$ , and  $I_E \approx I_C = f_4(V_{BE}, I_{CO}, \beta)$ .  $V_{BE}$ ,  $I_{CO}$ , and  $\beta$  are all

temperature dependent terms. The rate of change of  $A_{dl}$  with temperature is

$$\frac{dA_{dl}}{dT} = \frac{\partial A_{dl}}{\partial r_{elA}} \frac{dr_{elA}}{dT} + \frac{\partial A_{dl}}{\partial r_{elB}} \frac{dr_{elB}}{dT} + \frac{\partial A_{dl}}{\partial \beta_{lB}} \frac{d\beta_{lB}}{dT} \quad (6.5)$$

This assumes that the fixed resistors have zero temperature coefficients, or have temperature coefficients which are negligible compared to other parameter changes.

The variation of  $r_e$  with  $T$  can be expressed as

$$\frac{dr_e}{dT} = \frac{\partial r_e}{\partial T} + \frac{\partial r_e}{\partial I_E} \frac{dI_E}{dT} \quad (6.6)$$

But,

$$r_e = \frac{K T}{q I_E} \quad (6.7)$$

where  $K$  is Boltzmann's constant ( $1.381 \times 10^{-23}$  J/°K),  $T$  is the temperature in degrees Kelvin,  $q$  is the electronic charge ( $1.601 \times 10^{-19}$  Coulomb), and  $I_E$  is the emitter current. Substituting Equation (6.7) into Equation (6.6) gives

$$\frac{dr_e}{dT} = \left( \frac{K}{q} \right) \left[ \frac{1}{I_E} - \frac{T}{I_E^2} \frac{dI_E}{dT} \right] \quad (6.8)$$

Q1A and Q1B form a differential amplifier stage. R7 and R8 are large enough to aid considerably in bias stability since they are

unbypassed emitter resistors. The stability factors defined and discussed in Reference 31 may be used to estimate  $\frac{dI_E}{dT}$ . From this, and the discussion on multistage biasing in Reference 36, one can form a strong case for assuming  $\frac{dI_{E1}}{dT} \approx 0$  and neglecting  $V_{BE1}$  changes with  $\pm 5^\circ\text{C}$  variation around  $50^\circ\text{C}$ . Assuming  $\frac{dI_E}{dT} \approx 0$  in the temperature band of interest, Equation (6.8) becomes

$$\frac{dr_e}{dT} \approx \frac{K}{qI_E} \quad (6.9)$$

The dependence of  $\beta$  on temperature variations is difficult to accurately describe. As a best estimate, the value of  $\beta$  at room temperature will be expected to increase or decrease  $1\%/^\circ\text{C}$  (on a simple interest-type rate) with increasing or decreasing temperature respectively.

From Equation (6.4),

$$\frac{\partial A_{d1}}{\partial r_{e1A}} = \frac{-\beta_{1B} R_6}{(\beta_{1B} + 1) [r_{e1A} + r_{e1B} + R_7 + R_8 + \frac{R_9}{(\beta_{1B} + 1)}]^2} \quad (6.10)$$

$$\frac{\partial A_{d1}}{\partial r_{e1B}} = \frac{-\beta_{1B} R_6}{(\beta_{1B} + 1) [r_{e1A} + r_{e1B} + R_7 + R_8 + \frac{R_9}{(\beta_{1B} + 1)}]^2} \quad (6.11)$$

$$\begin{aligned} \frac{\partial A_{dl}}{\partial \beta_{lB}} = & \frac{\beta_{lB}(R6)(R9)}{(\beta_{lB} + 1)^3 [r_{elA} + r_{elB} + R7 + R8 + \frac{R9}{(\beta_{lB} + 1)}]^2} \\ & + \frac{R6}{(\beta_{lB} + 1)^2 [r_{elA} + r_{elB} + R7 + R8 + \frac{R9}{(\beta_{lB} + 1)}]} \quad (6.12) \end{aligned}$$

Equations (6.9) through (6.12) may be substituted into Equation (6.5) to evaluate the rate of change of  $A_{dl}$  with temperature. Obviously,  $\frac{dA_{dl}}{dT}$  depends upon bias levels which depend upon torquing modes. The remainder of the general expressions needed to evaluate  $\frac{dT_L}{dT}$  will be obtained before considering the specific cases of low- and high-torquing levels.

From Appendix E,

$$\begin{aligned} A_l = & \frac{R_{ilA}}{R_{ilA} + R4} \quad , \\ = & \frac{(\beta_{lA} + 1)[r_{elA} + r_{elB} + R7 + R8 + \frac{R9}{\beta_{lB} + 1}]}{(\beta_{lA} + 1)[r_{elA} + r_{elB} + R7 + R8 + \frac{R9}{\beta_{lB} + 1}] + R4} \quad (6.13) \end{aligned}$$

$$\frac{dA_l}{dT} = \frac{\partial A_l}{\partial R_{ilA}} \frac{dR_{ilA}}{dT} \quad (6.14)$$

$R_{ilA}$  is a function of four temperature dependent terms:  $r_{elA}$ ,  $r_{elB}$ ,  $\beta_{lA}$ , and  $\beta_{lB}$ . Consequently,

$$\begin{aligned} \frac{dR_{11A}}{dT} &= \frac{\partial R_{11A}}{\partial r_{e1A}} \frac{dr_{e1A}}{dT} + \frac{\partial R_{11A}}{\partial r_{e1B}} \frac{dr_{e1B}}{dT} \\ &+ \frac{\partial R_{11A}}{\partial \beta_{1A}} \frac{d\beta_{1A}}{dT} + \frac{\partial R_{11A}}{\partial \beta_{1B}} \frac{d\beta_{1B}}{dT} . \end{aligned} \quad (6.15)$$

The partial derivatives of  $R_{11A}$  with respect to its temperature dependent terms may be written with the aid of Equation (6.13).

$$\frac{\partial R_{11A}}{\partial r_{e1A}} = (\beta_{1A} + 1) . \quad (6.16)$$

$$\frac{\partial R_{11A}}{\partial r_{e1B}} = (\beta_{1A} + 1) . \quad (6.17)$$

$$\frac{\partial R_{11A}}{\partial \beta_{1A}} = [r_{e1A} + r_{e1B} + R7 + R8 + \frac{R9}{\beta_{1B} + 1}] . \quad (6.18)$$

$$\frac{\partial R_{11A}}{\partial \beta_{1B}} = \frac{-(\beta_{1A} + 1)R9}{(\beta_{1B} + 1)^2} . \quad (6.19)$$

From Equation (6.13),

$$\frac{\partial A_1}{\partial R_{11A}} = \frac{R4}{(R_{11A} + R4)^2} . \quad (6.20)$$

Now all the necessary equations are available to evaluate Equation (6.14), which is the  $\frac{dA_1}{dT}$  term.

Next, consider the  $\frac{dA_2}{dT}$  term. The simplified expression for  $A_2$ , taken from Appendix E, is

$$A_2 = \frac{(\beta_3 + 1)R_B}{r_{e2B} + (\beta_3 + 1)(r_{e3} + R_B)} \quad (6.21)$$

The derivative of  $A_2$  with respect to temperature may be written

$$\frac{dA_2}{dT} = \frac{\partial A_2}{\partial \beta_3} \frac{d\beta_3}{dT} + \frac{\partial A_2}{\partial r_{e2B}} \frac{dr_{e2B}}{dT} + \frac{\partial A_2}{\partial r_{e3}} \frac{dr_{e3}}{dT} \quad (6.22)$$

The expression for  $\frac{dr_e}{dT}$  has already been derived and given as Equation (6.8). When the differential stage gain  $A_{dl}$  was considered, the dependence of the  $\frac{dr_e}{dT}$  term upon  $\frac{dI_E}{dT}$  was neglected as being small compared to other parameter changes. However, in the case of  $A_2$ , which is associated with a Darlington pair, the  $\frac{dI_E}{dT}$  effect should be taken into account. Temperature stabilization of a Darlington stage is often extremely difficult. The temperature-dependent reverse collector current  $I_{CO}$  of the first transistor in the pair (Q2B in the case at hand) flows at the base of the composite unit just as it would for a single transistor unit. Since the composite  $\beta$  is very large, only a very small base current is needed to control the complete collector-current flow. But  $I_{CO}$  is of the same order of magnitude. Herein lies the temperature stabilization problem. The overall feedback of the TCG alleviates this problem with the Darlington stage to a large extent. The current through Q3 is maintained at the specified torquing level by feedback action. However, for a worst

case analysis, feedback will be ignored and the effect of  $\frac{dI_E}{dT}$  upon  $\frac{dA_2}{dT}$  will be investigated.

Reference 37 makes for informative reading on current-gain temperature dependence in silicon transistors, but isn't very useful for the problem at hand. Reference 38 has some useful equations involving the change in  $I_C$  with temperature. Because of the more suitable arrangement of the equations for the present application, the following material is taken from Reference 31.

$$\Delta I_C = S \Delta I_{CO} + S' \Delta V_{BE} + S'' \Delta \beta \quad (6.23)$$

$$S \equiv \frac{\partial I_C}{\partial I_{CO}} = \frac{(\beta + 1) \left(1 + \frac{R_b}{R_e}\right)}{(\beta + 1) + \frac{R_b}{R_e}} \quad (6.24)$$

$$S' \equiv \frac{\partial I_C}{\partial V_{BE}} = \frac{-\frac{\beta}{R_e}}{\beta + 1 + \frac{R_b}{R_e}} \quad (6.25)$$

$$S'' \equiv \frac{\partial I_C}{\partial \beta} = \frac{I_C S}{\beta(\beta + 1)} \quad (6.26)$$

In Equations (6.24) and (6.25),  $R_b$  is the effective resistance seen looking back from the base terminal.  $R_e$  is any fixed resistance contained in the emitter circuit. Since  $I_E \approx I_C$ , Equation (6.23) approximately holds for  $\Delta I_E$  also. Since  $\frac{dI_E}{dT} \approx \frac{\Delta I_E}{\Delta T}$ , Equations (6.23) through (6.26) can be used to approximate the  $\frac{dI_E}{dT}$  term in Equation (6.8).



Returning to Equation (6.22), the partial derivatives of  $A_2$  with respect to  $\beta_3$ ,  $r_{e2B}$ , and  $r_{e3}$  may be written.

$$\frac{\partial A_2}{\partial r_{e2B}} = \frac{-(\beta_3 + 1)R_B}{[r_{e2B} + (\beta_3 + 1)(r_{e3} + R_B)]^2} . \quad (6.27)$$

$$\frac{\partial A_2}{\partial r_{e3}} = \frac{-(\beta_3 + 1)^2 R_B}{[r_{e2B} + (\beta_3 + 1)(r_{e3} + R_B)]^2} . \quad (6.28)$$

$$\frac{\partial A_2}{\partial \beta_3} = \frac{r_{e2B} R_B}{[r_{e2B} + (\beta_3 + 1)(r_{e3} + R_B)]^2} . \quad (6.29)$$

Before going to the specific low- and high-torque case, Equation (6.1), will be used to obtain partial derivatives of  $T_L$ .

$$\frac{\partial T_L}{\partial A_{v1}} = A_{v1} A_{d1} A_2^B . \quad (6.30)$$

$$\frac{\partial T_L}{\partial A_{d1}} = A_{v1} A_{d1} A_2^B . \quad (6.31)$$

$$\frac{\partial T_L}{\partial A_{d1}} = A_{v1} A_{d1} A_2^B . \quad (6.32)$$

$$\frac{\partial T_L}{\partial A_2} = A_{v1} A_1 A_{d1} B . \quad (6.33)$$

$$\frac{\partial T_L}{\partial B} = 0, \quad (6.34)$$

since B is being considered invariant with temperature.

The results obtained in this chapter thus far are of a general nature and apply to both the low- and high-torquing modes of the TCG. The equations necessary to evaluate Equation (6.2) are now available. To conserve space, the equations derived earlier in the chapter will not be combined any further in a formal way. The necessary substitutions, etc., will be made for the low- and high-torque cases and only the results will be given. Table 6.1 lists some parameter values useful in calculating  $\frac{dT_L}{dT}$ .

#### Loop Transmission Variation with Temperature for the Low-Torque Mode

The low-torque or normal level of the torquing current is 30mA. The device parameters needed to evaluate the equations developed earlier for the low-torque case are given in Table 6.1, or in Figure 3.1.

Equation (6.2), when properly evaluated for the low-torque case, yields

$$\frac{dT_L}{dT} \text{ (L.T.)} \approx -358092/^{\circ}\text{C} \quad (6.35)$$

for an increasing temperature. Inversely, the loop gain increases with decreasing temperature.

TABLE 6.1

PARAMETER VALUES USED IN TEMPERATURE CALCULATIONS

	<u>High-Torque Case</u>				<u>Low-Torque Case</u>			
	Q1A	Q1B	Q2B	Q3	Q1A	Q1B	Q2B	Q3
$I_E$ (mA)	1.7	3.3	0.430	60	1.3	3.7	0.231	30
$V_{CE}$ (V)	35.9	15.1	20.9	21.6	36.0	12.7	23.4	24.1
	110	135	50	140	100	140	40	130
$r_e$ ( $\Omega$ )	15.3	7.88	60.5	0.433	20	7.03	113	0.867
$P_D$ rating (Watts)	0.5	0.5	0.5	1W	0.5	0.5	0.5	1W
	(0.6 Total package)			10W, if heat sunked				
$P_D$ (Actual) (Watts)	.061	.050	.009	1.30	.0468	.047	.0054	.723

Note:

Q1 = 2N5794

Q2 = 2N5794

Q3 = MPS-U06

In order to obtain an expression of the percentage change in  $T_L$  with temperature, note that

$$\Delta T_L \approx \frac{dT_L}{dT} \Delta T . \quad (6.36)$$

Then, the percentage change in  $T_L$ ,  $\Delta T_L(\%)$ , can be expressed as

$$\Delta T_L(\%) = \frac{\Delta T_L}{|T_L|} \times 100\% = \frac{\frac{dT_L}{dT} \cdot \Delta T}{|T_L|} \times 100\% . \quad (6.37)$$

Substitution of Equation (6.35), along with  $|T_L| = 93.3 \times 10^6$  and  $\Delta T = +5^\circ\text{C}$ , into Equation (6.37) yields

$$\Delta T_L(\%) \left| \begin{array}{l} \text{L.T.} \\ \Delta T = +5^\circ\text{C} \end{array} \right. \approx -1.919\% . \quad (6.38)$$

The relative values obtained when calculating  $\frac{dT_L}{dT}$  indicate that the predominant factor influencing the change in  $T_L$  with temperature is the temperature coefficient of the AD504M op. amp. In fact, when  $\Delta T_L(\%)$  is calculated using only the  $\left( \frac{\partial T_L}{\partial A_{v1}} \frac{dA_{v1}}{dT} \right)$  B term, the result is

$$\Delta T_L(\%) \left| \begin{array}{l} \text{L.T.} \\ \Delta T = +5^\circ\text{C} \end{array} \right. \approx -1.919\% . \quad (6.39)$$

Since Equations (6.38) and (6.39) give the same results to three decimal places, calculations for the high-torque case can be simplified to account only for the term associated with  $A_{v1}$ .

In actuality, the loop transmission obtained in Chapter IV was for an ambient temperature of 25°C. The parameter values in Table 6.1 are likewise for  $T = 25^\circ\text{C}$ . Calculations were performed to approximate the loop gain change as  $T$  increased from 25°C to 55°C. The results of that calculation indicate that the loop gain decreases approximately 11.5%. If the poles of  $T_L$  are little affected by the  $\Delta T$ , then the decrease in gain certainly won't adversely affect the stability of the loop. Pole shift with temperature will be investigated after obtaining  $\Delta T_L(\%)$  for the high-torque case.

#### Loop Transmission Variation with Temperature for the High-Torque Mode

The high-torque level of the torquing current is 60mA. All terms in Equation (6.2), except the  $\left[ \frac{\partial T_L}{\partial A_{v1}} \frac{A_{v1}}{dT} \right] B$  term will be neglected. Substitution of proper values into Equation (6.2) and associated equations gives

$$\frac{dT_L}{dT} (\text{H.T.}) \approx -275292/^\circ\text{C} . \quad (6.40)$$

$$\Delta T_L(\%) \left| \begin{array}{l} \text{H.T.} \\ \Delta T = +5^\circ\text{C} \end{array} \right. \approx -1.875\% . \quad (6.41)$$

The dependence of the pole locations of  $T_L$  is necessary before conclusive statements can be made about dynamic thermal stability. This subject will be investigated next.

### Effect of Temperature Variations Upon the Location of Poles of the Loop Transmission

The gain factors of the loop transmission of the TCG change as temperature varies. This topic has been discussed above. The pole locations of  $T_L$  also vary with temperature. A reasonable approximation of the percentage change in the time constants of the loop can be theoretically derived with the exception of the op. amp. The gain change in  $T_L$  with temperature variations is dominated by the op. amp. Perhaps this is so with the shift in pole locations, but insufficient information is presently available for making such a calculation. According to the manufacturer, every AD504M is stored for 48 hours at +200°C and temperature cycled 10 times from -65°C to +200°C to assure reliability and long-term stability. The concept of thermal symmetry has been used in the design of the AD504M to minimize the effects of thermal gradients developed within the chip. The design is such that the input NPN transistors account for the major portion of the amplifier's temperature drift. In view of this, and for lack of anything more informative, the poles of the op. amp. will be assumed to be stable with a  $\pm 5^\circ\text{C}$  variation around the temperature environment.

As explained in Appendix E, the remaining pertinent poles and zeros of the TCG loop (other than those associated with the op. amp.) are contained in the interaction of the output of Q1B, the input of Q2B, and the RC lag network. The equations for the two poles and zero are given as Equations (E.14), (E.15), and (E.16) in Appendix E. The expressions for the two poles contain some parameters which are temperature dependent.

This in turn makes the pole values temperature dependent. An analysis similar to that for obtaining  $\frac{dT_L}{dT}$  was made for each of the two poles for a  $\pm 5^\circ\text{C}$  variation around the operating temperature of the TCG. Again, to conserve space, only the results will be given here.

Consider first the expression for  $f_{p1}$ . From Equation (E.14), Appendix E,

$$\begin{aligned} f_{p1} &\approx \frac{1}{2\pi R_{Leq1B} (C_{Leq1B} + C_c)} , \\ &\approx 64 \text{ kHz} . \end{aligned} \quad (6.42)$$

The results of calculations on the temperature dependence of  $f_{p1}$  are:

$$\Delta f_{p1}(\%) \bigg|_{\Delta T = -5^\circ\text{C}} \approx -0.00733\% ; \quad (6.43)$$

and

$$\Delta f_{p1}(\%) \bigg|_{\Delta T = +5^\circ\text{C}} \approx +0.004\% . \quad (6.44)$$

Next, consider the expression for  $f_{p2}$ . From Equation (E.15), Appendix E,

$$\begin{aligned} f_{p2} &\approx \frac{1}{2\pi R_c \left[ \frac{C_{Leq1B} C_c}{C_{Leq1B} + C_c} \right]} , \\ &\approx 2.86 \text{ MHz} . \end{aligned} \quad (6.45)$$

Calculations on the temperature dependence of  $f_{p2}$  yield the following:

$$\Delta f_{p2}(\%) \bigg|_{\Delta T = -5^{\circ}\text{C}} \approx -0.263\% ; \quad (6.46)$$

and

$$\Delta f_{p2}(\%) \bigg|_{\Delta T = +5^{\circ}\text{C}} \approx +0.144\% . \quad (6.47)$$

The zero defined by Equation (E.16), Appendix E, is assumed to be temperature invariant. This zero is a function only of a fixed resistance and a fixed capacitance whose values are assumed constant within the narrow band of  $\Delta T = \pm 5^{\circ}\text{C}$ .

The percentage changes in  $f_{p1}$  and  $f_{p2}$  given above are those calculated using the parameter values associated with the low-torquing mode. These percentages are higher than those obtained for the high-torquing mode and will be considered a worst-case condition.

The changes in the pole locations of  $T_L$  which were investigated immediately above would scarcely show up on a Bode plot of  $T_L$ . The magnitude change in  $T_L$  with  $\Delta T$  has already been found to be decreasing with increasing temperature. Since the TCG loop has been proven stable at  $25^{\circ}\text{C}$  (well below the temperature environment of the system), the higher operating temperature results in a lower  $|T_L|$ , but with very little shift in the poles and zeros of  $T_L$ . Consequently, one may conclude that the changes in the magnitude, poles, and zeros of  $T_L$ , with a  $\Delta T$  of  $\pm 5^{\circ}\text{C}$  about  $50^{\circ}\text{C}$ , pose no threat to the stability against oscillations of the TCG loop.



### Thermal Runaway Possibilities in the TCG Loop

A brief study of Figure 3.1, along with bias levels and device limitations, indicates that only one active device in the TCG loop is in any danger of thermal runaway. This device is Q3, which is a MPS-U06 bipolar transistor. The transistor, as indicated in Table 6.1, has a  $P_D$  (max) of 1W at an ambient temperature of 25°C, or 10W if properly heat-sinked.  $P_D$  (max) must be derated above 25°C by 8mW/°C if the device is not heat-sinked, and 80mW/°C if it is heat-sinked. The circuit is to operate in a temperature environment of approximately 50°C. The result of derating gives a  $P_D$  (max) of 0.8W if not heat-sinked, and a  $P_D$  (max) of 8.0W if heat-sinked.

Table 6.1 has the actual power dissipation of Q3 listed for the low- and high-torque modes.  $P_D$  (actual) for the low-torque mode approaches  $P_D$  (max) for the MPS-U06 at 50°C and without a heat sink.  $P_D$  (actual) for the high-torque mode exceeds  $P_D$  (max) for the device at 50°C and without a heat sink. Consequently, Q3 must be heat-sinked to adequately handle the power dissipation required in the device for high-torquing levels. Once properly heat-sinked, Q3 can deliver a wide range of torquing current without danger of overheating. For example, if 200mA were used to drive the Kearfott Model 2544 gyro, only 2.3W would be dissipated in Q3.

The results obtained in this chapter are indicative of the effects to be expected due to active parameter changes. These changes may be prompted by temperature variations, aging, or device replacement. No attempt has been made to evaluate changes in the loop transmission due to changes in passive devices with temperature.

## CHAPTER VII

### TIME DOMAIN CHARACTERISTICS OF THE TORQUE CURRENT GENERATOR LOOP

Frequency domain characteristics of the TCG loop were treated in Chapters IV and V. There exists a correlation between sinusoidal and time responses. The purpose of this chapter is to use that correlation to determine some of the time domain characteristics of the TCG loop. Closed-loop frequency domain specifications of bandwidth, frequency of peaking, and resonant peak for the loop are given in Table 5.1.

The bandwidth BW is related to speed of response, to the ability of the TCG to reproduce an input signal, and to the ability of the loop to reject unwanted noise or spurious disturbances anywhere in the loop. A short discussion on the implications of BW was given in Chapter V and will not be repeated here.

The resonant peak,  $M_{pf}$ , is related to step response overshoot in the time domain. Generally, a greater peaking indicates a larger overshoot, a smaller risetime, and a longer settling time. The inverse applies for a situation with lesser peaking. However, for damping ratios of  $\xi < 0.4$ ,  $M_{pf}$  is not a good indication of overshoot. The damping ratio for the TCG loop, as indicated in Equation (5.26), is certainly less than 0.4 for both the low- and high-torque cases. Because of this, as well as ease of manipulation, another approach using open-loop frequency characteristics will be used to obtain closed-loop time domain characteristics of the TCG loop.

Reference 29 outlines the procedure to be used here to find the following for a second-order system:

$\xi$  = the damping ratio;

$t_p$  = the time to the peak value of the first overshoot;

$T_s$  = the settling time, which is defined as the time  
required for the signal in question to reach  
and remain within 2% of its final value;

$t_r$  = risetime (10% to 90%);

$M_{pt}$  = percentage overshoot.

The parameters listed above are in response to a step input signal. Only the magnitude crossover frequency,  $f_c$ , and the phase margin, P.M., of the loop transmission frequency response are required to be able to apply the procedure. Thereafter, the parameters mentioned above can be found from plots of P.M. versus  $\xi$ ,  $f_c t_r$  versus  $\xi$ , etc. Bode plots of the loop transmission of the TCG versus frequency for the high- and low-torque modes are found in Figure 4.5.  $f_c$  and P.M. can be read directly from these plots.

The loop transmission of the TCG is not a second-order system. This is obvious by studying Equations (E.23) and (E.24) in Appendix E. However, as argued in Appendix E,  $T$  may be approximated within a reasonable error by a second-order function. Hence, the procedure outlined in Reference 29 should give reasonable values of  $\xi$ ,  $t_r$ , etc.

Before proceeding with finding the closed-loop time domain characteristics of the TCG loop, perhaps a few words concerning the signal

of interest are in order. In Chapter IV, an open-loop voltage gain of the loop was used in conjunction with the feedback factor to obtain the loop gain  $T$ . Chapter V contains further discussion which indicates that the closed-loop signal to be characterized here is the voltage at the emitter of Q3, i.e., at the top of the H-switch.

#### A. The Low-Torque Case

Using Figure 4.5,

$$f_c(\text{L.T.}) \approx 130 \text{ kHz} , \quad (7.1)$$

and

$$\text{P.M.}(\text{L.T.}) \approx 27^\circ \quad (7.2)$$

for the low-torque case. From the P.M. versus  $\xi$  plot in Reference 29, the value of  $\xi$  corresponding to a P.M. of  $27^\circ$  can be estimated as

$$\xi(\text{L.T.}) \approx 0.24 . \quad (7.3)$$

Using this value of  $\xi$  and plots of time domain characteristics versus  $\xi$  in Reference 29, the following values were obtained for the low-torque case:

$$\begin{aligned} M_{pt}(\text{L.T.}) &\approx 45\% ; \\ t_p(\text{L.T.}) &\approx 3.6\mu\text{s} ; \\ t_r(\text{L.T.}) &\approx 1.4\mu\text{s} ; \\ T_s(\text{L.T.}) &\approx 19\mu\text{s} . \end{aligned} \quad (7.4)$$

### B. The High-Torque Case

$f_c$  and P.M. may again be read from Figure 4.5 for the high-torque case and are

$$f_c(\text{H.T.}) \approx 105 \text{ kHz} , \quad (7.5)$$

and

$$\text{P.M.}(\text{H.T.}) \approx 30^\circ . \quad (7.6)$$

The value of  $\xi$  corresponding to a P.M. of  $30^\circ$  is

$$\xi \approx 0.26 . \quad (7.7)$$

The associated values of the time domain characteristics are estimated from graphs to be:

$$\begin{aligned} M_{pt}(\text{H.T.}) &\approx 40\% ; \\ t_p(\text{H.T.}) &\approx 4.1\mu\text{s} ; \\ t_r(\text{H.T.}) &\approx 1.68\mu\text{s} ; \\ T_s(\text{H.T.}) &\approx 19.0\mu\text{s} . \end{aligned} \quad (7.8)$$

The closed-loop time domain parameters given in Equations (7.4) and (7.8) describe the voltage waveform which should occur at the emitter of Q3 in response to a step input signal at the input of the op. amp. This assumes a linear system with no overdrive or nonlinear problems.

However, as pointed out earlier in the thesis, the op. amp. is slew-rate limited. When the sampling resistor is switched, an approximate 3.8V signal appears at the input of the op. amp. until the feedback mechanism can correct. The time around the TCG loop is short enough for some correction to be in effect before the op. amp. can respond wholly to the abrupt 3.8V change at its input. Because of the slew rate limitation of the op. amp. and the overdrive at its input, the parameters in Equations (7.4) and (7.8) are not truly descriptive of what occurs at the emitter of Q3 when the sampling resistors are switched. However, for small perturbations at the input of the op. amp. or internal to the loop, they should be valid enough to partially characterize the behavior of the circuit.

Signals throughout the TCG loop are of interest. However, the prime signals of interest are those associated with the torquer coil of the gyro. As is so often the case, the signals of greatest interest are those most difficult to analytically characterize. Such is the case here. In Chapter V, the impedance looking into the top of the H-switch was shown to appear purely resistive over the operating frequency range of the TCG. This was done with a PCAP computer program which assumes a sinusoidal excitation. What the impedance looking into the top of the H-switch might appear to be in response to a step function excitation has not been determined. The PCAP program was written assuming alternate legs of the H-switch fully on or off. In actuality, the alternate legs of the H-switch are being switched from off to on, or vice versa, at a 2.4 kHz rate. The model used in the PCAP program is certainly not

adequate for these circumstances. The compensation for the torquer coil was determined by using a sinusoidal excitation at a 2.4 kHz rate. In reality, the torquer coil is not driven by a sinusoidal signal, but by a current pulse train with changing polarity. How adequate the compensation of the torquer is to make the torquer appear purely resistive under actual torquing conditions is a question difficult to answer. A further complication is involved when the sampling resistors are rapidly switched. One end of the torquer coil sees a voltage change (and consequently a current change) occur from the top of the H-switch because of the normal unilateral flow of signal around the loop. In addition, the other end of the torquer coil sees a voltage change which comes through the bottom of the H-switch, and emanates from the voltage change across the sampling resistors as a result of switching resistor values.

The above brief discussion serves to point out some of the difficulties to be encountered if one should attempt to analytically characterize the time domain signals associated with the torquer coil of the gyro. The complexity of the problem is of such magnitude as to justify relegating the determination of such signals to the experimental realm. Consequently, no attempt will be made in this thesis to analytically characterize the voltage and current waveforms associated with the torquer coil of the gyro. A brief treatment of these waveforms and others will be presented in a later chapter on experimental results.

## CHAPTER VIII

### ERROR ANALYSIS OF THE H-SWITCH AND PRECISION VOLTAGE REFERENCE CIRCUIT

A brief preliminary error analysis involving the H-switch was presented in Section C of Chapter II. Actuating errors and steady-state accuracy were obtained and discussed in Chapter V. This chapter will continue the error analysis of the TCG by investigating offset and drift errors associated with the H-switch and the PVR circuit. Rise- and fall-time inaccuracy and transient feed through currents will be briefly discussed. The results of investigating these errors will then be used to give a worst-case estimate of the overall accuracy of the TCG.

#### A. The H-Switch

A detailed description of the H-switch is given in Section E of Chapter III. The H-switch is included in the schematic of the TCG shown in Figure 3.1. A model of the H-switch for offset current error analysis is given in Figure 8.1. The main torquer current is shown in heavy lines. Offset currents are indicated by lighter, broken lines with arrows. The H-switch drive circuits are isolated from the torquer and switches Q5, Q6, Q8, and Q9 by insulated-gate FETS Q4A, Q4B, Q7A, and Q7B. There is negligible quiescent DC gate current present in the torque current. With reference to Figure 8.1, the gate leakage current of Q7A could contaminate the torquer current. However, according to manufacturer's data, this leakage current should be no greater than 10pA. When compared to



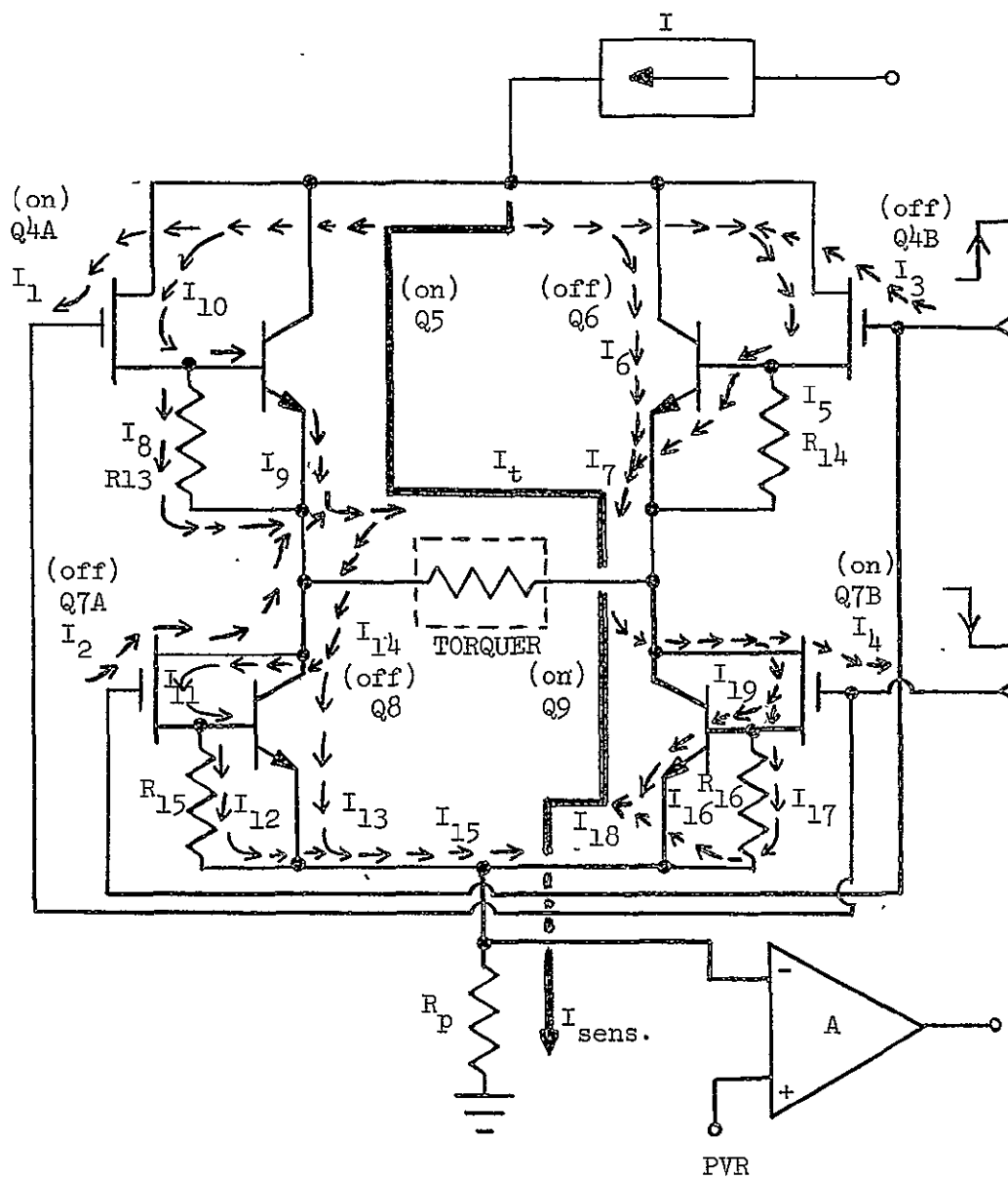


FIGURE 8.1

MODEL OF H-SWITCH FOR OFFSET CURRENT ERROR ANALYSIS

the low-level torquer current of 30mA, the leakage current represents only  $3.33 \times 10^{-4}$  ppm. For a torquer current of 1mA, the leakage current represents  $1 \times 10^{-2}$  ppm. The Kearfott Model 2544 gyro has a torquer scale factor of 0.57 deg/mA-sec.<sup>5</sup> For a 2.4 kHz interrogation rate, and the gyro pickoff assumed to be in a nulled position, the leakage current represents an approximate error in the movement of the gyro float of  $4.3 \times 10^{-9}$  arc-sec per torque pulse.

#### Transient Feedthrough Currents

Although the MOSFETS mentioned above do provide excellent DC isolation, they are somewhat susceptible to transient feedthrough currents. This occurs through the gate-source and gate-drain capacitances of the MOSFET. Good discussions of these parameters may be found in References 39 and 40.

Transient waveforms at the terminals of the composite field-effect-bipolar transistors in the H-switch were observed. The errors were small enough to make impractical a graphical analysis such as that reported by the author in Reference 4. The graphical analysis referred to was composed of the following steps: (1) photograph the transient current waveform at each terminal of the device in question; (2) enlarge and project this waveform upon a large scale grid made up of mm squares; (3) graphically obtain the area in ampere-seconds by counting the blocks; and, (4) comparing the areas to obtain a reasonable approximation of feedthrough currents.

A theoretical analysis of the transients in the H-switch is an almost insurmountable task. However, a brief argument will be presented

in an effort to obtain a worst-case approximation of transient feedthrough current errors. With reference to Figure 8.1, the main transient feedthrough will be  $I_1$ ,  $I_2$ ,  $I_3$ , and  $I_4$ . The problem is not simply one of feedthrough currents. Rather, the problem is to determine which transient feedthrough currents go through the torquer and are not sensed by the sampling resistor, or vice versa.

Consider first  $I_1$  and  $I_3$ . During a switching transient, one of these transient feedthrough currents enters the node at the top of the H-switch and the other leaves the node. Since the gate-source voltage changes on Q4A and Q4B are theoretically the same but of opposite polarity, and Q4A and Q4B are closely matched, one may assume  $I_1$  and  $I_3$  to be equal in value. If such is the case, then neither current contaminates the torque current and neither is sensed by the sampling resistor.  $I_1$  and  $I_3$  can thus be neglected because they cancel each other.

Next, consider  $I_2$  and  $I_4$ . Q7A is turning "off" as Q7B is turning "on". The gate-source voltage swings on Q7A and Q7B are theoretically the same, but are of opposite polarity. One may assume that  $I_2$  and  $I_4$  are equal in magnitude. However, in this case they do not enter and exit the same node. The torquer coil is located between the sources of Q7A and Q7B. Under these circumstances it is possible that part or all of  $I_2$  and  $I_3$  become a part of the torque current. With a 35V signal swing on the gates of the MOSFETS, the ampere-second area contributed by  $I_2$  or  $I_3$  to the total amp.-sec area of a torque pulse would at first appear significant. Suppose the gate-source swing of 35V is accomplished in 20ns. The well-known equation relating capacitance, the current through it, and the voltage change across it is

$$i_C = C \frac{dv}{dt} . \quad (8.1)$$

$$\int_0^{t_1} i_C dt = C \int_0^{V_1} dv . \quad (8.2)$$

The left side of Equation (8.2) gives the current-time area as a result of the voltage change on C from 0 to  $V_1$  in a time  $t$  from 0 to  $t_1$ . From the manufacturer's data sheet, the gate-source capacitance of the 3N190 MOSFET is approximately 2.5pF. Let  $\Delta i_{I_2}(\text{trans.})$  represent the area added to or subtracted from a normal torque pulse area by the transient feed-through current  $I_2$ . Then, substituting 2.5pF into Equation (8.2) gives

$$\Delta i_{I_2}(\text{trans.}) = \int_0^{t_1=20\text{ns}} i_C dt \approx 8.75 \times 10^{-11} \text{ amp.-sec.} \quad (8.3)$$

The error in the movement of the gyro float (for a Kearfott Model 2544 gyro) due to  $\Delta i_{I_2}(\text{trans.})$  is approximately  $1.8 \times 10^{-4}$  arc-sec. This error remains the same whether a limit cycle of 2.4 kHz or 10 kHz is used. The relative size of the error will change with the limit cycle frequency.

The worst-case contamination of the torque current will occur when the TCG is in the low-level torquing mode. Assume that the gyro is nulled and that the TCG is driving the gyro torquer with equal positive and negative area current pulses. Under such circumstances, and with a limit cycle of 2.4 kHz from the logic section, the time duration of either a positive or negative current pulse should be 208.33  $\mu\text{sec}$ . The low-torque

level is 30mA. Letting  $\Delta i_{t(\text{low})}$  represent the torque pulse area due to the low-level torque current under gyro nulled conditions,

$$\Delta i_{t(\text{low})} \equiv I_t(\text{low})\Delta t \approx 6.25 \times 10^{-6} \text{ amp.-sec.} \quad (8.4)$$

Now  $\Delta i_{I_2(\text{trans.})}$  can be compared to  $\Delta i_{t(\text{low})}$ .

$$\frac{\Delta i_{I_2(\text{trans.})}}{\Delta i_{t(\text{low})}} \approx 1.4 \times 10^{-5} = 14 \text{ ppm} . \quad (8.5)$$

If lower torquing levels were used, the value expressed in Equation (8.5) would increase proportionately. Assume the limit cycle frequency to be 2.4 kHz and the torque current level to be 1mA. Then,

$$\Delta i_{t(\text{low})} = 2.083 \times 10^{-7} \text{ amp.-sec.} \quad (8.6)$$

$\Delta i_{I_2(\text{trans.})}$  can be compared to  $\Delta i_{t(\text{low})}$  to give

$$\frac{\Delta i_{I_2(\text{trans.})}}{\Delta i_{t(\text{low})}} \approx 420 \text{ ppm} . \quad (8.7)$$

Now, assume the limit cycle frequency to be 10 kHz and the torque current level to be 1mA. Under these conditions,

$$\Delta i_{t(\text{low})} = 5.0 \times 10^{-8} \text{ amp.-sec.} , \quad (8.8)$$

and

$$\frac{\Delta i_{I_2(\text{trans.})}}{\Delta i_{t(\text{low})}} \approx 1750 \text{ ppm} . \quad (8.9)$$

The results obtained immediately above do not reflect the whole story and are much too pessimistic. A closer study of Figure 8.1 and the operating conditions of the H-switch indicate that the net effect of the transient feedthrough currents is two-fold: (1) they add torque pulse area to the leading edge of the torque current pulse; and (2) they subtract torque pulse area from the trailing edge of the torque current pulse. Since the H-switch is symmetrical and composed of well-matched devices, and since this is a binary system with positive and negative torquing during each limit cycle, the transient feedthrough effects should be compensating. Even if there is not complete compensation, a part of what remains will be sensed by the sampling resistor and corrected by the feedback mechanism of the TCG. In view of this, the errors due to transient feedthrough currents due to driving the H-switch can be neglected when compared to errors from other sources.

Another transient phenomenon occurs in the H-switch when the sampling resistors are switched. When switching from the low-torque level of 30mA to the high-torque level of 60mA, a negative spike of approximately 3.1 volts appears on the normal 6.2V DC level at the emitters of Q8 and Q9. When switching from the high level to the low-level of torque current, a positive spike appears at the emitters of Q8

and Q9. This positive spike attempts to rise 6.2 volts above the normal 6.2V DC level at that point, but is clamped at approximately 10V by the sampling resistor switching network. These transient pulses are eliminated as soon as corrective action can be taken by the feedback mechanism of the TCG. However, during the time they are present there are undoubtedly some undesirable transient feedthroughs in the H-switch. These transient feedthroughs are extremely difficult to observe, identify, and measure. Further, they are virtually impossible to calculate. All is not darkness, however, for two reasons. First, the sampling resistors are switched at a time when the torquer current is to change directions through the torquer coil. At some time during this interval of changing torquer current direction, one could look from the bottom of the H-switch up and see a bilateral circuit with each leg in a similar state to the other. At this particular time, none of the devices are full "on" or full "off". As a result, a transient voltage spike occurring at the emitters of Q8 and Q9 has a better opportunity to feedthrough both legs of the bilateral H-switch. Some compensating effects could be expected in this case.

Secondly, switching of the sampling resistors does not occur at a rapid rate. The logic section, which delivers torque commands to the TCG, is designed to generate a high scale factor command only 4 low torque-current pulses after the need was sensed. Once in the high scale factor mode, 2048 high torque-current pulses must be delivered before a low scale factor command is given by the logic. As long as the attitude changes of the vehicle on which the gyro is strapped are not too severe,

the low-torque mode is maintained and no switching of resistors occurs. Principally because of this, and because in-flight corrections are made, the cumulative error due to transient feedthrough errors resulting from switching sampling resistors should be relatively small. Consequently, they will be neglected.

#### Rise- and Fall-Time Inaccuracy

Ideally the current waveform driving the torquer would be one with vertical edges, making equal positive and negative excursions about the zero axis at a 2.4 kHz rate, and width modulated so as to null the gyro error signal. Since the system is a binary one, both positive and negative torque pulses must be applied on a continuous basis.

In reality, the edges of the current pulses driving the gyro are not vertical. Rather, they exhibit characteristics associated with finite rise- and fall-times. Using a Kearfott 2544 gyro, for example, the observed low-torque rise- and fall-times for the current pulse through the torquer were 70 nsec and 90 nsec, respectively. Torque pulse area is lost on the leading edges of the current pulses, and torque pulse area is gained on the trailing edges of the current pulses. With unequal rise- and fall-times, the areas gained and lost in a given positive (or negative) torque pulse will be unequal. As mentioned earlier, there must be positive and negative torque pulses applied on a continuous basis. With well-matched devices in the H-switch, the rise- or fall-time variations which would decrease negative torque area would also decrease positive torque area as well. Hence, there is effectively an inherent compensation in the H-switch. The overall net torque pulse area should experience only a very small resultant change.



An analytical analysis of the unequal rise- and fall-time errors associated with the torque current waveform is much too complicated to be undertaken here. In order to circumvent this difficulty and obtain a reasonable approximation of the error, a graphical technique was employed. A photograph of the torque current waveform at a torquing level of 30 mA and a limit cycle of 2.4 kHz was taken. The photograph was projected onto a grid of millimeter squares at a distance appropriate to enlarge the oscilloscope graticule to a 80 cm  $\times$  100 cm size. The enlarged current waveform was traced on the grid along with a sketch of the ideal current waveform. By counting the mm squares, the current-time areas gained and lost by the finite rise- and fall-times of the torquer current were obtained. The excess or deficiency of area gained or lost over one interrogation period is the error of concern. The current-time area in the error due to unequal rise- and fall-times of the torque current pulse can be approximated as

$$\Delta i(t_r \neq t_f) \approx 4.7 \times 10^{-10} \text{ amp.-sec.} \quad (8.10)$$

per interrogation period. For the Kearfott Model 2544 gyro, this error corresponds to a net error in the gyro float movement of approximately  $9.6 \times 10^{-4}$  arc-sec.  $\Delta i(t_r \neq t_f)$  may be compared to the current-time area in an ideal current pulse to obtain the relative error. Assume the gyro float to be in a nulled position, the limit cycle frequency to be 2.4 kHz, and  $I_t(\text{low})$  to be 30 mA. Under these conditions,

$$\left. \frac{\Delta i(t_r \neq t_f)}{\Delta i_t(\text{low})} \right| \approx 75 \text{ ppm} . \quad (8.11)$$

L.C.F. = 2.4kHz

For the same conditions, but with a limit cycle frequency of 10 kHz, the relative error becomes

$$\left. \frac{\Delta i(t_r \neq t_f)}{\Delta i_t(\text{low})} \right| \approx 313 \text{ ppm} . \quad (8.12)$$

L.C.F. = 10kHz

The value for  $\Delta i(t_r \neq t_f)$  will of course be different for different levels of torquing current. The finite rise- and fall-times of the torque current waveform appear on the grid mentioned above as nonlinear curves. The error in current-time area due to unequal rise- and fall-times of the torque current pulse is then a nonlinear phenomenon. Larger amplitudes than 30 mA of torque current result in longer rise- and fall-times. The nonlinear curves of the leading and trailing edges of the torque current pulse cover more distance. Hence, the relative areas gained or lost are increased. The error in current-time area appears to increase at a rate more rapid than it would if it were a linear function of current amplitude. The inverse of the argument above holds for smaller current amplitudes than 30 mA of torquer current. The current-time area of an ideal torque current pulse, with the limit cycle frequency held constant, is a linear function of the amplitude of current pulse. Hence, the ratio of  $\Delta i(t_r \neq t_f)$  to  $\Delta i_t(\text{low})$  should be greater

than the value given in Equation (8.11) when  $I_t$  is greater than 30 mA and the limit cycle frequency is 2.4 kHz. The ratio should be smaller than 75 ppm when  $I_t$  is less than 30 mA. For a given torque current level, the ratio of  $\Delta i(t_r \neq t_f)$  to  $\Delta i_t(\text{low})$  increases linearly for limit cycle frequencies above 2.4 kHz. The ratio decreases linearly for limit cycle frequencies below 2.4 kHz.

#### Offset and Drift Errors in the H-Switch

The assumption is made in Figure 8.1 that the composite transistor combinations (Q4A, Q5) and Q7B, Q9) are "on" and (Q4B, Q6) and (Q7A, Q8) are "off". Leakages in the "off" devices will cause a DC offset leakage current which did not pass through the torquer to be sensed by the sampling resistor. This ultimately appears to the system computer as a torque pulse area which was applied, but really wasn't. Obviously, high quality devices must be used in the H-switch to maintain low DC offset leakage if for no other reason.

Referring to Figure 8.1, the DC offset leakage is due principally to  $I_7$  and  $I_{15}$ . Using  $I_{\text{sens}}$  for the current sensed by the sampling resistor,  $R_p$ , one can write

$$I_{\text{sens.}} \approx I_{\text{torque}} + I_7 + I_{15} . \quad (8.13)$$

Manufacturer's data on the 3N190 MOSFET indicates a maximum leakage current of 400 pA. Data sheets on the SDT 6103 bipolars do not give any leakage specifications. 10 nA will be assumed as a reasonable maximum offset current for the SDT 6103 device. For lack of data, 10% of the

leakage current per degree Celsius will be assumed for the temperature coefficient for both the MOSFETS and bipolars. This amounts to 1 nA/°C for the SDT 6103 and 40 pA/°C for the 3N190.

Equation (8.6) indicates that the error in the current sensed is  $I_7 + I_{15}$ . The error of these terms in comparison to the low-scale torque current,  $I_t(\text{low})$  is

$$\text{Static Error} = \frac{I_7 + I_{15}}{I_t(\text{low})} \approx \frac{20.8 \times 10^{-9}}{30 \times 10^{-3}} \approx 0.7 \text{ ppm} . \quad (8.14)$$

The worst-case drift error is

$$\text{Drift Error} = \frac{2.08 \times 10^{-9}}{(30 \times 10^{-3})^\circ\text{C}} \approx 0.07 \text{ ppm/}^\circ\text{C} . \quad (8.15)$$

### The PVR Circuit

A full schematic of the PVR circuit is shown in Figure 3.1 as a part of the TCG circuit. A simplified model of the PVR and associated circuitry for use in drift error analysis is given in Figure 8.2. The terms indicated in Figure 8.2 are those needed for drift error analysis and are defined as following:

- $I_t$  - the precision current applied to the gyro torquer,  
and which is equal to  $V_{\text{Ref}}/R_p$ ;
- $V_{\text{Ref}}$  - the precision Zener diode reference voltage;
- $R_p$  - the precision sampling resistor which monitors  
the torque current;
- $I_z$  - the Zener current;

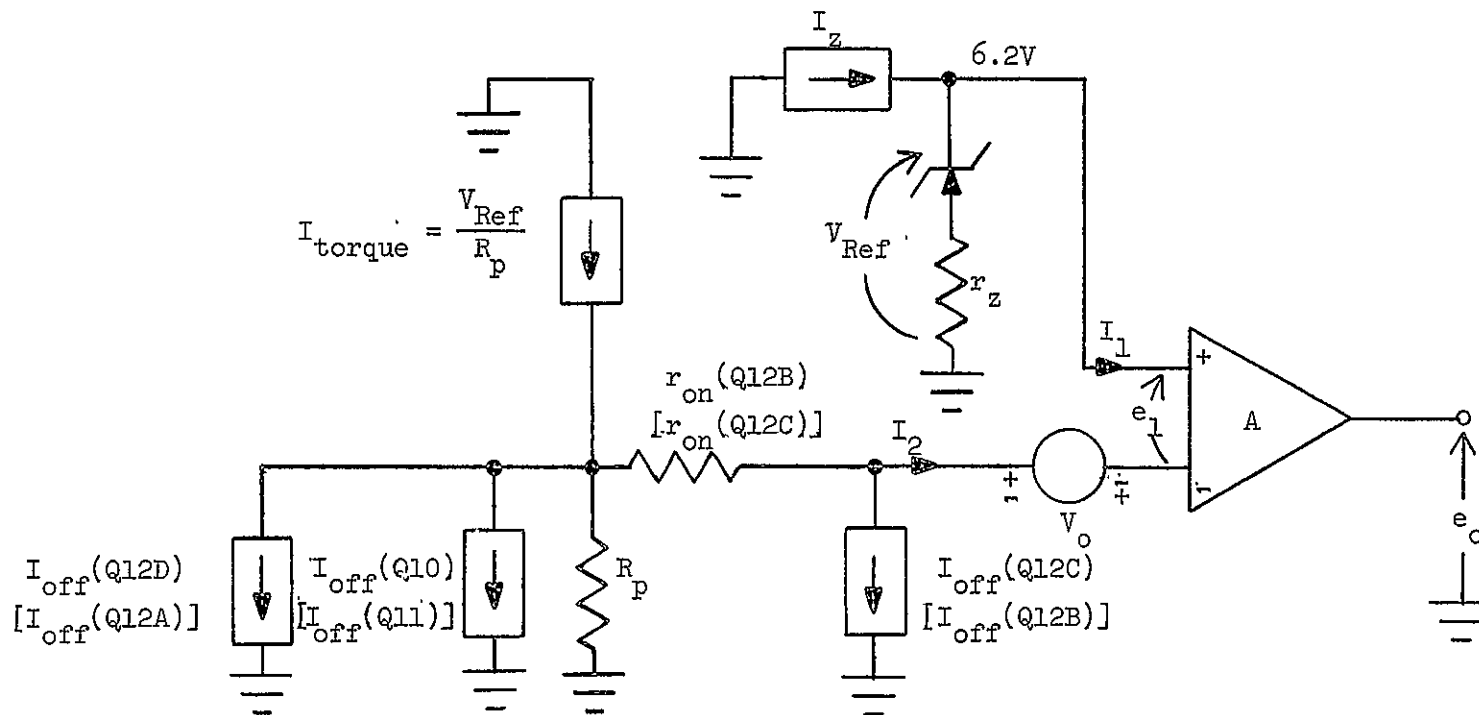


FIGURE 8.2

A SIMPLIFIED MODEL OF THE PVR AND ASSOCIATED CIRCUITRY  
FOR USE IN DRIFT ERROR ANALYSIS

- $I_1, I_2$  - input bias currents for the op.-amp.;  
 $V_o$  - the op. amp. offset voltage;  
 $r_{on}$  - the channel resistance of the "on" FET switches;  
 $r_z$  - the dynamic resistance of the Zener diode;  
 $e_1$  - the error signal voltage in the feedback circuit;  
 $I_{off}$  - the leakage current of an "off" FET or bipolar transistor switch.

The transistor numbers used in Figure 8.2 refer to those used in Figure 3.1. The topological form of the circuit in Figure 8.2 is the same whether the system is in the high- or low-torque state. Parameters shown in brackets apply to the low-scale torquing state, and unbracketed values indicate the high-scale torquing state.

An equation for the error signal,  $e_1$ , can be obtained from an analysis of Figure 8.2.

$$\begin{aligned}
 e_1 = & \pm V_o + I_2 [R_p + r_{on} (Q12B)] - I_1 r_z \\
 & + (V_{Ref} - R_p I_t) + R_p [I_{off}(Q12D) + I_{off} (Q10)] \\
 & + [R_p + r_{on} (Q12B)] I_{off}(Q12C) \quad . \quad (8.16)
 \end{aligned}$$

Drift of the error signal  $e_1$  with temperature can be estimated by a first-order linearization. This can be done by substituting values for the appropriate changes from data sheets into the expression for  $\Delta e_1 / \Delta T$  computed from Equation (8.16). Table 8.1 gives the data on drifts as

TABLE 8.1

DRIFT DATA USED FOR DRIFT  
ERROR ANALYSIS OF THE PVR

$\frac{\Delta V_o}{\Delta T} = \pm 0.5 \mu V/^{\circ}C$	$I_{off}(Q12) = 200 \text{ pA}$
$I_1 = 105 \text{ nA(max)}$	$\frac{\Delta I_{off}(Q12)}{\Delta T} = 20 \text{ pA}$
$\frac{\Delta I_1}{\Delta T} = 200 \text{ pA}/^{\circ}C$	$I_{off}(Q10, Q11) = 10 \text{ nA}$
$I_2 = 95 \text{ nA (max)}$	$\frac{\Delta I_{off}(Q10, Q11)}{\Delta T} = 1 \text{ nA}/^{\circ}C$
$\frac{\Delta I_2}{\Delta T} = 200 \text{ pA}/^{\circ}C$	$r_z = 10 \text{ ohms}$
$I_1 - I_2 = 10 \text{ nA(max)}$	$\frac{\Delta R_p}{\Delta T} = \pm 3 \text{ ppm}/^{\circ}C$
$V_{Ref} = 6.2V$	$R_p(\text{low-scale}) = 206.7 \text{ ohms}$
$\frac{\Delta V_{Ref}}{\Delta T} = \pm 31 \mu V/^{\circ}C$	$R_p(\text{high-scale}) = 103.3 \text{ ohms}$
$r_{on} = 75 \text{ ohms}$	
$\frac{\Delta r_{on}}{\Delta T} = 0.15 \text{ ohm}/^{\circ}C$	

reported by manufacturers' data sheets, or as reasonable estimates when not reported.

Neglecting insignificant terms, the normalized change in  $e_1$  with temperature can be approximated as

$$\left( \frac{1}{V_{\text{Ref}}} \right) \frac{\Delta e_1}{\Delta T} \approx \frac{1}{V_{\text{Ref}}} \left[ \pm \frac{\Delta V_o}{\Delta T} \pm \frac{\Delta V_{\text{Ref}}}{\Delta T} - \frac{V_{\text{Ref}}}{R_p} \frac{\Delta R_p}{\Delta T} \right] . \quad (8.17)$$

Substituting appropriate values from Table 8.1 into Equation (8.17) gives

$$\frac{1}{V_{\text{Ref}}} \frac{\Delta e_1}{\Delta T} \text{ (low-torque case) } \leq 3.6 \text{ ppm/}^\circ\text{C} , \quad (8.18)$$

and

$$\frac{1}{V_{\text{Ref}}} \frac{\Delta e_1}{\Delta T} \text{ (high-torque case) } \leq 2.2 \text{ ppm/}^\circ\text{C} . \quad (8.19)$$

An estimate of long-term drift can also be made.  $\Delta V_o/\Delta t$  is given for the op. amp. as 10  $\mu\text{V/month}$ .  $\Delta V_{\text{Ref}}/\Delta t$  is specified by data sheets as better than 100 ppm/1000 hr. The sampling resistor should be chosen so as to have a  $\Delta R_p/\Delta t$  of at least as low as 12 ppm/1000 hr. Substituting these values into the expression for the normalized error signal change with time gives

$$\frac{1}{V_{\text{Ref}}} \frac{\Delta e_1}{\Delta t} \leq 96 \text{ ppm/month} . \quad (8.20)$$



Obviously this value is due principally to the drift of the 1N829A Zener reference diode. If lower drift is required, a MZ605 precision reference diode with less than 5 ppm/1000 hr. can be used in place of the 1N829A diode. In that case, a long-term drift of 6.6 ppm/month could be expected.

A worst-case estimate of the overall accuracy of the TCG can be made by adding the errors associated with the PVR, with sensed current, and with unequal rise- and fall-times.

$$\begin{aligned} \text{Overall Accuracy (worst-case analysis)} \approx \\ & \text{error (PVR)} + \text{error (Sensed current)} + \\ & \text{error (rise- and fall-times)} \end{aligned} \quad (8.21)$$

Substituting values obtained earlier in this chapter into Equation (8.21) gives the following for the low-torque mode:

$$\begin{aligned} \text{Overall Accuracy (worst-case analysis)} \leq \\ & (3.6 \text{ ppm}/^{\circ}\text{C and } 96 \text{ ppm/month}) + \\ & (0.7 \text{ ppm and } 0.07 \text{ ppm}/^{\circ}\text{C}) + \\ & (< 75 \text{ ppm}). \end{aligned} \quad (8.22)$$

## CHAPTER IX

### NOISE CONSIDERATIONS FOR THE TORQUE

#### CURRENT GENERATOR

##### A. General Comments

Devices classified as transducers, detectors, and sensors are basic to the instrumentation and control fields. These devices are analogous to the ears, eyes, and other senses of the human body. They sense and translate physical world properties into electrical signals. The level of electrical noise generated in the sensor and its associated electronic system is often of great concern to the design engineer.

The TCG incorporates a type of sensor system. The torquing current is sensed by one of two sampling (or sensing) resistors. The voltage developed across the sampling resistor is compared to a precision voltage reference by the AD504M operational amplifier (see Figure 3.1). Input offset voltage, input currents, and their drifts constitute DC input error signals. Equivalent input noise voltage and currents represent AC input error signals in a differential stage, such as the input of the op. amp. The signal sensitivity of the amplifier system is limited by the combined effects of input noise voltage and currents. Any amplified signal must be of sufficient magnitude to be detectable over the inherent noise level of the amplifier. Whenever possible, circuit conditions should be adjusted for a maximum signal-to-noise ratio in order to optimize noise performance.

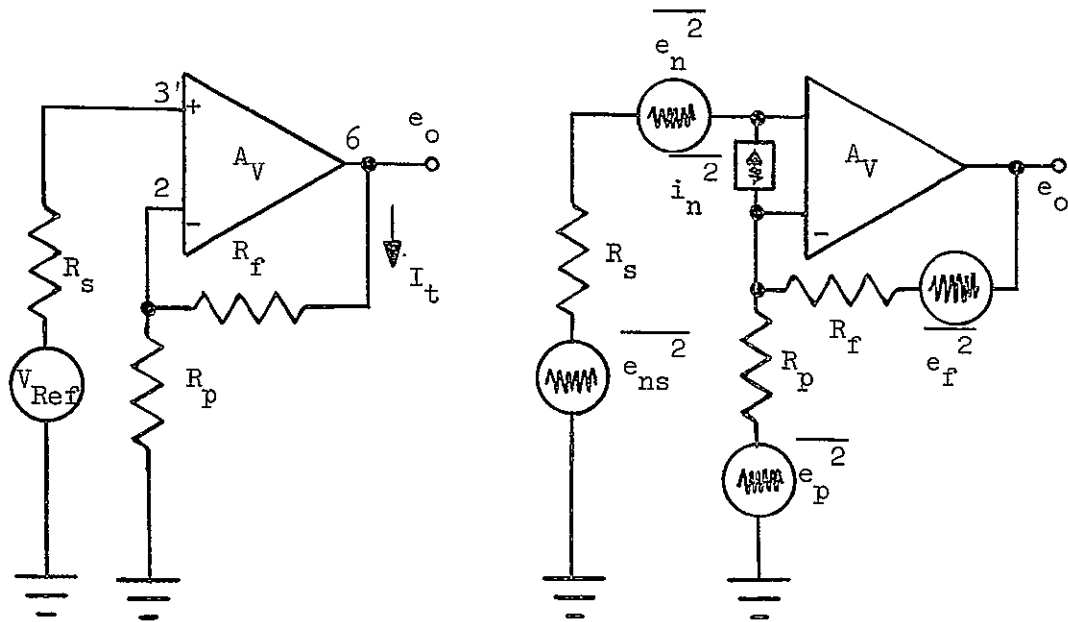
Much of the theory on noise is statistical and quite complicated. In addition to being highly mathematical, many treatments on noise are not readily applicable to circuits involving operational amplifiers. In this chapter, derivations will be avoided in hope of a simple noise analysis of the TCG. Noise mechanisms will be assumed familiar to those who read this thesis and will not be discussed. The literature contains many sources with discussions on noise mechanisms. Among these are References 42 through 48 which the author found helpful. A practical approach outlined in Reference 41 will be combined with conventional methods to predict the "total RMS noise" of the TCG.

Noise figures of merit will not be discussed in this chapter except to briefly state which parameter will be most useful in characterizing the TCG. The AD504M op. amp. functions to sense and amplify differences in voltages that may appear across the sampling resistor and the precision reference diode. In view of this, the most logical parameter to obtain would be the equivalent input noise voltage of the system. This will indicate how small a differential signal can be sensed and processed.

The noise analysis of the TCG will now be undertaken. Noise terminology and modeling which may be necessary will be discussed when needed.

#### B. Noise Analysis of the TCG

As detailed in Chapter V, the TCG can be represented as a feedback circuit illustrated in Figure 9.1 (a). The load, i.e. the torquer



(a) Feedback representation of the TCG.

(b) Feedback circuit with noise sources.

FIGURE 9.1

FEEDBACK CIRCUIT REPRESENTATIONS OF THE  
TCG FOR USE IN NOISE ANALYSIS

coil of the gyro, is floating and is contained in  $R_f$ . Standing at the output of the amplifier block, the impedance seen looking toward the load appears resistive over the frequency range of interest. However, within the resistor labeled  $R_f$  there are six composite field-effect-bipolar transistors as well as the torquer coil plus its compensation. At any one time under steady-state conditions, three of the composite transistors will be "on" and three will be "off". Ideally, one would like to obtain the noise contribution of each of these components grouped in  $R_f$  and combine these noise sources into one mean-square equivalent noise voltage generator,  $\overline{e_f^2}$ .

Between the junction of  $R_p$  and  $R_f$  and pin 2 of the amplifier block are two MOSFET's. At any one time under steady-state conditions, one transistor is "on" and one is "off". The noise contribution of these devices can be combined in the mean-square equivalent noise voltage generator for  $R_p$ ,  $\overline{e_p^2}$ .

$R_s$  in Figure 9.1 (a) represents any resistance presented by the PVR to the input of the amplifier block. The noise contributions of the IN829A Zener reference diode, D4, R3, and Q16 (see Figure 3.1) can all be combined into one mean-square equivalent noise voltage generator,  $\overline{e_{ns}^2}$ .

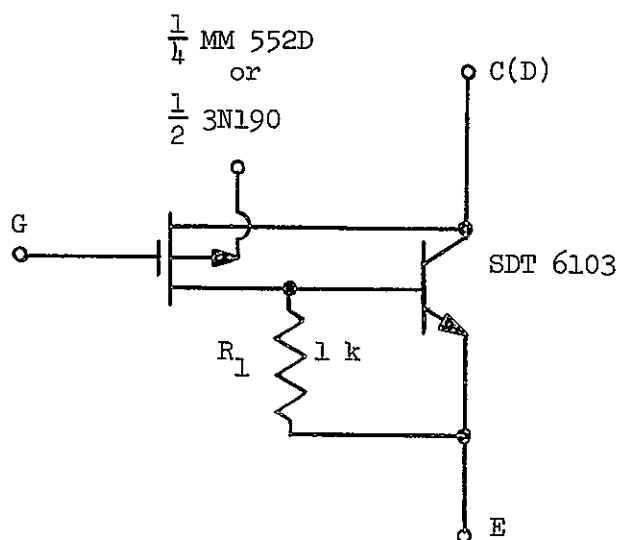
The amplifier block  $A_v$  in Figure 9.1 (a) represents the TCG loop from the input of IC1 to the emitter of Q3. Noise sources throughout this portion of the circuit will need to be reflected to the input of the op. amp. as  $\overline{e_n^2}$  and  $\overline{i_n^2}$ .

With all the conditions in the immediately above discussion met, the TCG loop can be represented as illustrated in Figure 9.1 (b). The equivalent input noise of this system is<sup>42</sup>

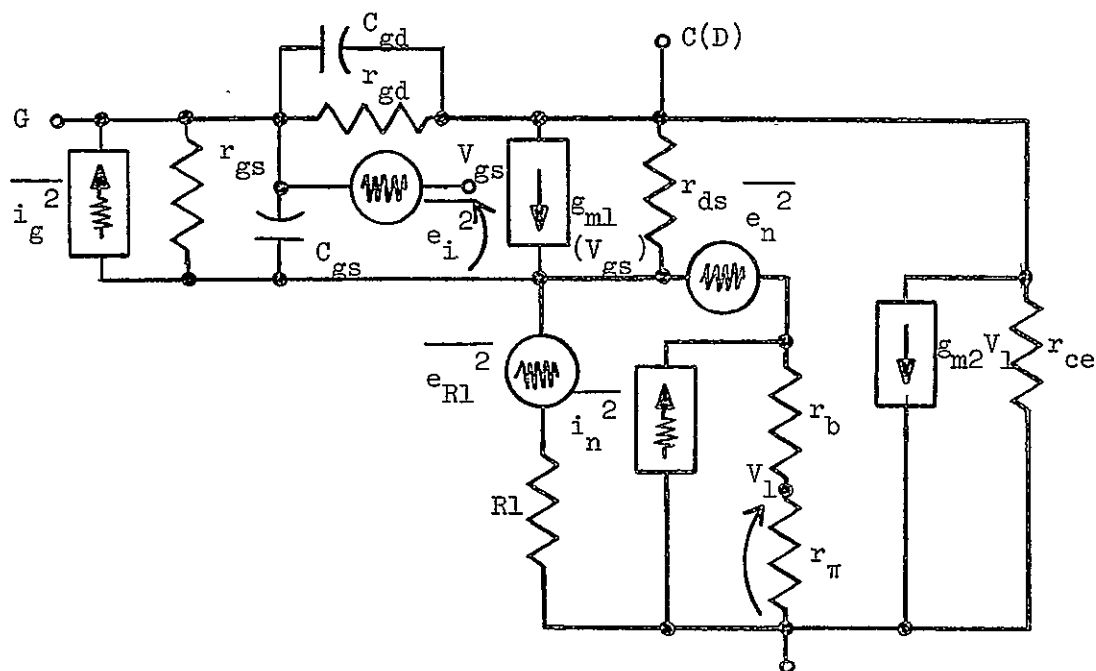
$$\begin{aligned} \overline{e_{ni}^2} \approx & \overline{e_{ns}^2} + \overline{e_n^2} + \overline{i_n^2} \left( R_s + \frac{R_p R_f}{R_p + R_f} \right)^2 \\ & + \overline{e_p^2} \left( \frac{R_f}{R_p + R_f} \right)^2 + \overline{e_f^2} \left( \frac{R_p}{R_p + R_f} \right)^2 . \end{aligned} \quad (9.1)$$

The  $\overline{e_f^2}$  noise generator included in Equation (9.1) will be considered first. An earlier discussion outlined the components contained in the  $R_f$  representation in Figure 9.1. Figure 9.2 (a) indicates the general form of the composite FET-bipolar transistors used in the H-switch and sampling resistor switching network. Figure 9.2 (b) is a simplified noise model, with noise referred to the inputs of the respective devices. Noise models of bipolar transistors and FET's may be found in noise literature, or in such references as References 42 and 49 in this thesis.

The method of attack will be as follows: determine the noise voltages and currents at the input of the MOSFET; reflect these contributions to the base of the bipolar; determine  $\overline{e_n^2}$  and  $\overline{i_n^2}$  for the bipolar; reflect the composite noise of the two devices from the base of the bipolar to the emitter. Then, the noise contributions of all the composite transistors ( $\overline{e_{f1}^2}$ ,  $\overline{e_{f2}^2}$ , etc.) can be combined. This result can be combined with noise contributions of the torquer and its compensation network to give the desired mean-square equivalent noise voltage generator



(a) General form of a composite FET-bipolar transistor used in the H-switch.



(b) Noise model for the composite FET-bipolar transistor in (a).

FIGURE 9.2

REPRESENTATIONS OF A COMPOSITE FET-BIPOLAR TRANSISTOR  
FOR USE IN NOISE ANALYSIS

$\overline{e_f^2}$ . The spectrum of frequency will be divided into narrow "spots" or intervals,  $\Delta f_1, \Delta f_2$ , etc., so that  $\overline{e_n^2}$  or  $\overline{i_n^2}$  may be considered either constant or to have constant slope (as in 1/f noise in low-frequency regions). Then an incremental approximation may be used to evaluate the rms noise,  $\overline{e_n}$ . The rms noise in the total interval to be computed is the root-sum-of-the-squares of the noise in the incremental intervals, since it can be assumed that each noise source is relatively uncorrelated with the others. This may be expressed as

$$\overline{e_n} = \sqrt{\overline{e_{n1}^2} \Delta f_1 + \overline{e_{n2}^2} \Delta f_2 + \dots} \quad (9.2)$$

The noise sources in the MOSFET may be calculated by the following equations:

$$\overline{i_g^2} = 2q I_g + \frac{4}{3} kTR_n (\omega C_{gs})^2 ; \quad (9.3)$$

$$\overline{i_d^2} = 4 kT (Kg_m) ; \quad (9.4)$$

$$\overline{e_i^2} = 4 kTR_n (1 + f_b/f\alpha) ; \quad (9.5)$$

and

$$R_n = K/g_m , \quad (9.6)$$



where  $K$  varies from 1 to 2.5 for a MOSFET. In Equation (9.5),  $f_b$  is the break frequency between  $1/f$  noise and white noise, and  $\alpha = 1$  for  $1/f$  noise. The  $f_b/f$  term in Equation (9.5) accounts for low-frequency noise. Das and Moore<sup>50</sup> give an expression for  $\overline{i_d^2}$  in the low-frequency range in terms of terminal voltages and power dissipation. The expression, though attractive, is in the form of a proportionality and the proportionality constant is not given. Since no exact data on the 3N190 or MM552D MOSFET's is given, an  $f_b$  of 10 kHz and  $K = 1$  will be assumed. These values seem reasonable in light of the following: (1) Ronen<sup>48</sup> shows that when clean thin oxides are used, conventional low-threshold p-MOSFET's demonstrate low-noise operation, low cross-over frequencies of less than 10 kHz, and high uniformity of results; and (2) the observation has been made that devices with exceptionally low gate leakage current ( $I_{GSS}$ ) have low  $1/f$  noise.<sup>42</sup> The 3N190 MOSFET's are specified by the manufacturer to have an  $I_{GSS}$  of 10 pA maximum. The MM552D is specified to have a typical  $I_{GSS}$  of 20 pA.

The values to be used for  $g_m$  in the cases of the 3N190 or MM552D MOSFET's is not clearly defined. Since the devices will be operated in or near the ohmic region, minimum specified values of  $g_m$  will be used. Thus, 1200  $\mu$ mhos will be used for each type of MOSFET. A  $C_{gs}$  of 3 pF will be used for each of the devices.

The mean-square noise generators  $\overline{e_n^2}$  and  $\overline{i_n^2}$  in Figure 9.2 can be evaluated by the following approximations:

$$\overline{e_n^2} \approx 4 kT \left( r_b + \frac{r_e}{2} \right) ; \quad (9.7)$$

and

$$\overline{i_n^2} = 2 q I_B \left(1 + \frac{f_b}{f}\right) . \quad (9.8)$$

$f_b$  in Equation (9.16) is the break frequency between  $1/f$  noise and white noise for the bipolar transistor. Equations (9.7) and (9.8) are simplifications from more complex equations by assuming  $\beta_o \gg 1$ ,  $r_\pi \gg r_b$ , and  $I_B \gg I_{CBO}$ , where  $r_b$  is the base resistance. The term  $\overline{e_{R1}^2}$  in Figure 9.2 is the thermal noise generator for  $R1$ . This noise voltage contribution will also be reflected to the emitter of the bipolar transistor.

The Kearfott Model 2544 gyro torquer coil has a DC resistance of approximately 71.7 ohms. The compensation resistor  $R_{tc}$  is also 71.7 ohms. The noise contribution of this effective resistance is to be included in the  $\overline{e_f^2}$  mean-square noise generator.

The necessary equations for determining  $\overline{e_f^2}$  are now available. The details of the calculations will not be given in order to conserve space. Also, the results of the calculations will be reserved until the means of deriving the other equivalent mean-square noise generators in Equation (9.1) have been discussed. Then, a table listing values of these noise generators for specified frequency bands will be given. In this way, all the pertinent information will be in one brief space for study and comparison.

The  $\overline{e_p^2}$  generator in Equation (9.1) will be considered next. The MOSFET's between the sampling resistor and the input of the op. amp. can be treated with Equations (9.3) through (9.6). This contribution can be combined by circuit analysis with  $\overline{e_{R_{pl}}^2} = 4 kTR_{pl}$  to give  $\overline{e_p^2}$ .

The  $\overline{e_{ns}^2}$  mean-square noise generator in Equation (9.1) consists of the noise contributions of Q16 (a JFET), D1, D4, and R3. Equations (9.3) through (9.6) can be used with the JFET.  $K$  is taken as 2/3, and other parameters are available in the manufacturer's data book.

D1 is a Zener reference diode. A Zener diode generates noise when it is biased in the normal reverse-bias breakdown region. The internal resistance associated with the device causes a small part of this noise. A larger part of Zener noise is a result of the Zener breakdown phenomenon. This noise mechanism is often called microplasma noise. Generally, this microplasma noise is considered "white" noise with equal amplitude for all frequencies from zero Hertz to approximately 200 kHz. The higher frequency components of the noise may be partially eliminated by using a small shunting capacitor (C3 in Figure 3.1, serves this purpose). The size of the capacitor which would be required to eliminate the lower frequency components of the noise would degrade the regulation properties of the Zener diode. Hence, the lower frequency noise must be tolerated.

A plot of the distribution of maximum generated noise versus center frequency for the 1N829A diode is included in one manufacturer's data sheets (The Semiconductor Data Library, Motorola Semiconductor Products, Inc., First Edition, Vol. 1). The curve was obtained with a current of 7.5 mA in the diode and with a measuring setup having a 500 Hz bandwidth. The value of maximum generated noise in a 500 Hz bandwidth was less than  $1 \mu V_{rms}$  over a center frequency range of 10 kHz to 1 GHz. Assuming a  $1 \mu V_{rms}$  maximum noise in a 500 Hz bandwidth, a value of  $45 nV_{rms}/\sqrt{Hz}$  is thus obtained for the noise generator representation of D1.

The TCG has a closed-loop bandwidth of approximately 200 kHz. The noise generated by D1 begins to experience attenuation before 200 kHz because of the time constant associated with the shunting capacitance C3 and the dynamic impedance of the diode. The break frequency corresponding to that time constant is approximately 159 kHz. To obtain a reasonable worst-case condition, the  $45 \text{ nV}_{\text{rms}}/\sqrt{\text{Hz}}$  value for the maximum generated noise for D1 will be assumed constant from zero Hertz to 200 kHz.

D4 is a forward-biased PN junction diode. Two noise current generators are important for D4 in the frequency range associated with the TCG operation. One is shot noise, and can be represented by

$$\overline{i_{(D4)S}^2} = 2 q I_D . \quad (9.10)$$

The other is low-frequency noise current, and it can be represented by<sup>42</sup>

$$\overline{i_{(D4)F}^2} = \frac{K I_D}{f} = \frac{2q F_L I_D}{f} , \quad (9.11)$$

where  $f_L$  is a constant having values from 3.7 kHz to 7 MHz. While  $f_L$  does not match the corner frequency, there is gross correlation between  $f_L$  and the low-frequency noise corner. Hence,  $f_L$  is used to represent the low-frequency noise corner frequency. In this application,  $f_L$  is chosen as 10 kHz.

R3 is typically 25 ohms, and exhibits thermal noise. The noise contribution of R3 is

$$\overline{e_{R3}^2} = 4 kT(R3) \Delta f \quad (9.12)$$

referred to pin 3 of IC1.

Consider the noise generators  $\overline{e_n^2}$  and  $\overline{i_n^2}$  which appear in Equation (9.1). These terms must contain the noise voltage and noise current contributions of the op. amp. and the circuit from the output of the op. amp. to the emitter of Q3. Many texts, such as Reference 42, contain the proper models and equations for calculating  $\overline{e_n^2}$  and  $\overline{i_n^2}$  for the Darlington pair and the differential amplifier. These are referred to the input of the op. amp. by using the proper gain expressions.

Curves are available from the manufacturer for  $\overline{e_n}$  and  $\overline{i_n}$  of the op. amp. over a frequency range of 1 Hz to 20 kHz. One can extrapolate these curves back to 0.1 Hz with reasonable accuracy. The curves will be assumed flat from 20 kHz to 200 kHz.

Before giving the table containing the mean-square noise sources used in Equation (9.1), a note should be made concerning the contribution of "pink noise" (a generic term applied to ideal 1/f noise). Pink noise contributes equal increments of rms noise over each octave or each decade of the spectrum. Each increment will be 1.52 K per decade, or 0.83 K per octave, where K is equal to the value of  $\overline{e_n}$  or  $\overline{i_n}$  at 1 Hz.<sup>41</sup>

Table 9.1 gives values for the contributions of the various noise generators appearing in Equation (9.1) over specified frequency bands. These values can be substituted into Equation (9.1) to yield  $\overline{e_{ni}^2}$  (and consequently  $\overline{e_{ni}}$ ) for each frequency interval. These results are given in Table 9.2.

TABLE 9.1  
CONTRIBUTIONS OF THE NOISE TERMS IN EQUATION (9.1) AND FIGURE 9.1  
FOR THE INDICATED FREQUENCY INTERVALS, AND FOR A TORQUE  
CURRENT OF 30 mA

$\Delta f$ (Hz)	$\overline{e_f^2}$ ( $V^2$ )	$\overline{e_p^2}$ ( $V^2$ )	$\overline{e_{ns}^2}$ ( $V^2$ )	$\overline{e_n^2}$ ( $V^2$ )	$\overline{i_n^2}$ ( $A^2$ )
0.1-10	$2.18 \times 10^{-12}$	$6.91 \times 10^{-13}$	$1.69 \times 10^{-13}$	$4.16 \times 10^{-15}$	$1.16 \times 10^{-22}$
10-100	$1.10 \times 10^{-12}$	$3.47 \times 10^{-13}$	$2.57 \times 10^{-13}$	$7.29 \times 10^{-15}$	$5.78 \times 10^{-23}$
100-1k	$1.18 \times 10^{-12}$	$3.59 \times 10^{-13}$	$1.90 \times 10^{-12}$	$7.31 \times 10^{-14}$	$5.78 \times 10^{-23}$
1k-10k	$2.00 \times 10^{-12}$	$5.13 \times 10^{-13}$	$1.83 \times 10^{-11}$	$7.74 \times 10^{-13}$	$3.60 \times 10^{-22}$
10k-200k	$1.93 \times 10^{-11}$	$3.54 \times 10^{-12}$	$3.85 \times 10^{-10}$	$1.59 \times 10^{-11}$	$1.71 \times 10^{-20}$

TABLE 9.2

 $\overline{e_{ni}}$  FOR THE INDICATED FREQUENCY INTERVALS

$\Delta f$ (Hz)	$\overline{e_{ni}}$ ( $v_{RMS}$ )
0.1-10	$1.12 \times 10^{-6}$
10-100	$9.03 \times 10^{-7}$
100-1k	$1.60 \times 10^{-6}$
1k-10k	$4.48 \times 10^{-6}$
10k-200k	$2.03 \times 10^{-5}$

The entries in Table 9.2 can then be substituted into

$$\overline{e_{ni}} = \sqrt{\overline{e_{ni1}}^2 + \overline{e_{ni2}}^2 + \dots} \quad (9.13)$$

to yield the total rms input noise in the 0.1 Hz to 200 kHz interval.

The result of this operation is (for a torque current of 30 mA)

$$\overline{e_{ni}} (0.1 \text{ Hz to } 200 \text{ kHz}) \approx 20.9 \mu\text{V}_{\text{rms}} \quad (9.14)$$

It is apparent from Table 9.1 that the significant noise contribution is due to the Zener reference diode (the  $\overline{e_{ns}}^2$  term), and thus the  $\overline{e_{ni}}$  value of Equation (9.14) is not strongly dependent on the torque current value.

A further note should be made concerning the input noise to IC1 of the TCG. The noise consists of frequency components that are random in both amplitude and phase. Although the instantaneous amplitude or phase cannot be predicted, the long-term mean of the noise signal should be zero. Hence, over relatively long term intervals, the effect of the noise on the movement of the gyro float should be negligible.



## CHAPTER X

### VERSATILITY OF THE TORQUE CURRENT

#### GENERATOR

The torque current generator illustrated in Figure 3.1 represents the author's idea of the required circuit at the point in time of its inception. Obviously, needs change with time and applications. One of the design goals enumerated for the TCG in Chapter II was versatility. The TCG circuit, as illustrated in Figure 3.1, presents itself as a circuit which can be modified in numerous ways without changing the basic design features of the circuit.

The current range capability of the TCG (as it exists in Figure 3.1) will be discussed in this chapter. In addition, many possible modifications of the TCG will be presented. Although not exhaustive in number, the possible modifications given will illustrate the versatility of the TCG.

#### A. Current Range Capability of the TCG

The TCG, as it appears in Figure 3.1, was experimentally run with two different gyros at low- and high-torquing levels of 30 mA and 60 mA, respectively. A knowledge of the upper and lower level torquing limits would be useful information. These limits depend upon several factors. Among these factors are the impedance of the gyro torquer coil, the power dissipation capability of Q3, the stability of the TCG loop against self-oscillation, and the voltage available for dropping across the torquer

coil. The latter two factors can be reasonably well predicted. The range of impedance levels for strapdown gyro torquer coils is beyond the author's knowledge, but an estimate of a DC resistance range of 10  $\Omega$  to 200  $\Omega$  will be made.

#### Maximum Torquing Current of the TCG

The voltage available for dropping across the torquer coil will be considered first. Naturally, the impedance of the torquer coil and the voltage across the coil define the current through it. Each of the composite FET-bipolar transistors in the H-switch (or in the sampling resistor switching network) has a voltage drop across the collector (drain) to emitter of 0.5 V to 1.0 V, depending on the torquing level. Three of these are normally "on" and three are "off" under steady-state conditions. Thus, a voltage drop 3.0 V maximum can be expected from the three "on" composite transistors. A voltage of 6.2 V normally appears across one or the other of the sampling resistors. This, combined with the voltage drop across three composite transistors, gives an approximate 9.2 V drop accounted for thus far. The voltage drop across the torquer coil is  $I_t R_t$ , where  $R_t$  is the DC resistance of the coil. A small voltage drop across Q3 is desired to hold the device out of saturation. If approximately 3.8 volts is chosen to be the minimum allowable drop across Q3, then a maximum of 31.2 volts is available at the emitter of Q3 to drop across the H-switch and sampling resistor network. Since 9.2 volts of this has already been accounted for, a maximum of 22 volts is available to drop across the torquer. As a result, one can write

$$I_t R_t = 22 \text{ V} . \quad (10.1)$$

A plot of Equation (10.1) is given in Figure 10.1. The cross-hatched region above the curve is forbidden because of voltage supply constraints.

Another constraint on the maximum allowable torquing current is the power dissipation capability of Q3. The manufacturer specifies the MPS-U06 to have a dissipation of 10 W when properly heat-sinked. The  $P_D(\text{max})$  of the device must be derated 80 mW/°C above 25°C. Assuming the operating temperature to be 55°C, 2.4 W must be subtracted from  $P_D(\text{max})$ . Another 1.6 W will be subtracted to give a small margin of safety. The resulting available  $P_D(\text{max})$  at 55°C is 6 W. The power dissipation in Q3 is

$$P_D = I_t V_{CE} . \quad (10.2)$$

$V_{CE}$  is just 35 V minus the voltage at the top of the H-switch. The voltage at the top of the H-switch is approximately

$$V_1 = (9.2 + I_t R_t) \text{ volts} . \quad (10.3)$$

$V_{CE}$  thus becomes

$$V_{CE} = (25.8 + I_t R_t) \text{ volts} . \quad (10.4)$$

If Equation (10.4) and  $P_D = P_D(\text{max}) = 6 \text{ W}$  are substituted into Equation (10.2), a relationship between  $I_t$  and  $R_t$  with  $P_D(\text{max})$  as a parameter is obtained. This relationship is

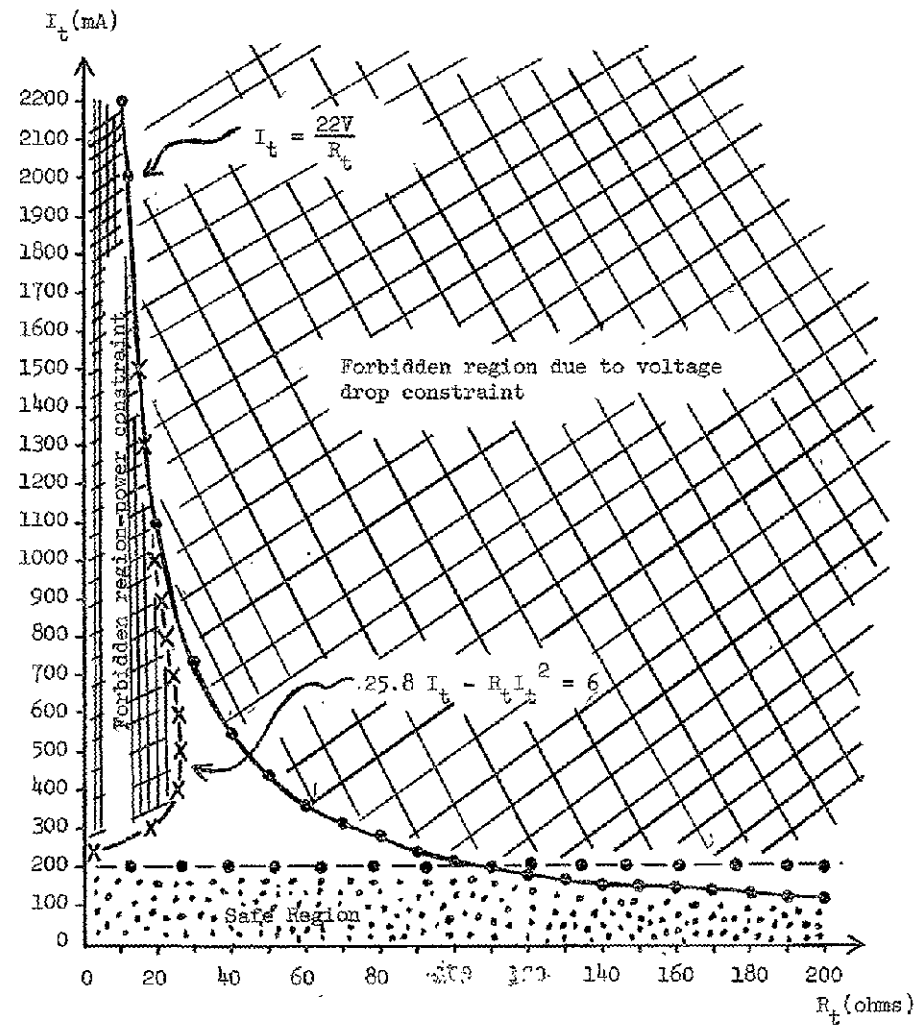


FIGURE 10.1

PLOTS OF VOLTAGE DROP AND POWER DISSIPATION  
CONSTRAINTS INDICATING TORQUING CURRENT AND  
TORQUE RESISTANCE RANGES, FOR A POWER  
SUPPLY VOLTAGE OF 35V

$$25.8 I_t - R_t I_t^2 = 6 . \quad (10.5)$$

Equation (10.5) is also plotted in Figure 10.1 along with Equation (10.1). The region to the left and above the plot of Equation (10.5) is a forbidden region of operation because of the power dissipation rating of Q3.

The area not cross-hatched in Figure 10.1 gives the available operating region with respect to voltage drop and power dissipation constraints. This does not include the constraint imposed by the stability of the TCG loop. Stability calculations for the loop indicate that if an additional constraint of  $I_t(\text{max}) = 200 \text{ mA}$  be imposed, a safe operating region below all curves in Figure 10.1 will be defined. This safe operating region is the dotted region in Figure 10.1. This region also indicates the maximum torquing current for a given  $R_t$ .

The dotted region in Figure 10.1 says nothing about error constraints on the maximum allowable torquing current. A study of the error analyses presented earlier in this thesis indicates that there are three errors which become worse with an increase in the high torque level of torquer current. One is  $e_{ss}(t)$ , or the steady-state actuating error. The change has little effect upon the performance of the TCG loop and will be neglected.

A second error which becomes worse with increasing torquer current levels is one associated with the PVR. If all other parameters are equal, the error given in Equation (8.19) becomes  $5.2 \text{ ppm}/^\circ\text{C}$  for an  $I_t$  of 200mA.

The third error of concern here is the error associated with unequal rise- and fall-times. As explained in Chapter VIII, this error

increases with increasing torquer current levels. A graphical approximation similar to that described in Chapter VIII was performed for a torquing level of 200 mA. Although the approximation is crude, the results indicate that an error in current-time area of approximately  $8.3 \times 10^{-9}$  amp.-sec. per interrogation period can be expected. This corresponds to an error in the movement of the gyro float of approximately 0.017 arc-sec. When compared to the current time area in an ideal torque current pulse, the relative error is approximately 200 ppm for a limit cycle frequency of 2.4 kHz. An increase in the limit cycle frequency causes a proportional increase in the relative error. For example, a limit cycle frequency of 10 kHz would cause the 200 ppm error to increase to approximately 830 ppm.

#### Minimum Torquing Current of the TCG

The constraints on the minimum possible torquing current are not altogether the same as those for the maximum torquing current. Power dissipation and voltage drop constraints are not problems in this case. The stability constraint remains. However, calculations on the stability of the loop indicate that an  $I_t$  of as low as 1 mA can be tolerated. The region indicated in Figure 10.1 as being a safe operating region basically holds for the minimum torquing current also. At torquer current levels of 1 mA - 10 mA, the feedback factor B will naturally be larger than for larger torquing currents. Consequently, an increase in the loop gain will occur. Dominant pole compensation may be required at the base of Q2B.

Lower values of torquing current naturally cause static and drift errors to appear worse. The static error given as 0.7 ppm in Equation

(8.14), for  $I_t = 30$  mA, becomes 20.8 ppm for  $I_t = 1$  mA. The worst-case drift error given as 0.07 ppm/°C in Equation (8.15), for  $I_t = 30$  mA, becomes 2.08 ppm/°C for  $I_t = 1$  mA.

Another error which appears to increase relative to a decrease in the current-time area of a torque current pulse is that due to transient feed-through currents in the H-switch. The current-time area in the feedthrough current error per torque pulse was estimated in Chapter VIII to be approximately  $8.75 \times 10^{-11}$  amp.-sec. This corresponds to an error in the gyro float movement of  $1.8 \times 10^{-4}$  arc-sec. When  $I_t = 30$  mA and the limit cycle frequency is 2.4 kHz, the ratio of  $Ai_{(trans.)} = 8.75 \times 10^{-11}$  amp.-sec. to the current-time area in an ideal current pulse,  $Ai_t$ , is approximately 14 ppm. If  $I_t = 1$  mA, and the limit cycle frequency is 2.4 kHz, then the ratio is approximately 420 ppm. If  $I_t = 1$  mA, and the limit cycle frequency is 10 kHz, then the ratio is approximately 1750 ppm.

The current range of the TCG is thus seen to extend from 1 mA, with some additional compensation, to 200 mA. In the extreme low levels of the range, static, drift, and transient feedthrough currents in the H-switch become principal areas of concern. In the extreme high levels of the current range, PVR drift error and error due to unequal rise- and fall-times take the dominant roles as errors to be closely observed. Increasing the limit cycle frequency compounds the transient feedthrough errors in the H-switch and the error due to unequal rise- and fall-times.

The TCG circuit illustrated in Figure 3.1 is overly complicated if torquer current levels of 1 mA - 5 mA in low torquer resistances are desired. The circuit illustrated in Figure 10.2 was developed and used

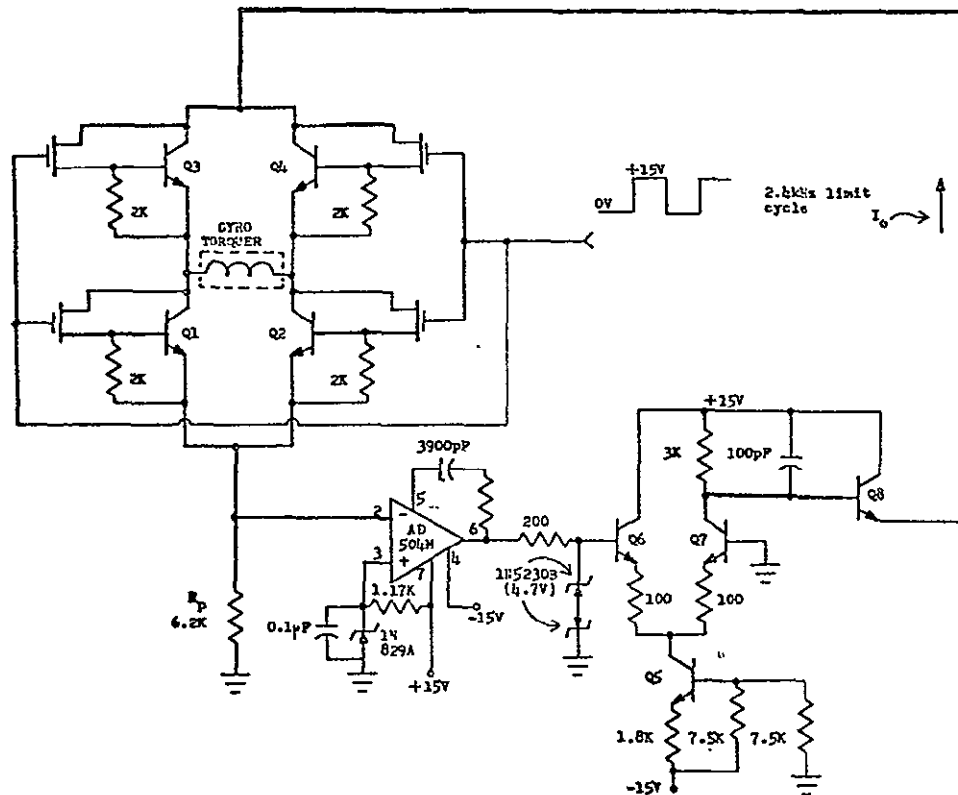


FIGURE 10.2

A TCG CIRCUIT FOR LOW-LEVEL TORQUING CURRENTS  
AND LOW DC TORQUER RESISTANCES



by Dr. E. J. Kennedy and Dr. T. V. Blalock in recent months. The circuit has the same basic circuit configuration as that in Figure 3.1, but is greatly simplified. The H-switch driver circuit is not present; the sampling resistor switching network is not necessary since only one sampling resistor is being used; the FET-diode current source feeding the 1N829A Zener reference diode is not present; feedforward compensation is unnecessary, although additional capacitance has been added to compensate the op. amp. and a capacitor at the base of Q8 replaces the RC lag compensation; and a standard complementary MOS digital circuit (CMOS) is used in the H-switch.

#### B. Some Possible Modifications of the TCG

The following material is not intended to be an exhaustive study of all possible modifications of the TCG. Rather, some of the possible and meaningful modifications will be illustrated to exhibit the versatility of the TCG. An attempt will be made to organize the material according to what logic is used and whether or not a 35 V supply is used.

##### Driving the TCG with TTL Logic

TTL logic signals may be used to drive the H-switch driver circuit and the sampling resistor switching network. With 0 to 5 V level signals, it becomes necessary to level shift to drive the MOSFET gates used in the H-switch and sampling resistor switching network. The type of level shifting required depends heavily upon the supply voltage attached to the collectors of Q1, Q2B, and Q3.

### Driving with TTL Logic with 35 V Supply Present. . .

This situation is the one illustrated in Figure 3.1. The TTL to CMOS interface illustrated in Figure 3.2 is necessary for these circumstances. Since these circuits have already been discussed in detail, no further comment will be made on the TTL logic drive with 35 V supply utilized.

### Driving with TTL Logic with 35 V Supply Eliminated

Elimination of the 35 V supply is easily accomplished if one does not require a high current drive. However, as determined in section A of this chapter, the upper limit of torquer current is a function of voltage available for dropping across the torquer coil. The problem, then, is to eliminate the +35 V supply and still have a reasonably large voltage differential between the top of the H-switch and the bottom of the sampling resistors. This can be accomplished by using +15 V wherever +35 V was used, and connecting the sampling resistors and Zener reference diode to -15 V at a common point instead of ground. The substrates of the 3N190's should be tied to +15 V, and the substrate of the MM552D should be biased at -5 V. The -5 V bias can be obtained using a 1N758 Zener diode and a 953  $\Omega$  resistor connected in series between -15 V and ground. A schematic illustrating these changes is not given since one can easily visualize the changes by studying Figure 3.1.

The changes in the TCG outlined in the above paragraph necessitate a new H-switch driver circuit and a new TTL to CMOS interface circuit to drive the sampling resistor switching network. The TTL to CMOS interface

circuit will need a -5 V supply. Figure 10.3 illustrates a modification of the H-switch driver circuit to allow elimination of the 35 V supply when using TTL logic. Figure 10.4 is a schematic of a TTL to CMOS interface for driving the sampling resistor switching network with no +35 V supply and using TTL logic. A (-5)V bias for the TTL to CMOS interface is given in Figure 10.5.

Many other modifications of the TCG which allow elimination of the +35 V supply are of course possible. Partial schematics which illustrate the salient features of two of these modifications are given in Figure 10.6 and Figure 10.7. The H-switch and sampling resistor switching network remain the same. The circuits illustrated in Figures 10.3, 10.4, and 10.5 are necessary to drive these two networks.

#### Driving the TCG with CMOS Logic

CMOS (complimentary metal-oxide semiconductor) technology is growing rapidly today. A CMOS capability is being developed by a growing number of IC manufacturers. CMOS circuits have unique features which demand attention from design engineers. Features like low power dissipation and high logic noise immunity are outlined with other features in Reference 51. Although this work is not primarily concerned with the logic to be used in the pulse rebalance electronics loop, References 52 through 59 are given as indicative of a trend which makes the material given here pertinent.

#### Driving with CMOS Logic with 35 V Supply Present

The normal logic levels of CMOS logic are either 0 V to 10 V or 0 V to 15 V depending on the supply used. When CMOS logic is used to

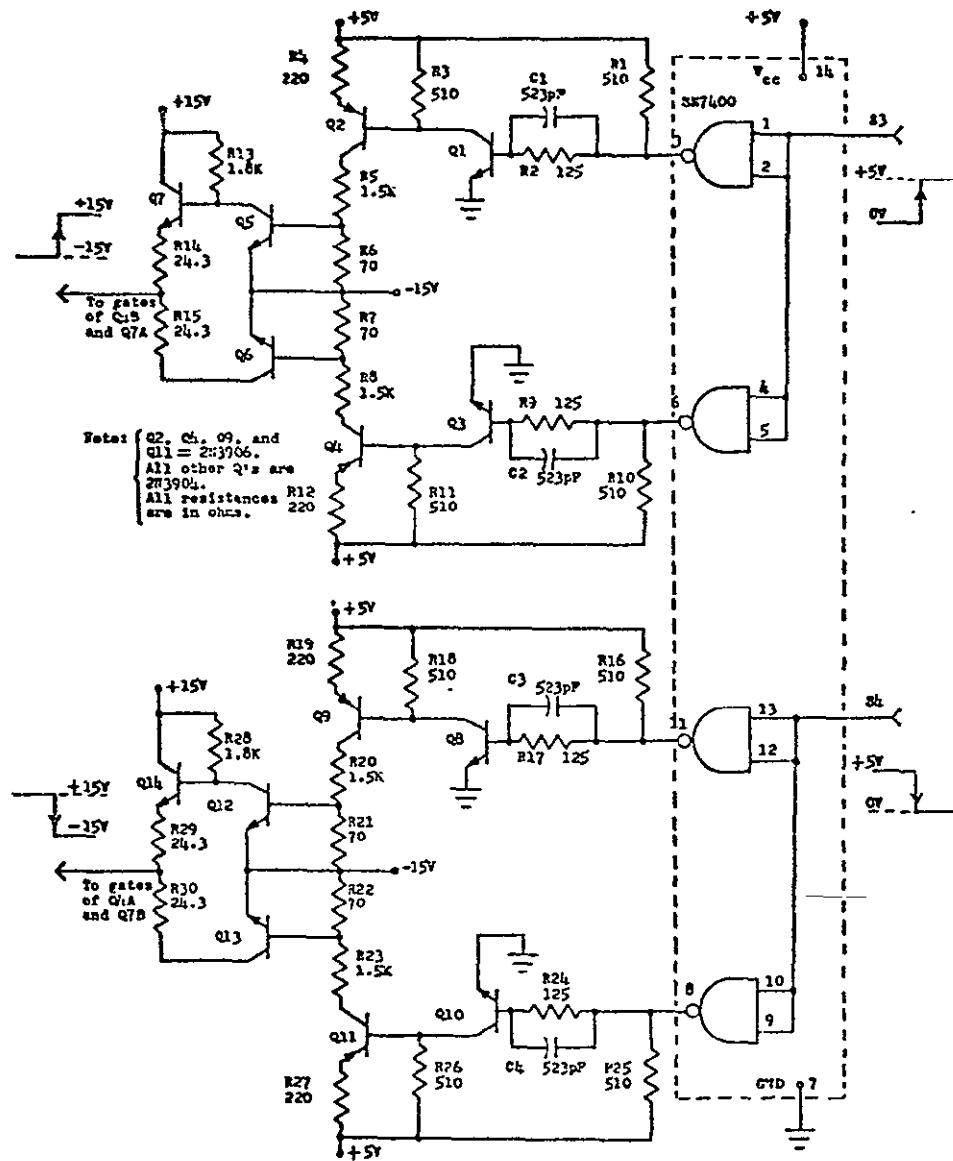


FIGURE 10.3

A MODIFICATION OF THE H-SWITCH DRIVER TO ALLOW  
ELIMINATION OF THE 35V POWER SUPPLY USING TTL LOGIC

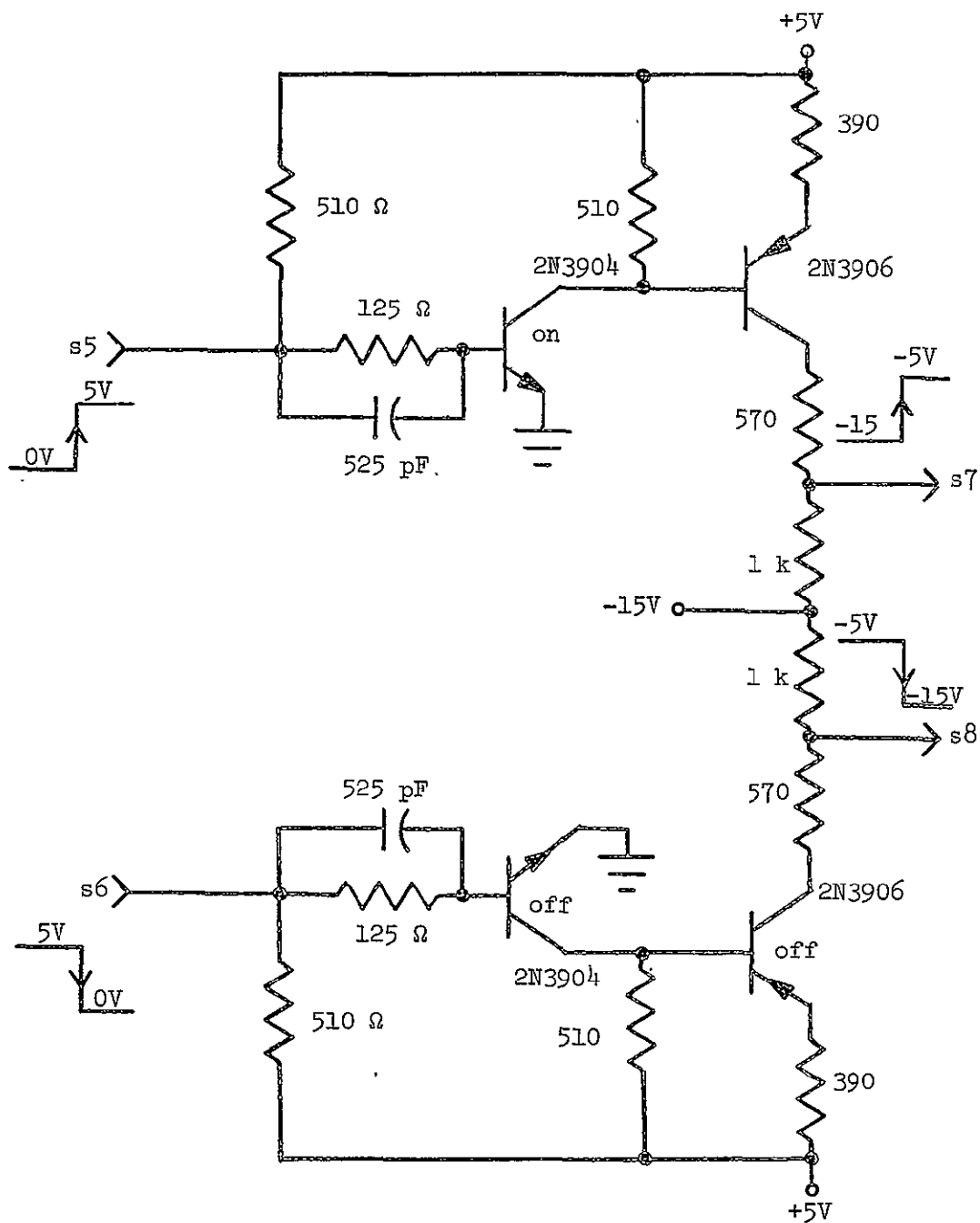
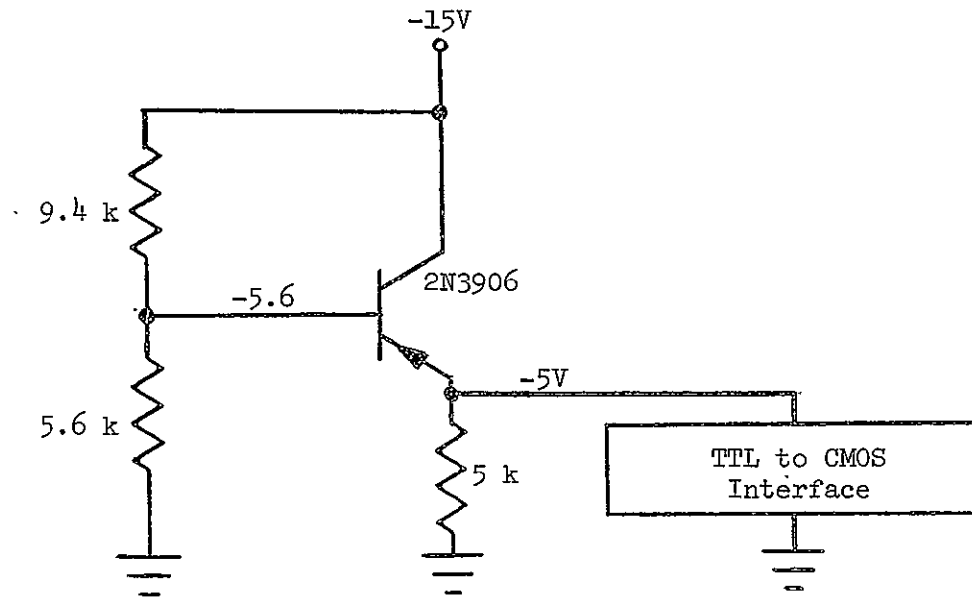
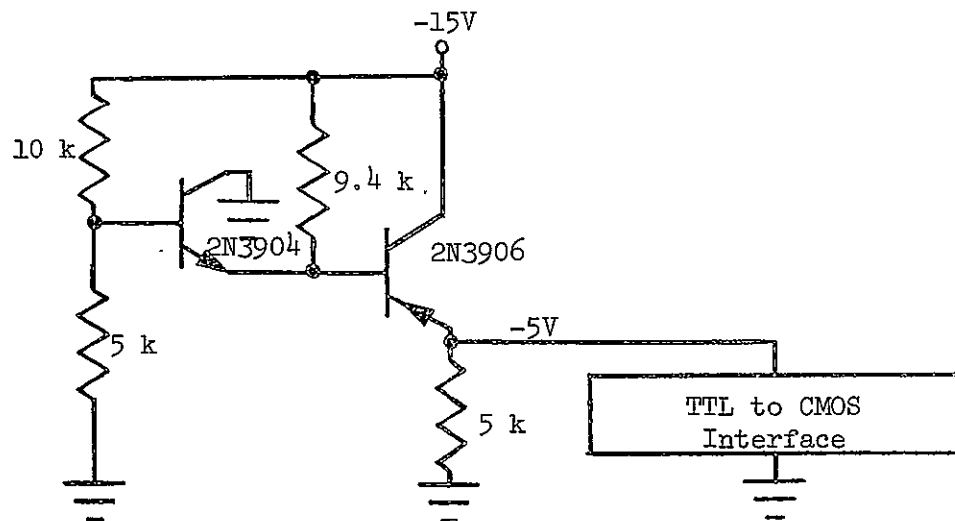


FIGURE 10.4

TTL TO CMOS INTERFACE FOR DRIVING THE SAMPLING  
RESISTOR SWITCHING NETWORK WITH NO 35V SUPPLY  
AND USING TTL LOGIC



(a) A simple -5V bias.



(b) A (-5)V bias with better temperature stability.

FIGURE 10.5

(-5)V BIAS FOR TTL TO CMOS INTERFACE

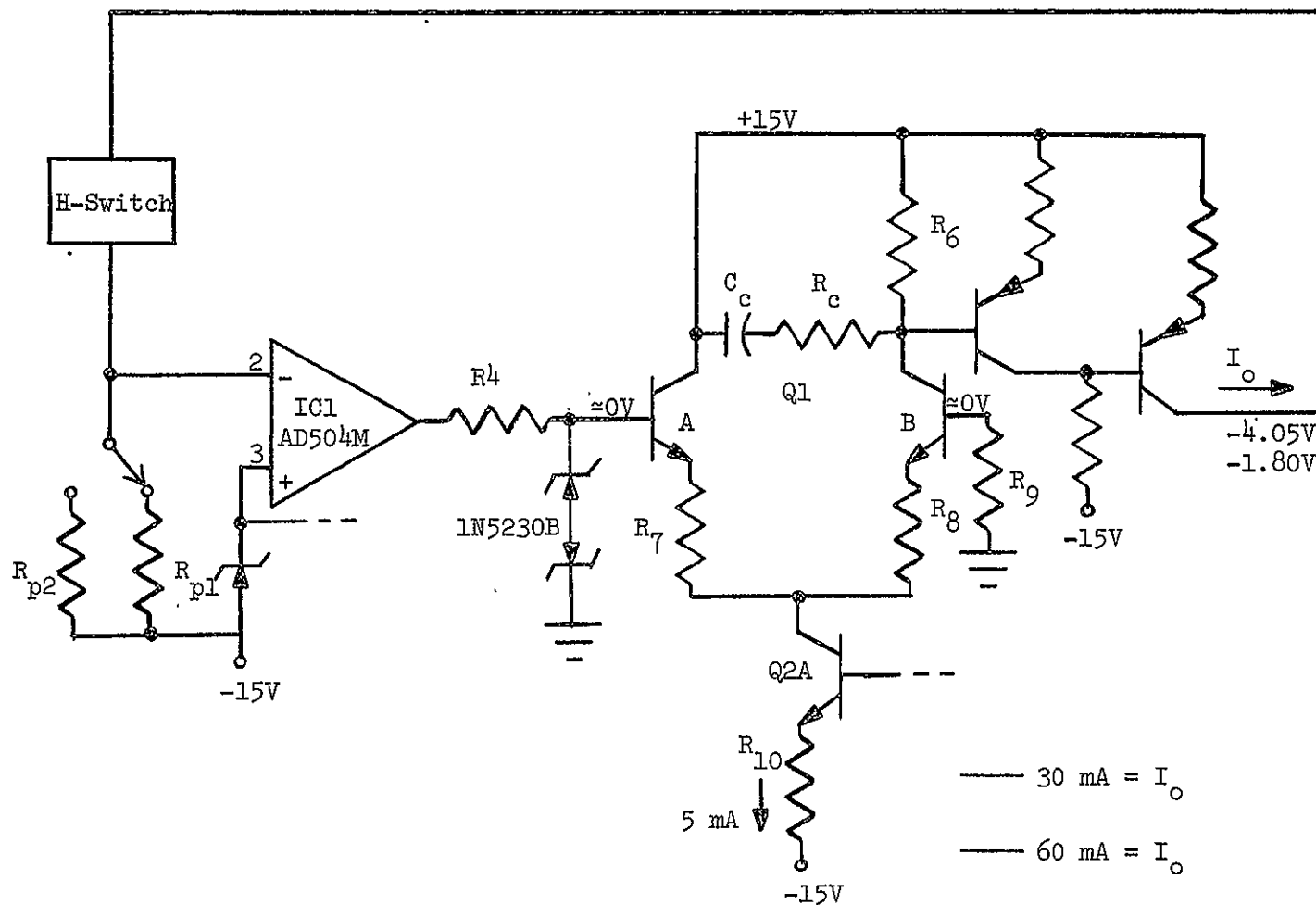


FIGURE 10.6

MODIFICATION OF TCG TO ACCOMMODATE ELIMINATION OF +35V SUPPLY

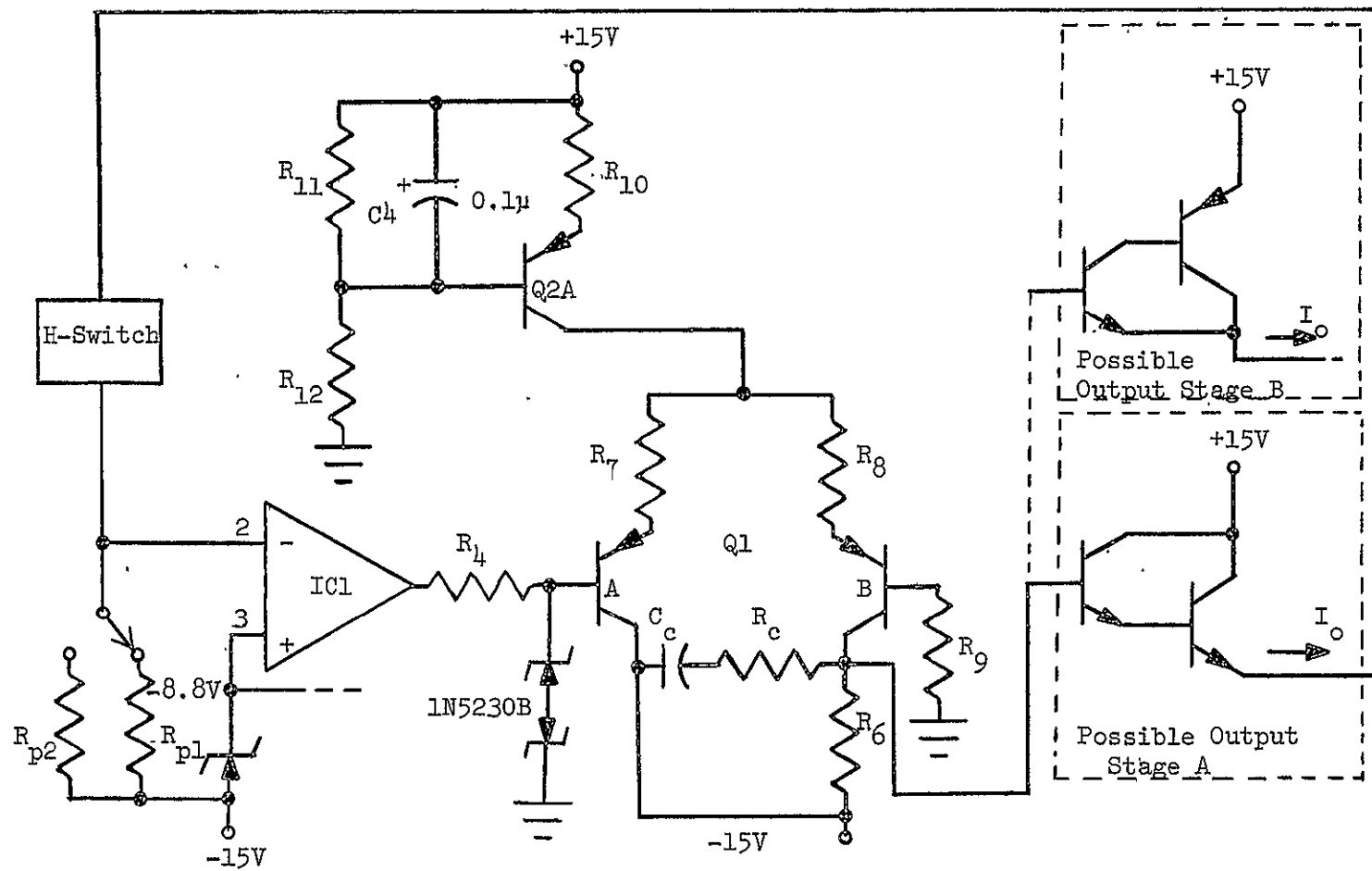


FIGURE 10.7

MODIFICATION OF TCG TO ACCOMMODATE ELIMINATION OF +35V SUPPLY  
WITH ALTERNATE OUTPUT STAGES



drive the TCG, the sampling resistor switching network can be driven directly by the logic section. The TTL to CMOS interface can be discarded. An alternate H-switch driver circuit is required. The driver circuit must pull but little current from the CMOS logic. Such an H-switch driver circuit is given in Figure 10.8. The circuit in Figure 10.8 was constructed and experimentally tested. Rise- and fall-times of 25 nsec and 15 nsec, respectively, were achieved at the out 1 and out 2 output terminals.

#### Driving with CMOS Logic with 35 V Supply Eliminated

Any of the modifications of the TCG discussed above which eliminate the +35 V supply apply for the case here. Any of these can be driven by CMOS logic.

Again, if the sampling resistors and Zener reference diode are connected to -15 V, new circuits for the H-switch driver and sampling resistor switching network are required. Figure 10.9 is an H-switch driver circuit for the case when CMOS logic is used and no +35 V supply is present. Figure 10.10 is an interface circuit to drive the sampling resistor switching network from CMOS logic.

#### The TCG with One Sampling Resistor

Dual scale factor capability is achieved in the TCG by switching the sampling resistors.

An alternative is to apply just enough torquing current to the gyro to handle the largest rate changes and have only one level of torquing current. A switching network to change sampling resistors is

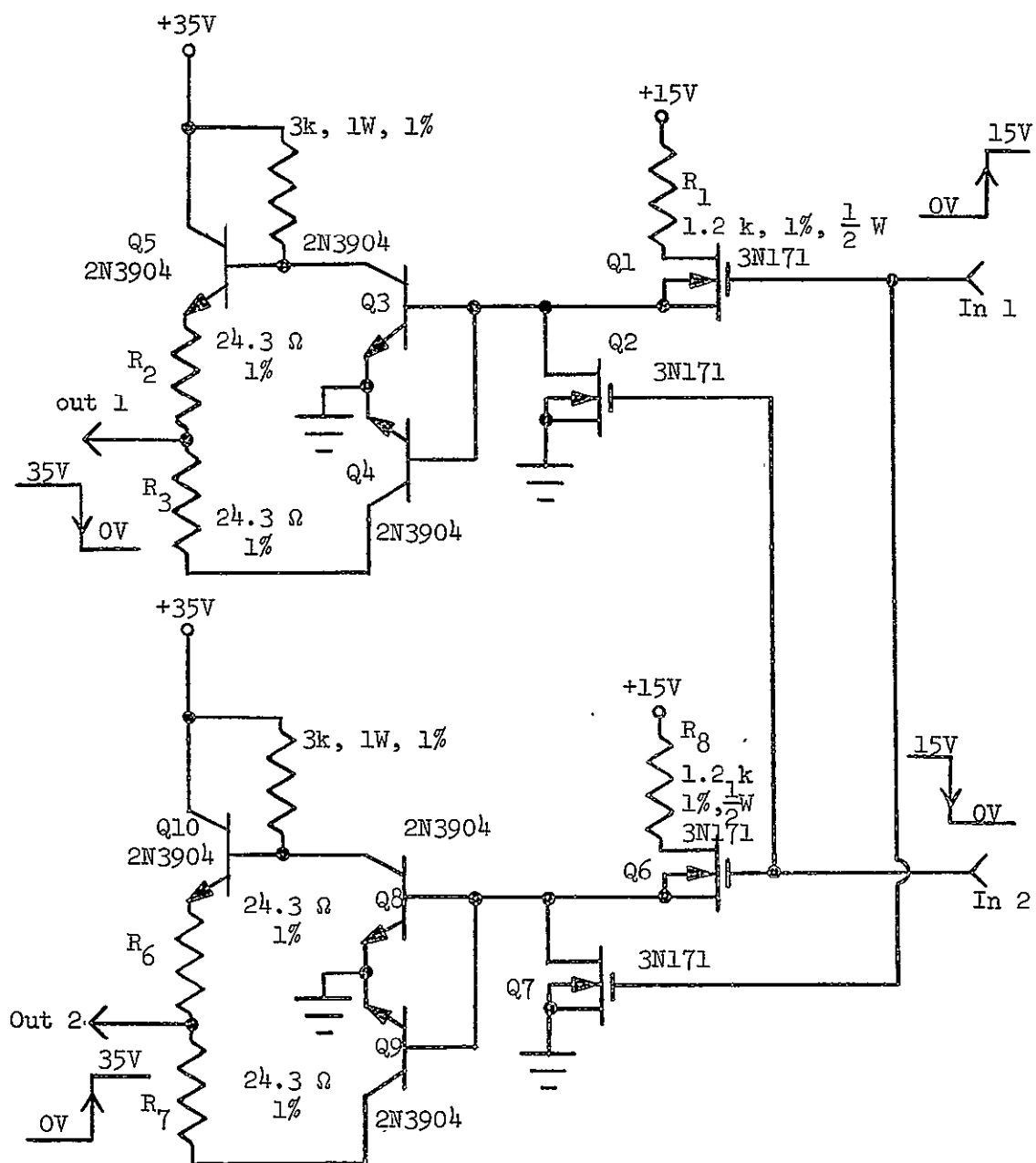


FIGURE 10.8

AN H-SWITCH DRIVER CIRCUIT FOR USE WITH CMOS LOGIC

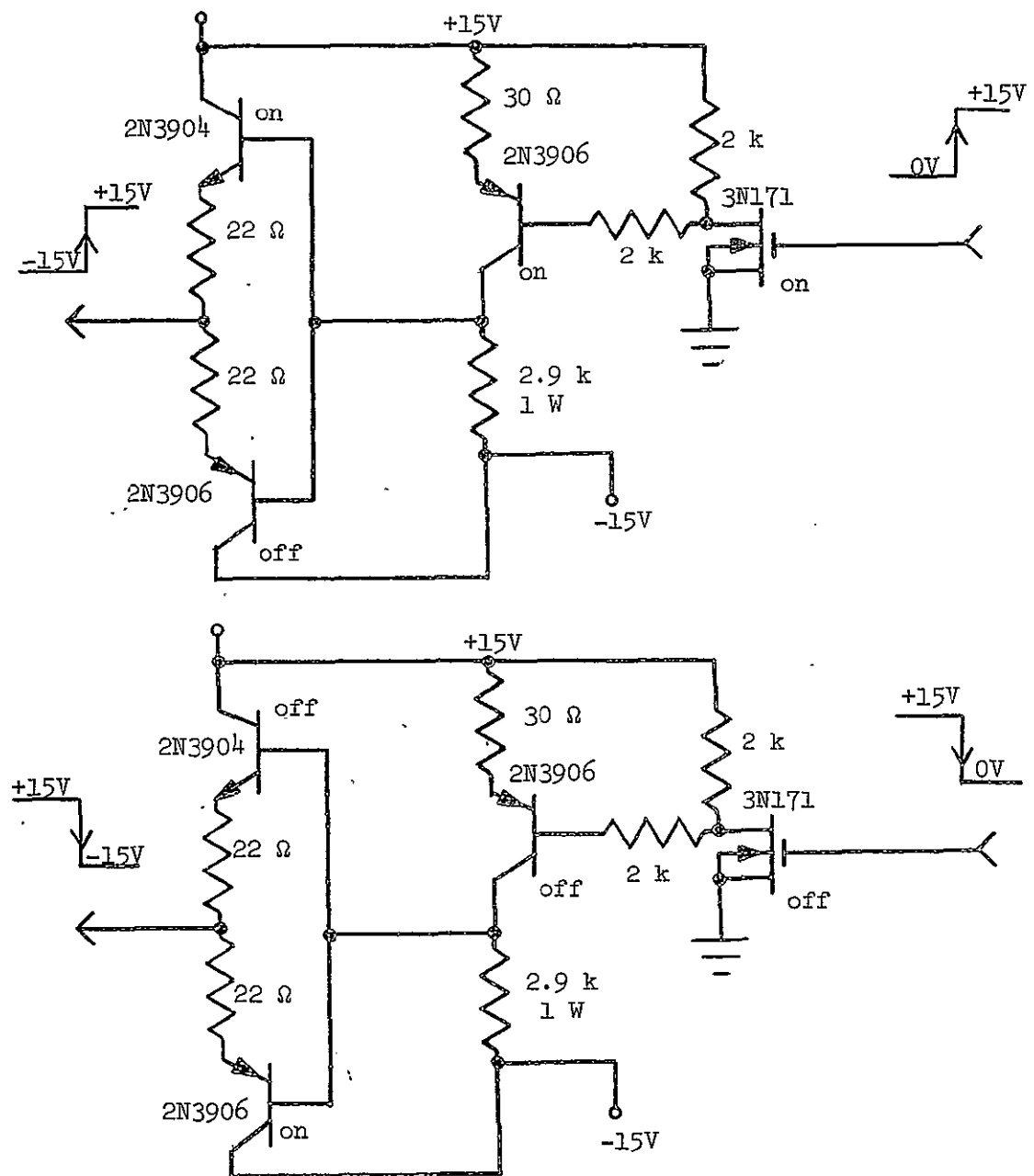


FIGURE 10.9

H-SWITCH DRIVER CIRCUIT FOR THE CASE WHEN CMOS LOGIC AND NO 35V SUPPLY IS USED

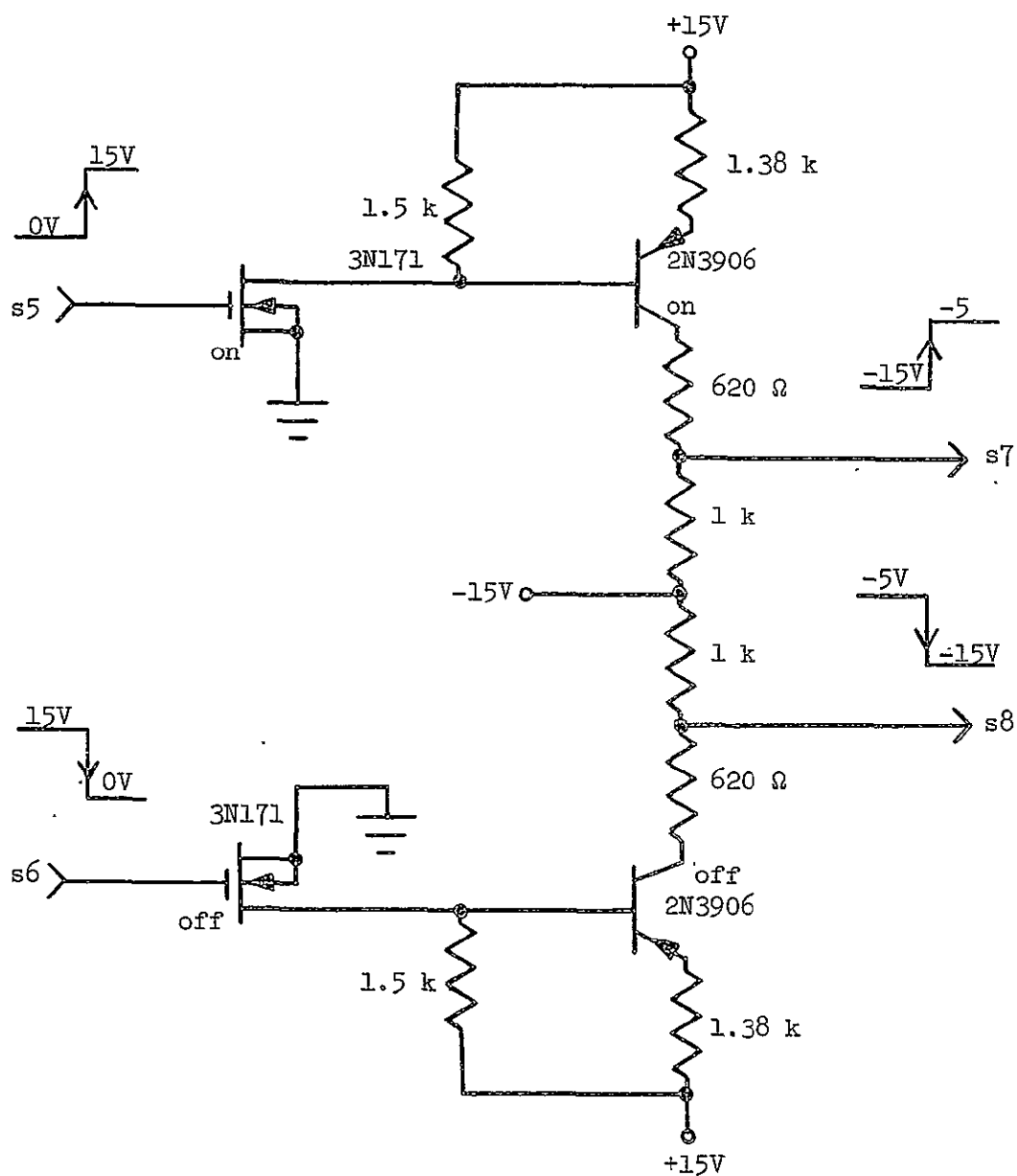


FIGURE 10.10

INTERFACE CIRCUIT TO DRIVE SAMPLING RESISTOR SWITCHING  
NETWORK WHEN CMOS LOGIC AND NO 35V SUPPLY IS USED

then unnecessary. An interface circuit to interface the sampling resistor switching network with the logic section is of course eliminated also. Operation with one sampling resistor not only simplifies the TCG, but also eliminates the error caused by switching the sampling resistors. In addition, the feedforward compensation on the AD504M op. amp. can be removed. The large overdrive signals developed at the op. amp. input due to switching the sampling resistors would no longer exist. A simplification of the logic driving the TCG could also be simplified since no scale factor command would be necessary.

#### Effect of a Lower PVR

The Zener reference diode used in the TCG has a breakdown of 6.2 volts. 6.2 V is the lowest voltage breakdown presently available in a temperature-compensated Zener diode. However, National's LM113 alleviates this problem. The LM113 is a 1.22 V temperature compensated shunt regulator diode. Transistors and resistors are used to synthesize the reference rather than using a breakdown mechanism.

One major advantage of having a lower PVR is a lower power dissipation in the sampling resistors. For a PVR of 1.22 V and a torquer current of 30 mA, only approximately 0.037 watts are dissipated in the sampling resistor. With the same current and a PVR of 6.2 V, the dissipation in the sampling resistor is approximately 0.186 watts.

Another advantage would be realized when switching sampling resistors. The transient spikes appearing at the input of the op. amp. would be at least three times smaller when a PVR of 1.22 volts is used.

The loop gain would be slightly reduced if a lower PVR were used, assuming all other parameters equal. This would result from a smaller feedback factor due to a smaller sampling resistor. With the same compensation, a larger phase margin and hence a greater degree of stability should result.

A further advantage of using a 1.22 V PVR is that larger torquer currents could be driven without a +35 V supply than would be possible with a 6.2 V reference. The extra capability results from the additional 5 volts available for dropping across the torquer coil.

Along with the advantages of a lower PVR, one might consider the possibility of a current reference. There are numerous circuits available which may be connected in a suitable way to serve as precision current sources or sinks. The precision current source could drive a voltage divider network to supply a reference voltage to the op. amp.

One principal advantage of a current reference is obvious. The circuit would, if judiciously selected, generate less noise than a Zener reference diode.

Several modifications which might be made to the TCG have been discussed in this chapter. Elimination of the +35 V supply poses no great problem to the current regulator portion of the TCG. However, elimination of the +35 V supply does present problems with interfacing the TCG to the logic from which it receives its commands. Note should be made of the fact that most of the modifications discussed in this chapter are paper designs and have not been experimentally verified. The circuit in Figure 10.2 was constructed and experimentally tested by

Dr. E. J. Kennedy and Dr. T. V. Blalock of the University of Tennessee Electrical Engineering Department. The circuit in Figure 10.8 was constructed and experimentally tested by the author.

## CHAPTER XI

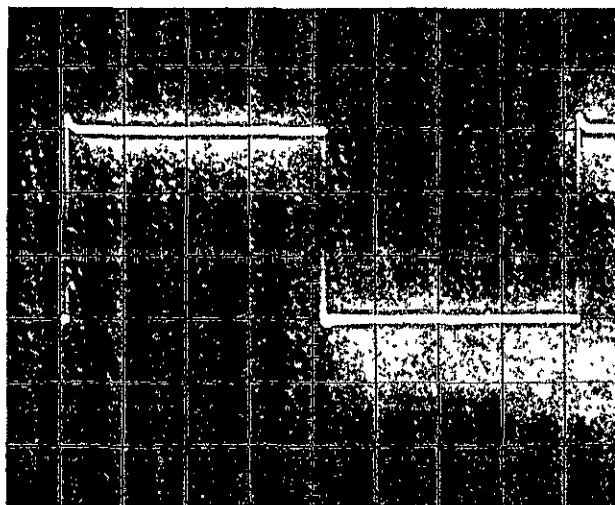
### EXPERIMENTAL RESULTS

The TCG, as it appears in Figure 3.1, was constructed and experimentally evaluated. The TCG was combined with other functional blocks to complete the pulse rebalance electronics loop.

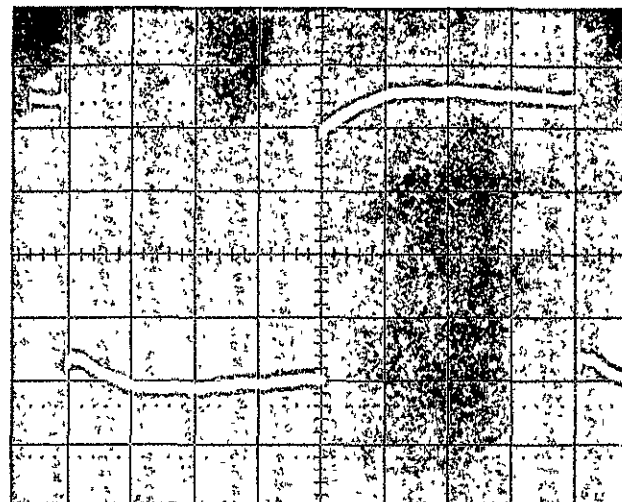
The rebalance electronics loop was evaluated using both the Honeywell GG334 and Kearfott 2544 gyros. The loop functioned well with both gyros. Since MSFC expressed more interest in the Kearfott 2544 gyro at the time, most of the experimental data was taken with this gyro in the loop.

The principal test of the TCG's performance is the current waveform in the gyro's torquer coil. Other waveforms, rise- and fall-times, etc., around its loop are important, but in a secondary sense. Using the Kearfott 2544 gyro, the rise- and fall-times (10-90%) for the current pulse through the torquer were 70 nsec and 90 nsec, respectively. Figure 11.1 (a) shows the waveform of the applied torquer current. Figure 11.1 (b) shows the waveform of the voltage across the compensated torquer winding for 30 mA of torquing current. The waveforms in Figure 11.2 represent the transient response of the current through the torquer as the torque current is being switched from a low value of 30 mA to a high value of 60 mA. The pips seen riding on the waveform in Figure 11.2 (a) are the result of the 19.2 kHz synchronous generator frequency. The rise- and fall-times (10-90%) in Figure 11.2 (b) are approximately 12  $\mu$ sec. This represents approximately 8 data periods to switch ranges, since a





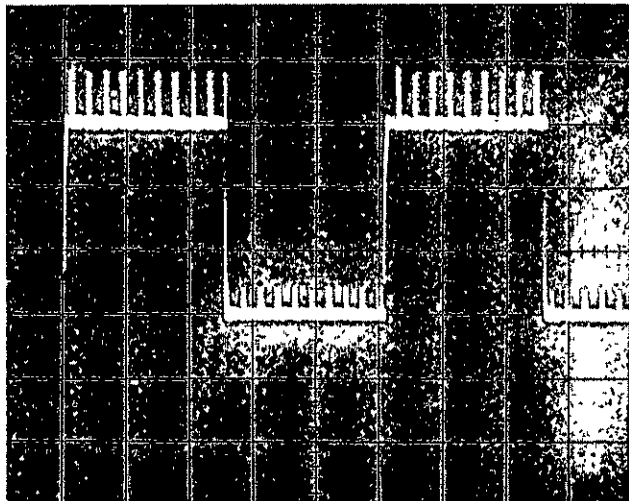
(a) Current through torquer, spin motor on, low torque (30 mA); 20 mA/div., 50  $\mu$ s/div.



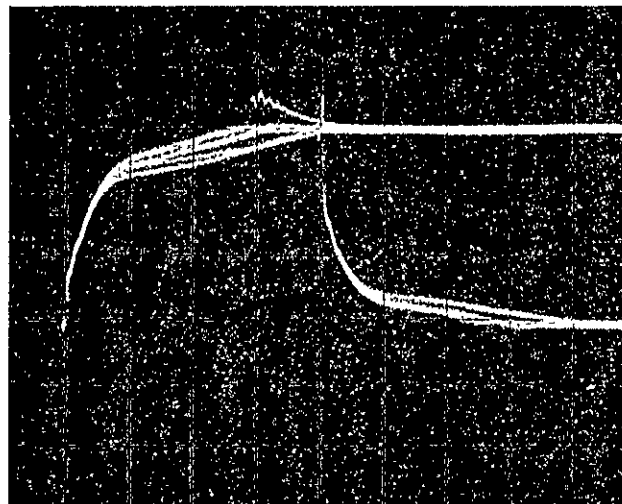
(b) Voltage across torquer, spin motor, low torque (30 mA); 1V/div, 50  $\mu$ s/div.

FIGURE 11.1

CURRENT AND VOLTAGE WAVEFORMS THROUGH AND ACROSS THE  
TORQUER WHEN TORQUING THE KEARFOTT 2544 GYRO



(a) 10 mA/div, 500  $\mu$ s/div.  
Switching rate of 390 Hz.



(b) Rise- and fall-times of current.  
10 mA/div, 5  $\mu$ s/div.

FIGURE 11.2

TRANSIENT RESPONSE OF TORQUER CURRENT WHEN SWITCHED FROM LOW  
TO HIGH SCALE (30 mA TO 60 mA). SPIN MOTOR ON.

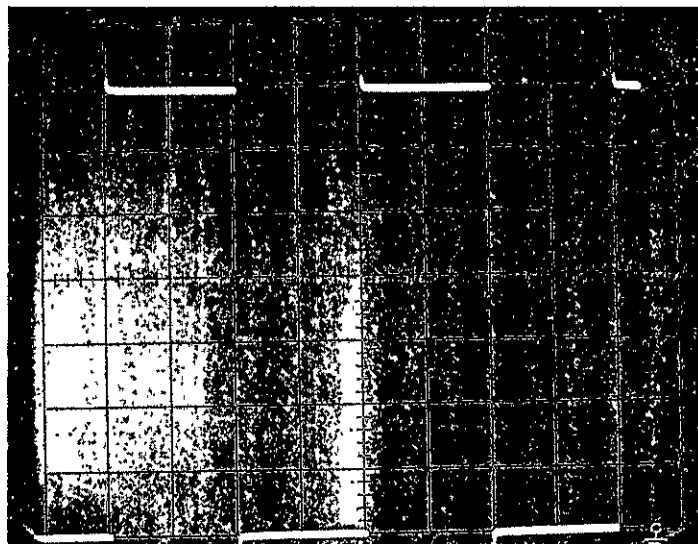
data period is 1.63 sec. Figures 11.1 and 11.2 were taken from Reference 5.

Some additional photographs are given to exhibit experimental evidence of other voltage waveforms at various points in the TCG circuit. Figure 11.3 shows the output of the H-switch driver driving the H-switch at a 2.4 kHz rate. Referenced to Figure 3.1, inputs S3 and S4 were pulsed with a TTL signal at 2.4 kHz; S1 and S2 were held constant in a manner to command a low-torque level (30 mA). The rise time of the H-switch driver output is approximately 22 nsec. The fall time, though not shown, is approximately 15 nsec.

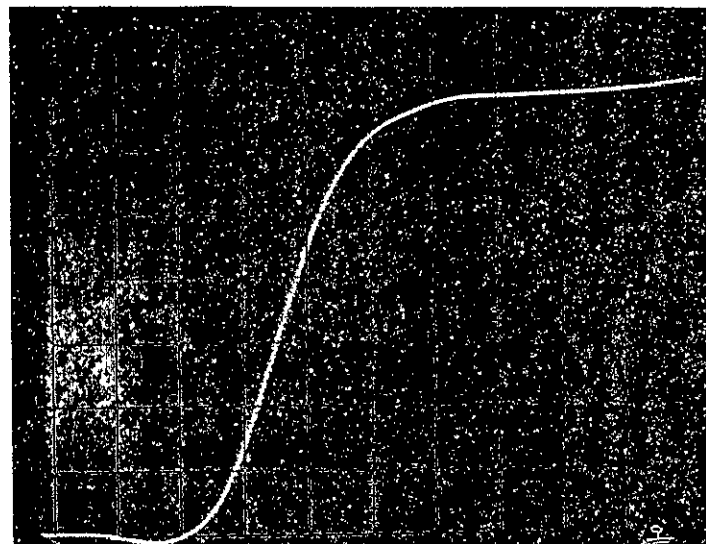
The waveforms given in Figure 11.4 illustrate transient inputs to the AD504M op. amp. when the torquing current levels are being switched (from 30 mA to 60 mA and vice-versa). Figure 11.4 (a) illustrates the transient spikes occurring at pin 2 of IC1 when switching sampling resistors. The transients occurring here were discussed earlier in the thesis in relation to the feedforward compensation for the AD504M op. amp. These transient spikes drive the op. amp. into a nonlinear region of operation and cause the long settling time mentioned above. A study of Figure 11.4 (b) indicates that the PVR holds the voltage at pin 3 of IC1 relatively constant during scale factor switching operations.

Voltage waveforms across the sampling resistors during scale factor switching and the corresponding IC1 op. amp. output are given in Figure 11.5. Some of the transient nonlinearity in the operation of the op. amp. during scale factor switching appears in trace A of Figure 11.5 (b). The photographs in Figure 11.4 and 11.5 were taken under the

ORIGINAL PAGE IS  
OF POOR QUALITY

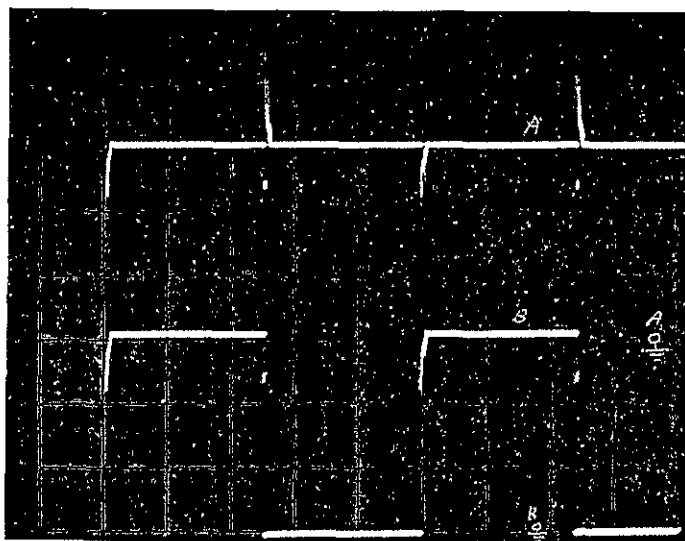


(a) vertical: 5V/div  
horizontal: 100  $\mu$ s/div

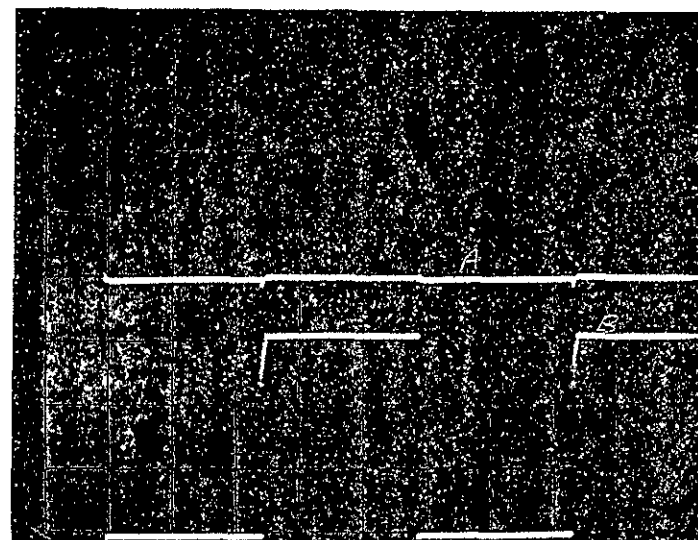


(b) vertical: 5V/div  
horizontal: 10 ns/div

FIGURE 11.3  
AN OUTPUT OF THE H-SWITCH DRIVER (GATE OF Q4B.)



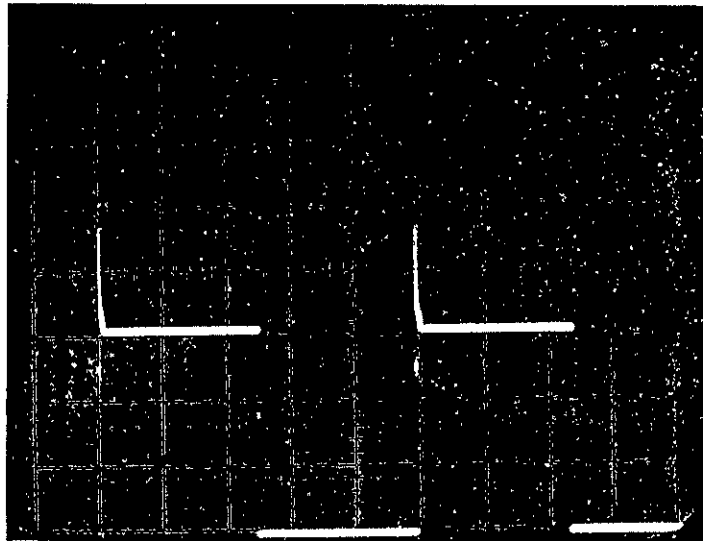
(a) Trace A - pin 2, IC1  
Trace B - top of  $R_{p2}$   
Vertical: 2V/div  
Horizontal: 200  $\mu$ s/div



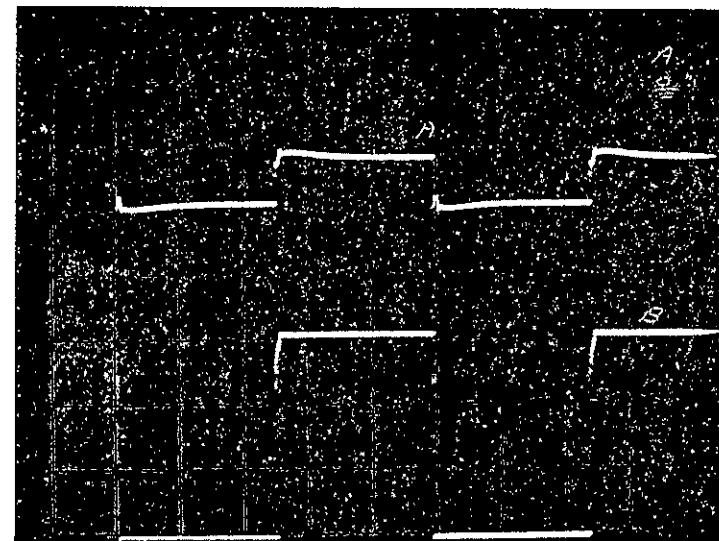
(b) Trace A - pin 3, IC1  
Vertical for Trace A:  
0.05V/div with AC  
coupling.  
Trace B - top of  $R_{p2}$   
Horizontal for A,B:  
200  $\mu$ s/div

FIGURE 11.4

TRANSIENT INPUTS TO THE AD504M OP. AMP. WHEN SWITCHING  
TORQUING SCALE FACTORS (30 mA-60 mA)



(a) Top of  $R_{p1}$   
 Vertical: 2V/div  
 Horizontal: 200  $\mu$ s/div



(b) Trace A - pin 6, IC1  
 Vertical scale for trace A:  
 0.2V/div  
 Trace B - Top of  $R_{p2}$   
 Vertical scale for trace B:  
 2V/div  
 Horizontal scale for A, B:  
 200  $\mu$ s/div

FIGURE 11.5

VOLTAGE WAVEFORMS ACROSS SAMPLING RESISTORS AND AT IC1 OP. AMP.  
 OUTPUT DURING SCALE FACTOR SWITCHING (30 mA-60 mA)

following conditions: with reference to Figure 3.1, S3 was held at +5V and S4 at 0V; S1 and S2 were driven by the TTL to CMOS interface circuit in Figure 3.2, at a 1 kHz rate.

The TTL to CMOS interface in Figure 3.2 was experimentally evaluated. With reference to Figure 3.2, the observed rise time at S7 or S8 was 60 nsec. The observed fall time at the same terminals was 16 nsec.

## CHAPTER XII

### CONCLUSIONS

#### A. Summary

The objective of this thesis was to design, implement, analyze, and experimentally evaluate a torque current generator with optimum performance. The primary expected application for the TCG was that it be used in a width-modulated binary pulse rebalance electronics loop for strapdown gyroscopes. A degree of versatility was to be built into the circuit so that a wide range of current levels might be achieved with a wide range of gyros. As a means of evaluating the resulting design, the following criteria were chosen as figures of merit: steady-state accuracy; margins of stability against self-oscillation, temperature variations, aging, etc.; static and drift errors; PVR errors; transient errors; classical frequency and time domain characteristics; and the equivalent noise at the input of the op. amp.

Chapter I presented brief background material on current regulating problems associated with strapdown gyros. Two commonly used schemes for current levels incorporated in pulse torquing methods were briefly discussed.

In Chapter II, design considerations for the TCG were discussed. References 1 through 4 were relied upon heavily for experience in formulating a well-founded design approach to the TCG problem.

Implementation of the TCG was detailed in Chapter III. The DC feedback loop was outlined in general, and each functional block was



discussed in particular. In addition, torquer compensation and a TTL to CMOS interface circuit were discussed.

Chapters IV through X presented the analysis section of the TCG. The figures of merit mentioned immediately above, as well as other pertinent aspects of the TCG, were obtained and discussed. A summary in tabular form of the principal results will be presented shortly.

Some of the more important experimental results were reported in Chapter XI. Those of prime concern will be listed in Table 12.1 along with the analytical entries.

Table 12.1 is a tabular summary of theoretical and experimental performance characteristics of the TCG. Experimental entries are indicated by (\*) following the item entry.

#### B. Suggestions for Further Study

While working on the material in this thesis, several areas surfaced where work in addition to that presented here would be desirable. Some of these afterthoughts will be presented here.

The TCG system is not purely continuous, but has associated digital elements. A system analysis to include these elements would be educational.

Radiation effects upon the operation and performance of the TCG have not been explored in this thesis. An interdisciplinary study on this topic might clarify some of the unknowns about the long-term characteristics of the TCG in its proposed environment.

The possibilities of using more CMOS circuitry in the TCG should be investigated. Power conservation techniques could be mated with this topic.

TABLE 12.1

A TABULAR SUMMARY OF THEORETICAL AND EXPERIMENTAL  
PERFORMANCE CHARACTERISTICS OF THE TCG

Item	High-Torque Case	Low-Torque Case
Magnitude of midband loop transmission	157.3 dB	159.4 dB
Actuating error, $\epsilon_{ss}(t)$ , under steady-state conditions	0.0136 ppm	0.011 ppm
Error (Precision Voltage Reference)	2.2 ppm/°C (<96 ppm/month)	3.6 ppm/°C
Static and drift errors in sensed current	0.7 ppm and 0.07 ppm/°C	
Overall Accuracy (worst-case analysis)	$\leq (3.6 \text{ ppm/}^\circ\text{C and } 96 \text{ ppm/month})$ $+ (0.7 \text{ ppm and } 0.07 \text{ ppm/}^\circ\text{C})$ $+ (<75 \text{ ppm})$	
Gain margin	21 dB	18 dB
Phase margin	30°	27°
Gain crossover frequency	105 kHz	130 kHz

TABLE 12.1 (continued)

Item	High-Torque Case	Low-Torque Case
Phase crossover frequency	600 kHz	600 kHz
Closed-loop high corner frequency	200 kHz	205 kHz
Bandwidth (closed-loop)	200 kHz	205 kHz
Magnitude of peaking in closed-loop frequency response	6.1 dB	7.0 dB
Frequency of peaking	108 kHz	130 kHz
Magnitude of closed-loop voltage gain	5.66 dB	3.28 dB
Change in loop transmission with temperature	3760 ppm/°C or 1.875% for a 5° C change	3840 ppm/°C or 1.919% for a 5° change
Error ( $I_{\text{sensed}}$ ) due to transient feedthrough currents in H-switch	7 ppm	14 ppm
$I_t = 1 \text{ mA}$ , limit cycle freq. = 2.4 kHz		420 ppm
$I_t = 1 \text{ mA}$ , limit cycle freq. = 10 kHz		1750 ppm

TABLE 12.1 (continued)

Item	High-Torque Case	Low-Torque Case
Error ( $I_{\text{sensed}}$ ) due to unequal rise and fall times per interrogation period		
$I_t = 30 \text{ mA}$	$4.7 \times 10^{-10} \text{ amp.-sec. or}$ $9.6 \times 10^{-4} \text{ arc-sec for}$ Kearfott Model 2544 gyro	
$I_t = 1 \text{ mA}$	$1 \times 10^{-11} \text{ amp.-sec. or}$ $2.05 \times 10^{-5} \text{ arc-sec for}$ Kearfott Model 2544 gyro	
$I_t = 200 \text{ mA}$	$8.3 \times 10^{-9} \text{ amp.-sec. or}$ 0.017 arc-sec for Kearfott Model 2544 gyro	
Total RMS noise at input of IC1 op. amp. in the frequency band 0.1 Hz to 200 kHz		$20.9 \mu\text{V}_{\text{RMS}}$
Rise time (10-90%) of current through torquer (*)		70 ns
Fall time (10-90%) of current through torquer (*)		90 ns

TABLE 12.1 (continued)

Item	High-Torque Case	Low-Torque Case
Rise and fall times when switching scale factors (30 mA - 60 mA) (*)		5-10 $\mu$ s
Settling time when switching scale factors (30 mA - 60 mA) (*)		12 $\mu$ s
Rise time of H-switch driver output (*)		22 ns
Fall time of H-switch driver output (*)		15 ns
Rise time of TTL to CMOS interface output (*)		60 ns
Fall time of TTL to CMOS interface output (*)		16 ns
(*) indicates experimentally observed quantities.		

Circuit layout is a very important parameter in circuit performance. A useful study would be to seek an optimum layout of the TCG for optimum performance.

Optical isolators are faster now than when this work was begun. The possibility of using these devices in the H-switch should be investigated.

The TCG was not purposely designed with low noise performance as a principal goal. Although components were chosen with noise considered, noise was somewhat relegated to a status of lesser importance than steady-state accuracy, etc. A study on components, biasing, etc., to optimize the noise characteristics of the TCG without sacrificing circuit performance would be a healthy undertaking. Flicker noise compensation in the MOSFET's needs investigating.<sup>60</sup>

A study on new MOSFET's available for use in the TCG would be helpful. The technology is growing so rapidly as to obsolete some older devices. Perhaps SOS MOSFET's should be experimentally evaluated in the circuit to ascertain advantages and disadvantages of such devices.

## BIBLIOGRAPHY

## BIBLIOGRAPHY

1. A. W. Lawrence, et. al., The Design of an Advanced Strapdown Gyroscope, NASA Contract No. NAS 12-687, Hamilton Standard System Center, February 15, 1970.
2. John R. Howatt, A Gyroscope Bilevel-Compensated Torque Rebalance, NASA Contract No. NAS 9-6863, Draper Laboratory, Massachusetts Institute of Technology, 1970.
3. Scientific Report S-23, A Study of Strapdown Platform Technology, NASA Contract No. NAS 8-27296/DCN 1-1-40-10230, Dept. of Electrical Engineering, The University of Tennessee, Knoxville, Tenn., April 15, 1972.
4. R. D. McKnight, A Comparison of Two Current Regulator Loops for a Strapdown Gyroscope, M. S. Thesis, Dept. of Electrical Engineering, The University of Tennessee, Knoxville, Tenn., Dec., 1972.
5. T. V. Blalock, E. J. Kennedy, and R. D. McKnight, Scientific Report S-25, Development of a Width-Modulated Pulse Rebalance Electronics Loop for Strapdown Gyroscopes, NASA Contract No. NAS 8-27296/DCN 1-1-40-10230, Dept. of Electrical Engineering, The University of Tennessee, Knoxville, Tenn., July 13, 1973.
6. DC Power Supply Handbook, Hewlett Packard Application Note 90A, Hewlett Packard Co., Palo Alto, Calif., 1970.
7. Paul Birman, Power Supply Handbook, Kepco, Inc., Flushing, N.Y., 1965.
8. Semiconductor Power Circuits Handbook, Motorola, Inc., Phoenix, Ariz., 1968.
9. Erwin Kreyszig, Advanced Engineering Mathematics, John Wiley and Sons, Inc., New York, 1968.
10. Leonard Strauss, Wave Generation and Shaping, McGraw-Hill Book Co., New York, 1970.
11. Paul Richman, Characteristics and Operation of MOS Field-Effect Devices, McGraw-Hill Book Co., New York, 1967.
12. C. K. Walters and R. N. Racino, Design Considerations and Performance of Motorola Temperature-Compensated Zener (Reference) Diodes, Motorola Application Note AN-437A, Motorola Semiconductor Products, Inc., Phoenix, Ariz., 1970.



13. R. C. Dobkin, "IC Creates a Precise 1.2-Volt Reference", Electronic Products Magazine, Vol. 15, No. 4, United Technical Publications, Inc., Garden City, N.Y., Sept. 18, 1972.
14. Zener Diode Handbook, Motorola Semiconductor Products, Inc., Phoenix, Ariz., 1967.
15. Bob Botos, FET Current Regulators-Circuits and Diodes, Motorola Application Note AN-462, Motorola Semiconductor Products, Inc., Phoenix, Ariz., 1971.
16. Bob Botos, Low Frequency Applications of Field-Effect Transistors, Motorola Application Note AN-511, Motorola Semiconductor Products, Inc., Phoenix, Ariz., 1971.
17. William Gosling, Field Effect Transistor Applications, Wiley and Sons, New York, 1965.
18. J. G. Graeme, G. E. Tobey, and L. P. Huelsman, editors, Operational Amplifiers - Design and Applications, McGraw-Hill Book Co., New York, 1971.
19. Arpad Barna, Operational Amplifiers, Wiley-Interscience, New York, 1971.
20. Ed Renschler, The MC1539 Operational Amplifier and Its Applications, Motorola Application Note AN-439, Motorola Semiconductor Products, Inc., Phoenix, Ariz., 1968.
21. "Lift IC Op-Amp Performance at High Frequencies by Adding a 'Fast' Amplifier", Electronic Design, Vol. 21, No. 4, Hayden Publishing Co., Rochelle Park, N.J., Feb. 15, 1973.
22. National Linear Applications Handbook, National Semiconductor Corp., Santa Clara, Calif., 1972.
23. Eugene R. Hnatek, A User's Handbook of Integrated Circuits, John Wiley & Sons, New York, 1973.
24. R. J. Schwarz and B. Friedland, Linear Systems, McGraw-Hill Book Co., New York, 1965.
25. S. Goldman, Laplace Transform Theory and Electrical Transients, Dover Publications, Inc. New York, 1966.
26. D. K. Cheng, Analysis of Linear Systems, Addison-Wesley Publishing Co., Inc., Reading, Mass., 1959.

27. J. J. D'Azzo and C. H. Houppis, Feedback Control System Analysis and Synthesis, McGraw-Hill Book Co., New York, 1966.
28. R. Saucedo and E. E. Schiring, Introduction to Continuous and Digital Control Systems, The Macmillan Co., New York, 1965.
29. J. F. Pierce and T. J. Paulus, Applied Electronics, Charles E. Merrill Publishing Co., Columbus, Ohio, 1972.
30. T. R. Williams, Programming Notes: PCAPS, Princeton University, Princeton, New Jersey, 1970.
31. J. Millman and C. C. Halkias, Integrated Electronics: Analog and Digital Circuits and Systems, McGraw-Hill Book Co., New York, 1972.
32. R. G. Brown and J. W. Nilsson, Introduction to Linear Systems Analysis, John Wiley and Sons, Inc., New York, 1962.
33. J. J. DiStefano, III, A. R. Stubberud, and I. J. Williams, Theory and Problems of Feedback and Control Systems, Schaum's Outline Series, McGraw-Hill Book Co., New York, 1967.
34. R. F. Shea, Editor-in-Chief, Amplifier Handbook, McGraw-Hill Book Co., New York, 1966.
35. J. G. Graeme, Applications of Operational Amplifiers - Third Generation Techniques, McGraw-Hill Co., New York, 1973.
36. R. D. Thornton, C. L. Searle, D. O. Pederson, R. B. Adler, and E. J. Angelo, Jr., Multistage Transistor Circuits, John Wiley & Sons, Inc., New York, 1965.
37. Dale Buhanan, Investigation of Current-Gain Temperature Dependence in Silicon Transistors, IEEE Transactions on Electron Devices, Vol. ED-16, No. 1, January, 1969.
38. C. L. Searle, A. R. Boothroyd, E. J. Angelo, Jr., P. E. Gray, and D. O. Pederson, Elementary Circuit Properties of Transistors, John Wiley & Sons, Inc., New York, 1964.
39. A. S. Grove, Physics and Technology of Semiconductor Devices, John Wiley & Sons, Inc., New York, 1967.
40. C. T. Sah, Characteristics of the Metal-Oxide-Semiconductor Transistors, IEEE Transactions on Electron Devices, Vol. ED-11, No. 7, July, 1964.

41. L. Smith and D. H. Sheingold, Noise and Operational Amplifier Circuits, Analog Dialogue, Volume 3, No. 1, Analog Devices, Inc., Cambridge, Mass., March, 1969.
42. C. D. Motchenbacher and F. C. Fitchen, Low-Noise Electronics Design, John Wiley & Sons, Inc., New York, 1973.
43. R. D. Thornton, D. DeWitt, P. E. Gray, and E. R. Chenette, Characteristics and Limitations of Transistors, John Wiley & Sons, Inc., New York, 1966.
44. N. Wax, Editor, Selected Papers on Stochastic Processes, Dover Publications, Inc., New York, 1954.
45. J. R. Miller, Editor, (Prepared by the Engineering Staff of Texas Instruments, Inc.), Solid-State Communications, McGraw-Hill Book Co., New York, 1966.
46. R. Brubaker, Semiconductor Noise Figure Considerations, Motorola Application Note AN-421, Motorola Semiconductor Products, Inc., Phoenix, Ariz., 1968.
47. S. Christensson, I. Lundström, and C. Svensson, Low Frequency Noise in MOS Transistors, Solid State Electronics, Vol. 11, pp. 797-812, Pergamon Press, Great Britain, 1968.
48. R. S. Ronen, Low-Frequency 1/f Noise in MOSFET's, RCA Review, Vol. 34, No. 2, RCA Research and Engineering, RCA Corp., Princeton, N.J., June, 1973.
49. J. F. Pierce, Transistor Circuit Theory and Design, Charles E. Merrill Books, Inc., Columbus, Ohio, 1963.
50. M. B. Das and J. M. Moore, Measurements and Interpretation of Low-Frequency Noise in FET's, IEEE Transactions on Electron Devices, Vol. ED-21, No. 4, April, 1974.
51. E. A. Torrero, Associate editor, Focus on CMOS, Electronic Design, Vol. 20, No. 8, April 13, 1972.
52. W. F. Kalin, CMOS Logic Elements Interface Easily, Electronic Design, Vol. 21, No. 5, March 1, 1973.
53. B. Furlow, Why Go CMOS? The answer today is a lot different than it was a year ago, EDN, Nov. 1, 1972.
54. B. Furlow, The basic building blocks in the 4000 Series have made CMOS a full fledged logic family, EDN, Dec. 1, 1972.

55. Bernard Schmidt, Motorola Semiconductor Products, Using CMOS in system designs - those all-important details, EDN, January 5, 1973.
56. B. Furlow, Associate Editor, Interfacing CMOS with other logic and display devices, EDN, February 5, 1973.
57. Bill Furlow, Associate Editor, CMOS gates in linear applications: the results are surprisingly good, EDN, March 5, 1973.
58. Bill Furlow, Associate Editor, Here's a list of manufacturers, their product lines and bibliography, EDN, April 20, 1973.
59. A. Alan, Noise Immunity Comparison of CMOS Versus Popular Bipolar Logic Families, Motorola Semiconductor Products, Inc., Phoenix, Ariz., 1973.
60. S. J. Lee and A. Van Der Ziel, Flicker noise compensation in high-impedance MOSFET circuits, Solid State Electronics, Vol. 16, pp. 1301-1302, Pergamon Press, Great Britain, 1973.

## APPENDIXES

## APPENDIX A

### DEVELOPMENT OF EQUATION (2.3) FOR ERROR

#### ANALYSIS OF SCALE FACTOR AND BIAS

#### CURRENT ERRORS IN LOWER

#### H-SWITCH ELEMENTS

The following equations apply to the circuit illustrated in Figure 2.5.

$$-\frac{e_1}{R_p} + \frac{e_2 - e_1}{R_T} + I_A(\omega) + I_B(\omega) = 0 \quad . \quad (A.1)$$

$$I = e_2 \left( \frac{1}{R_T} + \frac{1}{R_o} \right) - \frac{e_1}{R_T} = A_2 e_o \quad ,$$

$$= A_1 A_2 [V_{Ref}(\omega) - e_1] \quad . \quad (A.2)$$

$$I_{T1} = \frac{e_2 - e_1}{R_T} \quad . \quad (A.3)$$

Equations (A.1) and (A.2) can be rewritten as

$$\left( \frac{R_p + R_T}{R_p R_T} \right) e_1 - \left( \frac{1}{R_T} \right) e_2 = I_A(\omega) + I_B(\omega) \quad , \quad (A.4)$$

and

$$\left( \frac{1}{R_T} - A_1 A_2 \right) e_1 - \left( \frac{R_O + R_T}{R_O R_T} \right) e_2 = - A_1 A_2 V_{Ref}(\omega) , \quad (A.5)$$

respectively. The result of using Cramer's rule to solve for  $e_1$  and  $e_2$  and then substituting these values into Equation (A.3) is

$$I_{T1} = R_O A_1(j\omega) A_2(j\omega) V_{Ref}(\omega) / x_1$$

$$\frac{-[I_A(\omega) + I_B(\omega)] [R_p + R_O R_p A_1(j\omega) A_2(j\omega)]}{x_1} , \quad (A.6)$$

where

$$x_1 = R_O + R_p + R_T + R_O R_p A_1(j\omega) A_2(j\omega) . \quad (A.7)$$

## APPENDIX B

### TORQUER COMPENSATION FOR THE KEARFOTT

#### MODEL 2544 GYRO

The torquer coil of the gyro must be compensated if undesirable transients due to switching current levels and polarity are to be minimized. Optimum compensation for switching current polarity is not optimum compensation for switching current levels. With the modified Hamilton Standard logic used with the U. T. system,<sup>5</sup> switching current levels occurs far less frequently than switching current polarity at the 2.4 kHz limit cycle rate. Hence, less error should be incurred by compensating the torquer coil for the 2.4 kHz rate of switching current polarity.

Figure B.1, shown below, will be used to aid in calculating the required values of  $R_{tc}$  and  $C_{tc}$ . Experimental values of  $R_t = 71.7 \Omega$ ,  $L_T = 3.08 \text{ mH}$ , and  $C_s = C_{\text{Stray}} = 20.4 \text{ pF}$  are given in Chapter III. In the calculation to follow,

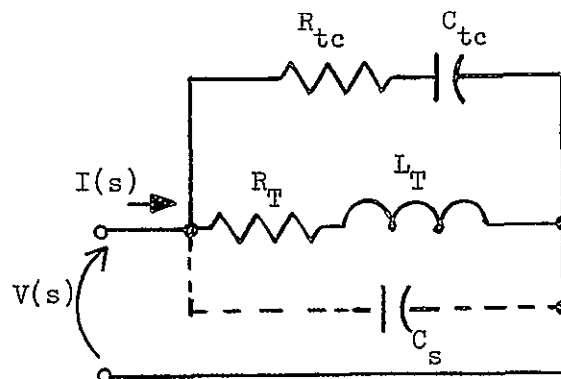


FIGURE B.1

EQUIVALENT CIRCUIT OF THE TORQUER  
COIL AND COMPENSATION



the stray capacitance is neglected.

From Figure B.1,

$$Z(s) = \frac{V(s)}{I(s)} = \frac{(sR_{tc}C_{tc} + 1)(sL_T + 1)}{s^2L_TC_{tc} + s(R_{tc}C_{tc} + R_TC_{tc}) + 1} . \quad (B.1)$$

Let  $R_{tc} = R_T$ . Equation (B.1) becomes

$$Z(s) = \frac{s^2L_TR_TC_{tc} + s(R_T^2C_{tc} + L_T) + R_T}{s^2L_TC_{tc} + s(2R_TC_{tc}) + 1} . \quad (B.2)$$

If  $s = j\omega$ , then

$$Z(j\omega) = \frac{(R_T - \omega^2L_TR_TC_{tc}) + j\omega(R_T^2C_{tc} + L_T)}{(1 - \omega^2L_TC_{tc}) + j\omega(2R_TC_{tc})} = \frac{a + jb}{c + jd} . \quad (B.3)$$

$Z(j\omega)$  will be resistive if  $ad = bc$ , or

$$(R_T - \omega^2L_TR_TC_{tc})(2\omega R_TC_{tc}) = \omega(R_T^2C_{tc} + L_T)(1 - \omega^2L_TC_{tc}) . \quad (B.4)$$

Equation (B.4) can be written

$$C_{tc}^2 - \left( \frac{R_T^2 + \omega^2L_T^2}{\omega^2L_TR_T^2} \right) C_{tc} + \frac{L_T}{\omega^2L_TR_T^2} = 0 . \quad (B.5)$$

Substitution of  $R_T = 71.7 \, \Omega$ ,  $L_T = 3.08 \, \text{mH}$ , and  $\omega = 2\pi f = 2\pi(2.4 \, \text{kHz}) = 15079.64 \, \text{rad/sec}$  into Equation (B.5) gives

$$C_{tc}^2 - (2.03 \times 10^{-6}) C_{tc} + (8.602 \times 10^{-13}) = 0 . \quad (B.6)$$

Equation (B.6) is in the form

$$ax^2 + bx + c = 0 , \quad (B.7)$$

which is the quadratic equation. Applying the quadratic formula to Equation (B.6) yields two values of  $C_{tc}$ :  $C_{tc1} = 0.6025 \mu F$ ; and  $C_{tc2} = 1.428 \mu F$ . The lesser value of capacitance can then be chosen as the compensation capacitance.  $R_{tc}$  was set equal to  $R_T$  earlier. Hence, the compensation values are

$$R_{tc} \approx 71.7 \, \Omega, \, C_{tc} \approx 0.60 \, \mu F . \quad (B.8)$$

A calculation similar to the one above was performed with the stray capacitance included. To four significant figures the result was the same as for the case neglecting  $C_s$ .

## APPENDIX C

### OPEN-LOOP FREQUENCY RESPONSE OF AN OP. AMP. FROM CLOSED-LOOP INVERTING MODE DATA

Consider an operational amplifier with an open-loop voltage gain  $A$ , as yet unknown. The device may be operated in a closed-loop inverting mode as illustrated in Figure C.1.

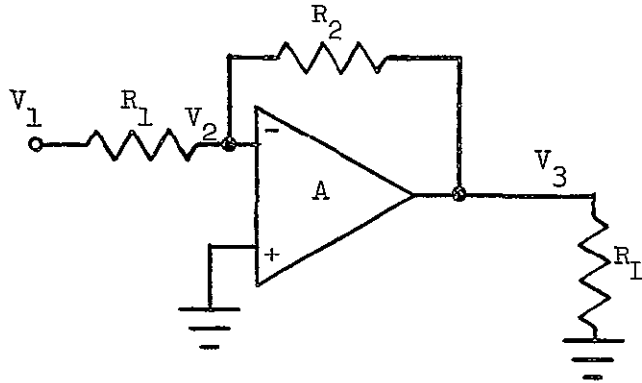


FIGURE C.1

#### CLOSED-LOOP INVERTING-MODE CONFIGURATION OF AN OPERATIONAL AMPLIFIER

The following equations may be written with reference to Figure C.1:

$$\frac{V_1 - V_2}{R_1} + \frac{V_3 - V_2}{R_2} = 0 ; \quad (C.1)$$

and

$$V_3 = -AV_2 \quad . \quad (C.2)$$

Equation (C.1) can be solved in terms of  $V_1$  and  $V_3$  to give

$$V_2 = \frac{R_2}{R_1 + R_2} V_1 + \frac{R_1}{R_1 + R_2} V_3 \quad . \quad (C.3)$$

A brief study of Equation (C.3) and Figure C.1 indicates that Figure C.1 can be represented as illustrated in Figure C.2.

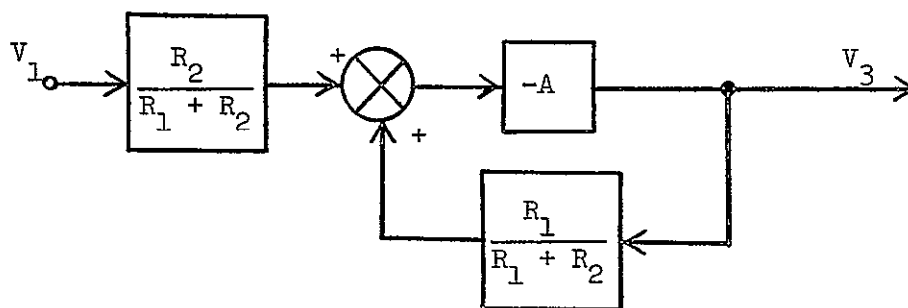


FIGURE C.2

A FEEDBACK CONFIGURATION HAVING THE SAME  
PARAMETER RELATIONSHIPS AS FIGURE C.1

The diagram illustrated in Figure C.2 can be transformed<sup>33</sup> to that illustrated in Figure C.3.

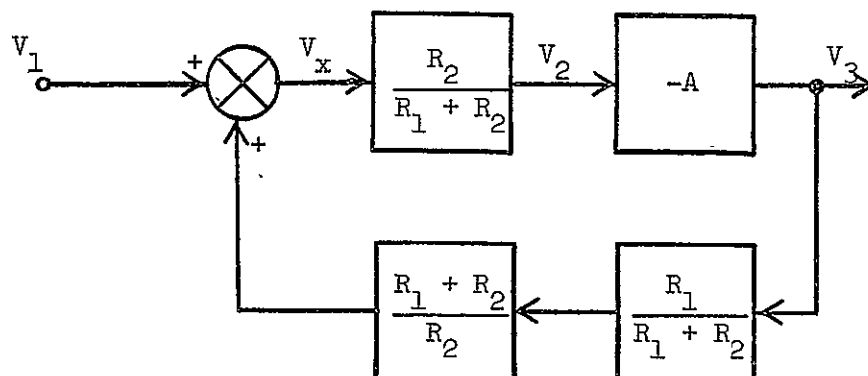


FIGURE C.3

A BLOCK DIAGRAM REPRESENTATION EQUIVALENT  
TO THAT IN FIGURE C.2

Figure C.3 can be simplified to the block diagram representation of a feedback system as illustrated in Figure C.4.

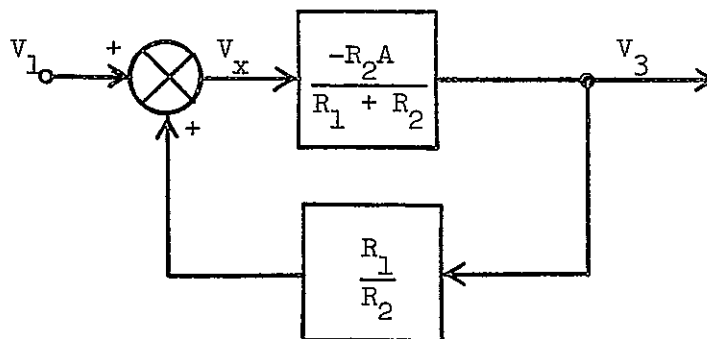


FIGURE C.4

A BLOCK DIAGRAM REPRESENTATION EQUIVALENT  
TO THAT IN FIGURE C.3

Using Figure C.4, the following set of equations may be written:

$$V_3 = \left( \frac{-R_2}{R_1 + R_2} \right) A V_x ; \quad (C.4)$$

$$V_x = V_1 + V_f ; \quad (C.5)$$

$$V_f = \frac{R_1}{R_2} V_3 . \quad (C.6)$$

Solving Equations (C.4), (C.5), and (C.6) for  $V_3$  in terms of  $V_1$ , and simplifying, yields

$$A_V^{CL} \equiv \frac{V_3}{V_1} = \frac{-AR_2}{R_2 + (A + 1)R_1} . \quad (C.7)$$

$A_V^{CL}$  is the closed-loop voltage gain of the op. amp. \_\_\_\_\_

The Nichols chart is set up to accommodate data from a unity feedback system. Note in Figure C.4 that if  $R_1 = R_2$ , a unity feedback system results. Therefore, for ease in graphical analysis, choose

$$R_1 = R_2 ; \quad (C.8)$$

Equation (C.7) becomes

$$A_V^{CL} = \frac{-\frac{A}{2}}{1 + \frac{A}{2}} . \quad (C.9)$$

Define

$$A_1 = \frac{A}{2} . \quad (C.10)$$

Then,

$$A_V^{CL} = \frac{-A_1}{1 + A_1} , \quad (C.11)$$

and

$$\left| A_V^{CL} \right| = \left| \frac{-A_1}{1 + A_1} \right| . \quad (C.12)$$

Equation (C.12) is in the form

$$\left| A_V^{CL} \right| = \left| \frac{T}{1 + T} \right| ,$$

where the feedback factor, B, is unity. Experimental data for  $A_V^{CL}$  can be obtained using the configuration in Figure C.1. This data can be plotted on the curvilinear coordinates of the Nichols chart using frequency as a parameter.  $A_1$  can then be taken from the linear coordinates of the Nichols chart and plotted as a Bode plot. A is obtainable from  $A_1$ .

From Equation (C.10),

$$A = 2A_1 . \quad (C.13)$$

Obviously,  $A$  has the same phase plot as  $A_1$ . The magnitude plot in dB for  $A$  is related to that of  $A_1$  by

$$|A|_{\text{dB}} = |A_1|_{\text{dB}} + 6 \text{ dB} . \quad (\text{C.14})$$



## APPENDIX D

### OUTLINE, PLOTS, AND DATA FOR A GRAPHICAL SOLUTION OF THE CLOSED-LOOP FREQUENCY RESPONSE FROM T VIA A NICHOLS CHART

A graphical solution of the closed-loop frequency response of the torque current generator using a Nichols chart involves the following steps:

- (1) Construct a Bode plot of  $|T|$  and  $\angle T$ . This was done in Chapter IV.
- (2) Using the data from step (1), construct the plot of  $|T|$  versus  $\angle T$  on the linear coordinates of the Nichols chart with frequency as a parameter. Figure D.1 in this appendix contains these plots.
- (3) The values of  $\left| \frac{T}{(1+T)} \right|$  and  $\angle \frac{T}{(1+T)}$  may be read from the curved coordinates of the Nichols chart. Data of this type is contained in Table D.1 of this appendix.
- (4) Using the data from step (3), construct the Bode plot of  $\left| \frac{T}{(1+T)} \right|$  and  $\angle \frac{T}{1+T}$ .
- (5) Combine the Bode plots of  $\left| \frac{T}{(1+T)} \right|$  and  $\left( \frac{1}{B} \right)$  to form a plot of  $A_f$ .

The plots of step (4) are not shown. However, the plot of step (5) is given as Figure 5.4.

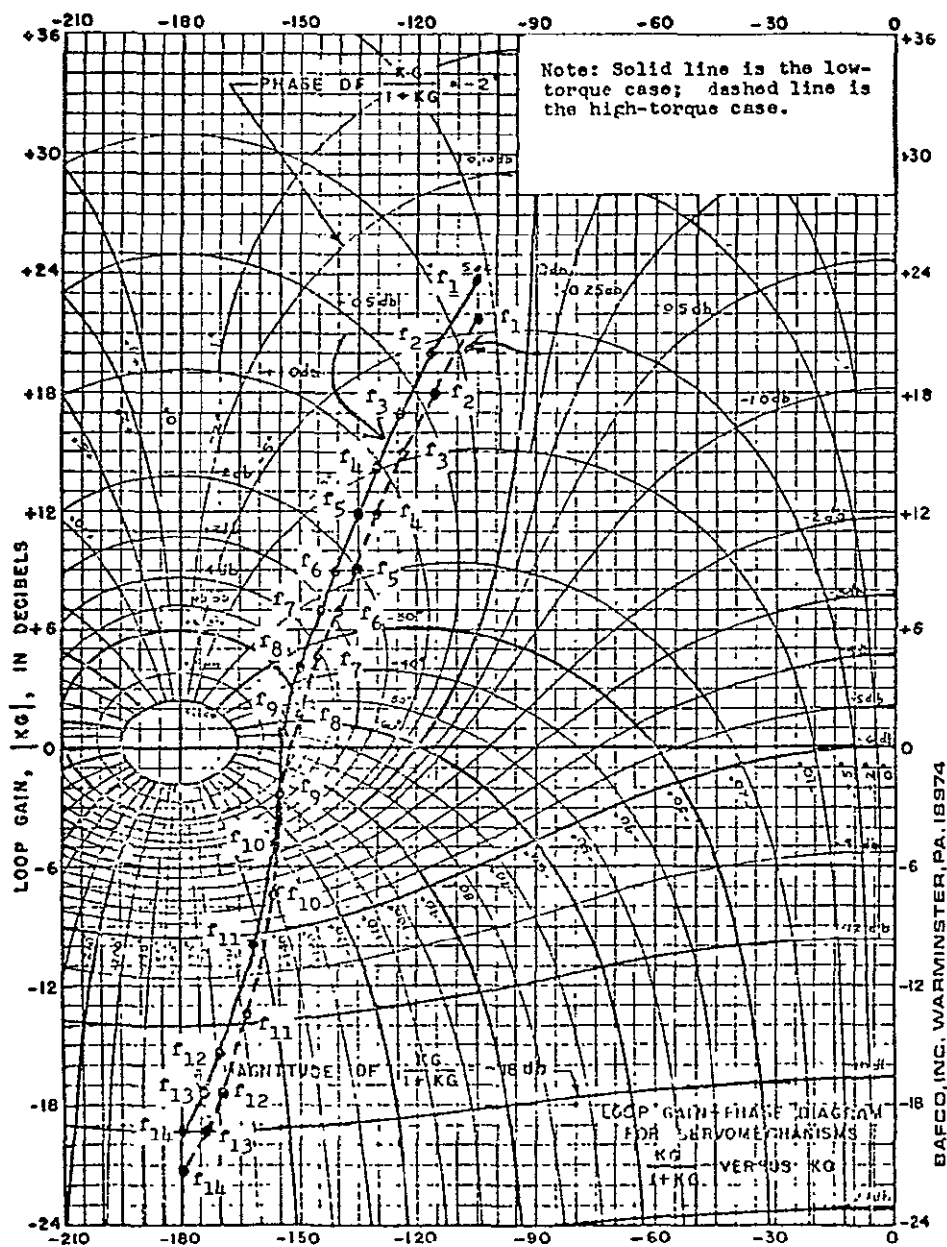


FIGURE D.1

THE LOOP TRANSMISSION OF THE TCG  
PLOTTED ON A NICHOLS CHART

ORIGINAL PAGE IS  
OF POOR QUALITY

TABLE D.1

DATA FOR GRAPHICAL SOLUTION OF CLOSED-LOOP FREQUENCY  
RESPONSE FROM T VIA NICHOLS CHART

Freq. Parameter	f	$ T $ (dB) (L.T.)	$\angle T$ (°) (L.T.)	$ T $ (dB) (H.T.)	$\angle T$ (°) (H.T.)	$\left \frac{T}{1+T}\right $ (dB) (L.T.)	$\angle \frac{T}{1+T}$ (°) (L.T.)	$\left \frac{T}{1+T}\right $ (dB) (H.T.)	$\angle \frac{T}{1+T}$ (°) (H.T.)
$f_1$	20 kHz	24 dB	105	21.9 dB	105	0.11	-3.7	0.15	-4.6
$f_2$	30 k	20	116	17.9	116	0.35	-5.5	0.42	-7.3
$f_3$	40 k	17	124	14.9	124	0.70	-7.5	0.80	-9.5
$f_4$	50 k	14	130	11.9	130	1.1	-10	1.3	-13
$f_5$	60 k	11	135	8.9	135	1.7	-15	2.0	-19
$f_6$	70 k	9	141	6.9	141	2.3	-18	2.8	-25
$f_7$	80 k	7	144	4.9	144	3.2	-23	3.9	-33
$f_8$	100 k	4	150	1.9	150	5.1	-35	6.2	-57
$f_9$	130 k	0	154	-2.1	154	7.0	-77	4.7	-104
$f_{10}$	200 k	-5	157	-7.1	157	0.5	-132	-3.0	-140
$f_{11}$	300 k	-11	163	-13.1	163	-8.2	-157	-11	-158

TABLE D.1 (continued)

Freq. Parameter	$f$	$ T $ (dB) (L.T.)	$\angle T$ (°) (L.T.)	$ T $ (dB) (H.T.)	$\angle T$ (°) (H.T.)	$\left \frac{T}{1+T}\right $ (dB) (L.T.)	$\angle \frac{T}{1+T}$ (°) (L.T.)	$\left \frac{T}{1+T}\right $ (dB) (H.T.)	$\angle \frac{T}{1+T}$ (°) (H.T.)
$f_{12}$	400 k	-15	170	-17.1	170	-13.5	-168	-15.5	-168
$f_{13}$	500 k	-17	174	-19.1	174	-15.5	-173	-17.5	-173
$f_{14}$	600 k	-19	180	-21.1	180	-17.5	-180	-20	-180

## APPENDIX E

### DERIVATION OF THE LOOP TRANSMISSION OF THE TORQUE CURRENT GENERATOR

The loop transmission of the TCG loop has the general form

$$T = A_V^{OL} B , \quad (E.1)$$

where  $A_V^{OL}$  is the open-loop voltage gain and  $B$  is the feedback factor.  $B$  was shown in Chapter IV to be frequency independent over the frequency range of interest. The frequency dependence of  $T$  then lies in  $A_V^{OL}$ .  $A_V^{OL}$  can be expressed as the product of a midband value of  $A_V^{OL}$ ,  $A_V^{OL}(\text{mid})$ , and some frequency dependent factors representing the poles and zeros of the TCG loop.

With the aid of Figure 3.1, the following expression for  $A_V^{OL}(\text{mid})$  may be written:

$$A_V^{OL}(\text{mid}) = A_{V1}(\text{mid}) A_1 A_{d1} A_2 . \quad (E.2)$$

In Equation (E.2),  $A_{V1}(\text{mid})$  is the midband voltage gain of the AD504M op. amp.;  $A_1$  is the voltage division factor from the output of the op. amp. to the input of Q1A;  $A_{d1}$  is the midband differential voltage gain from the base of Q1A to the collector of Q1B; and,  $A_2$  is the midband voltage gain of the Darlington pair consisting of Q2B and Q3.

From the manufacturer's data book,

$$A_{V1}(\text{mid}) \approx -8 \times 10^6 . \quad (\text{E.3})$$

The negative sign in  $A_{V1}(\text{mid})$  is used to indicate that the correction signal is fed to the inverting input of the op. amp.  $T$  must be negative for negative feedback. From Figure 3.1,

$$R_{i1A} \approx (\beta_{1A} + 1) [r_{e1A} + R7 + R8 + r_{e1B} + \frac{R9}{\beta_{1B} + 1}] . \quad (\text{E.4})$$

Then,

$$A_1 = \frac{R_{i1A}}{R_{i1A} + R_4} . \quad (\text{E.5})$$

Substitution of the proper values from the circuit and bias calculations into Equations (E.4) and (E.5) yields

$$A_1 \approx 0.997 : \quad (\text{E.6})$$

Equation (E.6) holds for both the low- and high-torque cases.

$$A_{d1} \approx \frac{R6}{r_{e1A} + R7 + R8 + r_{e1B} + \frac{R9}{\beta_{1B} + 1}} . \quad (\text{E.7})$$

Substitution of the proper values into Equation (E.7) gives

$$A_{dl} \text{ (L.T.)} \approx 17.5 , \quad (\text{E.8})$$

and

$$A_{dl} \text{ (H.T.)} \approx 17.7 \quad (\text{E.9})$$

for the low- and high-torque cases, respectively.

$$A_2 = \frac{(\beta_3 + 1) R_B}{r_{e2B} + (\beta_3 + 1) (r_{e3} + R_B)} \approx 1 \quad (\text{E.10})$$

for both the low- and high-torque cases.  $R_B$  is the resistance seen looking out from the emitter of Q3.

From Figure 5.5, the following values of B may be calculated:

$$\left. \begin{array}{l} B \text{ (L.T.)} \approx 0.684 , \\ B \text{ (H.T.)} \approx 0.520 . \end{array} \right\} \quad (\text{E.11})$$

Equations (E.2) through (E.11) provide information which, when substituted into Equation (E.1), yields

$$\left. \begin{array}{l} |T_{mid}| \text{ (L.T.)} \approx 9.55 \times 10^7 , \\ |T_{mid}| \text{ (H.T.)} \approx 7.34 \times 10^7 . \end{array} \right\} \quad (\text{E.12})$$

The values of  $|T_{\text{mid}}|$  given in Equation (E.12) are midband values of the loop gain for the TCG.

However,  $T$  is a function of frequency. The poles and zeros of  $T$  must be determined to completely describe  $T$ .

The TCG is completely DC coupled. Since no zeros occur in the response of the AD504M op. amp. in the region of interest, the only zero in the expression for  $T$  will be that due to the RC lag network. The experimentally-obtained open-loop frequency response curve for the AD504M op. amp. is given in Figure 4.2. A brief study of this curve indicates that the curve can be closely approximated over the frequency range of DC to 1 MHz by the expression

$$\begin{aligned}
 A_{V1} &= \frac{A_{V1}(\text{mid})}{(1 + s\tau_1)(1 + s\tau_2)} = \frac{-8 \times 10^6}{[1 + s(39.8 \text{ sec})][1 + s(0.398 \text{ } \mu\text{sec})]} , \\
 &= \frac{-8 \times 10^6}{[1 + j\left(\frac{f}{0.004 \text{ Hz}}\right)][1 + j\left(\frac{f}{400 \text{ kHz}}\right)]} . \quad (E.13)
 \end{aligned}$$

The impedance seen looking into the top of the H-switch was shown in Chapter V to appear purely resistive to approximately 10 MHz. The remaining frequency dependence of the TCG is associated with  $Q1$ ,  $Q2$ , and  $Q3$ , their bias networks, and the RC lag network. In fact, the relevant zero and poles are contained in the interaction of the output of  $Q1B$ , the input of  $Q2B$ , and the RC lag network. The pertinent formulas for calculating the zero and pole locations for such a case are given in Reference 29. For the case at hand, these are:



$$f_{p1} \approx \frac{1}{2\pi R_{Leq1B} (C_{Leq1B} + C_c)} ; \quad (E.14)$$

$$f_{p2} \approx \frac{1}{2\pi R_c \left[ \frac{C_{Leq1B} C_c}{C_{Leq1B} + C_c} \right]} ; \quad (E.15)$$

and

$$f_z \approx \frac{1}{2\pi R_c C_c} . \quad (E.16)$$

$R_{Leq1B}$  and  $C_{Leq1B}$  represent the equivalent impedance from the collector of Q1B to ground with the  $R_c C_c$  lag network disconnected.

$R_{Leq1B}$  can easily be approximated as 6.2 k  $\Omega$ .  $C_{Leq1B}$  is a bit more complicated. Reference 29 again has the appropriate formulas for making the approximation. The output capacitance of Q1B may be approximated as

$$C_{out(1B)} \approx C_{ob(1B)} \left( 1 + \frac{R_b}{R_e} \right) . \quad (E.17)$$

where  $R_b$  is the equivalent base resistance, and  $R_e$  is the total AC resistance in the emitter circuit. Substitution of proper parameter values into Equation (E.17) yields

$$C_{out(1B)} \approx 31.4 \text{ pF} . \quad (E.18)$$

The input capacitance of Q2B can be conservatively approximated as

$$C_{in(2B)} \approx 10 \text{ pF} . \quad (\text{E.19})$$

Then,

$$C_{Leq1B} = C_{out(1B)} + C_{in(2B)} \approx 41.4 \text{ pF} . \quad (\text{E.20})$$

Values for  $R_c$  and  $C_c$ , as given in Figure 3.1, are  $1.5 \text{ k } \Omega$  and  $360 \text{ pF}$ , respectively. Substitution of the proper R and C values into Equations (E.14), (E.15), and (E.16) gives

$$f_{p1} \approx 64.0 \text{ kHz} ; \quad (\text{E.21})$$

$$f_{p2} \approx 2.86 \text{ MHz} ; \quad (\text{E.22})$$

and

$$f_z \approx 295 \text{ kHz} . \quad (\text{E.23})$$

These are approximately the same for both torquing levels.

The indicated product  $A_1 A_{d1} A_2$  in Equation E.2 represents the voltage gain from the output of the op. amp. to the output of the current regulator (emitter of Q3). Using the appropriate parameters from the above discussion, this gain can be represented as

$$\begin{aligned}
 A_{V2} &\equiv A_1 A_{d1} A_2 , \\
 &= \frac{A_{V2}^{(mid)} (1 + j \frac{f}{f_z})}{(1 + j \frac{f}{f_{p1}}) (1 + j \frac{f}{f_{p2}})} .
 \end{aligned}
 \tag{E.24}$$

Combining the necessary equations from this appendix, an expression for  $T$  as a function of frequency may be written. For the low-torque case,

$$T(L.T.) \approx \frac{(-9.55 \times 10^7) (1 + j \frac{f}{295 \text{ kHz}})}{\left[1 + j \frac{f}{0.004 \text{ Hz}}\right] \left[1 + j \frac{f}{64 \text{ kHz}}\right] \left[1 + j \frac{f}{400 \text{ kHz}}\right] \left[1 + j \frac{f}{2.86 \text{ MHz}}\right]}
 \tag{E.25}$$

Similarly, the high-torque case  $T$  may be written

$$T(H.T.) \approx \frac{(-7.34 \times 10^7) (1 + j \frac{f}{295 \text{ kHz}})}{\left[1 + j \frac{f}{0.004 \text{ Hz}}\right] \left[1 + j \frac{f}{64 \text{ kHz}}\right] \left[1 + j \frac{f}{400 \text{ kHz}}\right] \left[1 + j \frac{f}{2.86 \text{ MHz}}\right]}
 \tag{E.26}$$

The magnitude of  $T$  will be at least -10 dB by the time the zero at 295 kHz is reached, and even more negative for the two higher poles. Within a reasonable error,  $T$  can be approximated as

$$T \approx \frac{T_{mid}}{\left[1 + j \frac{f}{0.004 \text{ Hz}}\right] \left[1 + j \frac{f}{64 \text{ kHz}}\right]} .
 \tag{E.27}$$

$$T(L.T.) \approx \frac{(-9.55 \times 10^7)}{\left[1 + j \frac{f}{0.004 \text{ Hz}}\right] \left[1 + j \frac{f}{64 \text{ kHz}}\right]} .
 \tag{E.28}$$

$$T(H.T.) \approx \frac{(-7.34 \times 10^7)}{\left[1 + j \frac{f}{0.004 \text{ Hz}}\right] \left[1 + j \frac{f}{64 \text{ kHz}}\right]}
 \tag{E.29}$$

## VITA

The author was born in [REDACTED], on [REDACTED]. He attended elementary school in that county. He attended Bellevue Junior High and Messick High School in Memphis, Tennessee, and graduated from high school in May, 1955. He began work at Memphis State University in 1955 and was awarded the Bachelor of Science degree in History in January, 1960.

From March, 1960 to February, 1962, he attended the New Orleans Baptist Theological Seminary in New Orleans, Louisiana. He began teaching in the public schools of Memphis, Tennessee in September, 1962. He taught school there for six years, until August, 1968.

In September, 1968, he entered the University of Tennessee at Knoxville. He received the Bachelor of Science degree in Electrical Engineering in June, 1970, and the Master of Science in Electrical Engineering in December, 1972. He worked as a graduate assistant in the Electrical Engineering Department at the University of Tennessee from January, 1970 until May, 1973. From April, 1972 until April, 1973, he also worked on a research assistantship from the National Aeronautical and Space Administration's Marshall Space Flight Center. He has been a senior development engineer at ORTEC, Inc., Oak Ridge, Tennessee, since August, 1973.

He is married to the former Sara F. Outland of Memphis, Tennessee. They have three daughters, Sarita, Anita, and Lisa.

He is a member of Eta Kappa Nu, Tau Beta Pi, and IEEE.